

SEARCH FOR A HIGH MASS HIGGS
BOSON IN THE CHANNEL
 $H \rightarrow ZZ \rightarrow llbb$ AND DIGITAL
FILTERING FOR THE ATLAS
LEVEL-1 CALORIMETER TRIGGER

David Richard Hadley

*Thesis submitted for the degree of
Doctor of Philosophy*



Particle Physics Group,
School of Physics and Astronomy,
The University of Birmingham.

November 2011.

Abstract

The Standard Model of particle physics predicts the existence of a new massive state: the Higgs Boson. The discovery or exclusion of this particle is one of the main goals of the ATLAS experiment.

One of the greatest experimental challenges at the LHC is to achieve efficient triggering. The ATLAS first level calorimeter trigger uses reduced granularity information from the calorimeters to search for high E_T e , γ , τ and jets as well as identifying high E_T^{miss} and total E_T events. A Finite Impulse Response (FIR) filter combined with a peak finder is applied to identify signals, determine their correct bunch-crossing and improve the energy measurement. A study to determine the optimum filter coefficients is presented. The performance of these filters is investigated with commissioning data and cross-checks of the calibration with initial beam data are shown.

In this thesis a study of the search sensitivity in the channel $H \rightarrow ZZ \rightarrow llbb$ is presented. This channel can contribute to the Higgs search in the high mass region that has been unexplored by previous lower energy colliders. The dominant backgrounds, without b -tagging applied, are extracted from 34.6 pb^{-1} of early LHC data. The event yields are found to be consistent with the Standard Model expectation.

Dedicated to Mom and Dad.

Author's Contribution

The work presented in this thesis is my own (with the exceptions listed below). However, by its very nature particle physics involves close collaboration with colleagues. In particular I have collaborated closely with members of the Birmingham Particle Physics group and the ATLAS Level-1 Calorimeter Trigger group.

- All results presented rely on the ATLAS software as well as external software packages including ROOT [1] and the Monte Carlo event generators listed in Appendix A.
- Chapter 3 provides a review of Higgs physics and contains no original research.
- Chapter 4 describes the LHC and the ATLAS detector. Many of the images are taken from other published ATLAS documents. See the references provided within that chapter.
- The Monte Carlo samples used in chapters 5 and 6 were centrally generated by the ATLAS.
- The model used in the kinematic fit shown in chapter 5 was constructed

by myself using the tools provided by RooFit [2].

- The CLs limits shown in chapter 5 were calculated with MCLIMIT [3] [4].
- The data corrections applied in the analysis shown in chapter 6 were all official corrections provided by various ATLAS working groups.
- Chapter 7 describes the ATLAS Level-1 Calorimeter Trigger. Many of the images are taken from other ATLAS publications. See the references provided within that chapter.

Acknowledgements

I thank my colleagues both in the Birmingham ATLAS group and in the L1Calo collaboration. Special thanks to Alan Watson and Paul Thompson for their advice and guidance. I thank the STFC for their financial support. Finally, thanks to my loved ones for supporting me, despite my negligence while writing this document.

Contents

1	Non-technical Summary	15
2	Introduction	20
3	The Higgs Mechanism and Constraints on the Higgs Boson	
	Mass	23
3.1	Higgs Mechanism	24
3.2	Higgs Boson Decay Properties and Production at the LHC . .	27
3.3	Constraints on m_H	32
4	The LHC and the ATLAS Detector	38
4.1	The Large Hadron Collider	38
4.2	ATLAS	40
4.2.1	Nomenclature	42
4.2.2	Tracking	44
4.2.3	Calorimetry	47
4.2.4	Muon Spectrometer	50
4.2.5	Trigger and Data Acquisition	53

5 Search Prospects for a High Mass Higgs in the Channel

$H \rightarrow ZZ \rightarrow llbb$	56
5.1 Signal Properties and Dominant Backgrounds	57
5.1.1 $H \rightarrow llbb$	57
5.1.2 Z +jets	59
5.1.3 Top-quark Pair Production	60
5.1.4 Di-boson Production	61
5.1.5 QCD	61
5.2 Event Selection	62
5.2.1 Electron Reconstruction	62
5.2.2 Jet Reconstruction and b -tagging	64
5.2.3 Muon Selection	69
5.2.4 Lepton and Jet Invariant mass cut	69
5.2.5 Jet Angular Correlation	72
5.2.6 Missing E_T	75
5.2.7 Trigger	75
5.2.8 Event Reduction	77
5.3 Kinematic Fitting	79
5.3.1 Fitting Procedure	81
5.3.2 Jet Energy Resolution	82
5.3.3 Kinematic Constraints	83
5.3.4 Performance of Kinematic Fit	92
5.4 Background Control Regions	92
5.5 Systematic Effects	97
5.6 Expected Limits	102

5.7	Future Improvements	109
6	Backgrounds to $H \rightarrow ZZ \rightarrow llqq$ in Early LHC Data	110
6.1	Monte Carlo Corrections	110
6.2	Event Preselection	112
6.3	Kinematic Distributions	113
6.4	QCD Background	115
6.5	Z Background	123
6.6	Top-quark Background	123
6.7	Signal Region	126
6.8	Conclusions	130
7	Level-1 Calorimeter Trigger	131
7.1	Preprocessor	131
7.2	Bunch-crossing Identification	133
7.3	Cluster Processor	136
7.4	Jet/Energy Processor	138
8	Digital Filter for the Level-1 Calorimeter Trigger	140
8.1	Digital Filter Implementation	141
8.2	Choice of Filter Coefficients	143
8.3	Measurement of Pulse Shapes	147
8.4	Digital Filter Performance	150
8.5	Saturation Energies in the Preprocessor	156
8.6	LUT E_T Calibration	158
8.7	Summary and Outlook	160

9 Summary	163
9.1 $H \rightarrow ZZ \rightarrow llbb$	163
9.2 L1Calo Preprocessor Digital Filter	164
Bibliography	169
Glossary	170
A Cross-sections	174

List of Figures

3.1	Diagram of the Higgs potential	26
3.2	Feynman diagrams of Higgs production mechanisms at the LHC	28
3.3	Higgs boson production cross-sections at the LHC.	30
3.4	Higgs boson branching fractions.	30
3.5	Higgs boson decay width versus mass	31
3.6	Combined Tevatron Limits on m_H	33
3.7	Leading order Feynman diagrams for WW scattering.	34
3.8	Limits on m_H from the running of λ	35
3.9	χ^2 of global fit for m_H to precision electroweak data.	37
4.1	Diagram of ATLAS	41
4.2	Diagram of the η coverage of the ATLAS sub-detectors.	43
4.3	Diagram of the ATLAS inner detector.	45
4.4	Diagram of the ATLAS calorimetry.	48
4.5	Diagram of the ATLAS muon spectrometer.	51
4.6	Photograph of the barrel toroid during installation.	51
4.7	Overview of the ATLAS Trigger architecture.	53
5.1	Truth-level Kinematic distributions for $H \rightarrow llbb$	58

5.2	Electron ID efficiency	63
5.3	Predicted QCD background for different electron ID cuts . . .	65
5.4	Reconstructed Jet p_T distribution for $lljj$ events	67
5.5	Reconstructed Jet Multiplicity distribution for $lljj$ events . . .	67
5.6	Jet b -tag weight distribution for $lljj$ events	68
5.7	Muon reconstruction efficiency	70
5.8	Predicted QCD background in the muon channel	70
5.9	Reconstructed di-lepton mass distribution for $lljj$ events . . .	71
5.10	Reconstructed di-jet mass distribution for Z +di-jet events . .	73
5.11	$\Delta\phi_{jj}$ distribution for $lljj$ events	74
5.12	Reconstructed Z -boson p_T distribution signal and ZZ events .	74
5.13	E_T^{miss} distribution for $lljj$ events	76
5.14	Signal efficiency for each generated Higgs mass	77
5.15	Reconstructed m_H distribution before kinematic fitting	80
5.16	Components of mass resolution versus m_H before kinematic fitting	80
5.17	Correlation between jet energy uncertainties in $H \rightarrow llbb$ events	82
5.18	Jet Energy uncertainty	84
5.19	Corrections to jet energy scale in the barrel	85
5.20	Corrections to jet energy scale in the end-cap	86
5.21	Jet energy variance versus jet energy	87
5.22	Likelihood component from the di-jet mass constraint	89
5.23	Likelihood component from the jet energy uncertainty	90
5.24	Combined likelihood used in the kinematic fit	91
5.25	Reconstructed m_H distribution after kinematic fitting	93

5.26	Components of mass resolution versus m_H after kinematic fitting	94
5.27	Correction to mass scale	95
5.28	Reconstructed m_{lljj} distributions for signal and background . .	96
5.29	m_{lljj} distribution for events in the Z control region	98
5.30	m_{lljj} distribution for events in the $t\bar{t}$ control region	99
5.31	Expected CL_s with and without systematic uncertainties . . .	105
5.32	Expected CL_s with statistical uncertainties	106
5.33	Expected exclusion confidence limits as a ratio of Standard Model σ	107
5.34	Expected exclusion confidence limits for various integrated lu- minosities without systematic uncertainties.	108
5.35	Expected exclusion confidence limits for various integrated lu- minosities including systematic uncertainties.	108
6.1	Di-lepton invariant mass spectrum	114
6.2	Jet multiplicity in di-lepton events	115
6.3	Di-lepton invariant mass spectrum in $lljj$ events	116
6.4	Kinematic distributions for $lljj$ events	117
6.5	m_{lljj} distribution for Z +jets events	118
6.6	$m_{\mu\mu}$ distribution for same-sign muon pairs	119
6.7	m_{ee} distribution for same-sign electron pairs	119
6.8	m_{ee} and m_{eejj} distributions for QCD enhanced sample	120
6.9	m_{lljj} for events in the Z control region	124
6.10	m_{lljj} for events in the $t\bar{t}$ control region	125
6.11	m_{lljj} for events in the signal region before b -tagging	128

6.12	m_{ujj} for events in the signal region after b -tagging	129
7.1	Level-1 Calorimeter Trigger system architecture.	132
7.2	Trigger towers in L1Calo.	134
7.3	Cluster Processor trigger algorithm	136
7.4	Windows of the Level-1 jet-finding algorithm	138
8.1	BCID in the Preprocessor	142
8.2	Effect of a matched filter on a typical pulse	144
8.3	Typical trigger tower pulse shapes.	148
8.4	Pulse widths in e.m. and hadronic layers.	149
8.5	BCID efficiency turn-on curves for a single trigger tower.	152
8.6	BCID efficiency turn-on curves σ distribution	152
8.7	Noise energy distribution for a single trigger tower.	153
8.8	Noise output probability	154
8.9	Energy residual for a single trigger tower.	155
8.10	Energy resolution for all channels.	156
8.11	Fraction of LUT range used for different scaled filters.	157
8.12	Peak ADC versus LUT output for a single channel in collision events.	159
8.13	LUT gradients measured from collision events.	160

List of Tables

4.1	Performance Goals of the ATLAS detector	40
5.1	Summary of signal and background cross-sections	60
5.2	Summary of Electron ID cuts	63
5.3	Trigger efficiencies for $H \rightarrow llbb$ events	75
5.4	Event reduction by each analysis cut	78
5.5	Systematic effects with the low mass selection	103
5.6	Systematic effects with the high mass selection	103
6.1	Predicted and observed event yields	127
6.2	Predicted signal event yields	127
8.1	Common filter coefficients.	151
A.1	List of signal cross-sections	175
A.2	List of background cross-sections	176

Chapter 1

Non-technical Summary

The following pages attempt to explain the motivation for this research and summarise the results at a level suitable for a non-particle physicist. Expert readers should skip onto chapter 2 on page 20.

There are four known fundamental forces in the universe: gravity and electromagnetism, the forces we are familiar with in our day-to-day lives; the weak force, which is responsible for nuclear decays; and the strong force, which binds together the nucleus and its constituents. The Standard Model of particle physics describes all of these forces, with the notable exception of gravity. It is one of the greatest achievements of modern science and represents our deepest understanding of the fundamental physics of the universe. The model describes how the fundamental matter particles, 6 leptons, 6 quarks and their anti-particles, interact through the exchange of the force-carrying particles: the photon, the mediator of the electromagnetic force; the W^\pm and Z , the mediators of the weak force; and the gluons, the mediators of the strong force.

This theory has been remarkably successful at describing nature. It also has a compelling theoretical motivation: the equations that govern these forces come from underlying symmetries in nature.

There is, however, a problem with this picture: electroweak symmetry, the symmetry that gives rise to the electromagnetic and the weak forces, can only be true if the mediators of those forces are massless. This contradicts the experimentally observed fact that the W^\pm and Z bosons have mass (and very large masses, the Z is almost one hundred times heavier than the proton). Rather than discard the entire Standard Model, a new element is introduced: the Higgs field. This field spontaneously breaks the symmetry in just the right way to produce the observed weak interactions, and produce the masses for the W^\pm and Z particles, leaving the photon massless. The Higgs field also provides a mechanism for all of the other particles of the Standard Model to acquire their masses. The Higgs field has an associated physical state, the Higgs boson, that can be produced and measured in experiment. At the time of writing, it is the only particle of the Standard Model that has not yet been directly observed.

Understanding the mechanism of electroweak symmetry breaking is one of the main unsolved problems of particle physics today. It is a problem that we hope to solve at current and future high energy physics experiments. The Standard Model Higgs boson, if it exists, should be within reach of the Large Hadron Collider (LHC), the worlds highest energy particle accelerator. The LHC is a 27 km accelerator ring located deep underground at the European Organisation for Nuclear Research, CERN. It circulates two proton beams in opposite directions. The beams are not continuous, instead they

consist of discrete bunches. At four points around the ring the beams cross and the bunches collide. Built around these interaction points are the four main LHC experiments: ATLAS, CMS, LHCb and ALICE. Each of these experiments have wide-ranging physics programmes which aim to test the current model and to search for new physics. ALICE is designed to study the high temperature and high density environment produced in heavy ion collisions. LHCb is designed for precision measurements of CP violation and rare decays. ATLAS and CMS are general purpose detectors designed to reconstruct a variety of particles over a wide range of energies.

The studies presented in this thesis all relate to the ATLAS experiment. The ATLAS (**A Toroidal LHC ApparatuS**) detector is often likened to a digital camera. The detector records snapshots, or events, of each collision, comprising the measurements made of the final states of those collisions. Typically, the heavy particles believed to be associated with new physics, the Higgs boson included, decay very quickly and only their decay products can be seen directly in the detector. By studying the signatures left behind we hope to discover and identify any new physics that manifests at high energy. In this thesis, the study of one particular signature that the Higgs boson may produce is presented, the $H \rightarrow ZZ$ channel where one of the Z bosons decays to leptons, and the other to b quarks.

The theory predicts every property of the Higgs boson except for its mass. This search channel is useful if the Higgs boson has a high mass. However, it is not as simple as looking for events with 2 leptons and 2 b quarks. There are other processes that can create the same signature, referred to as backgrounds. From measurements of the final state particles the mass of the

Higgs boson can be reconstructed. The mass distribution of the backgrounds is different from the Higgs signal. The Higgs boson appears as a peak above background in the mass distribution. Many events must be collected to prove that signal has been observed (or that no signal exists).

At design luminosity¹, the LHC will collide bunches of protons at a rate of 40 MHz. It is technically impossible to record events at this rate. Instead, the data must be processed in real time, the signatures of the event identified, and a decision made whether or not to record the event for permanent storage. This job is done by the ATLAS *Trigger*. The Trigger is divided into several levels. The first level systems make a very fast decision (every 25 ns) based on limited information. If an event passes the first level, the data are readout from the detector and processed by the High Level Trigger, where the full event information is available. Only once an event passes this level will it be permanently stored and available for physics analysis.

The first level itself is divided into several sub-systems. One of these sub-systems is the *Calorimeter Trigger*². The Calorimeter Trigger receives signals from the calorimeters, digitises them, and runs algorithms to identify objects such as electrons/photons and jets³. For efficient operation of the Trigger, it is essential that the energies of these signals are accurately measured, that they are assigned to the correct event and that noise is suppressed. To this end, signals are passed through a digital filter. If correctly configured, the

¹Luminosity is a property of the beam that affects how often collisions happen. The event rate is directly proportional to the luminosity.

²A calorimeter is a type of detector which measures a particles energy by stopping and absorbing them.

³Quarks and gluons do not normally exist as free particles, instead they form a *jet* of many composite particles.

digital filter greatly improves the energy measurement, identification of small signals with the correct event, and noise suppression. From the studies presented in this thesis, the initial configuration of the digital filter was decided, and used for data taking during the LHC 2010 run.

Chapter 2

Introduction

The search for the Standard Model Higgs boson [5–7] is one of the main objectives of the ATLAS experiment. The theory predicts all of its properties except for its mass. Direct searches from previous experiments place lower limits around 114 GeV [8]. Theoretical constraints place upper limits on its mass of ~ 1 TeV [9]. The LHC General Purpose Detectors (GPDs) must search for the Higgs boson over this entire mass range. The high mass range is particularly interesting as this region is unexplored by previous lower energy colliders. Also, the discovery of a high mass Higgs Boson would be a strong indication of beyond-the-standard-model (BSM) physics as Standard Model fits to precision electro-weak data prefer a low mass Higgs boson.

At High mass, the channel $H \rightarrow ZZ \rightarrow lll$ provides a beautifully clean signature. However, it is statistically limited. The focus of this thesis is the channel $H \rightarrow ZZ \rightarrow llbb$. While this channel suffers from larger backgrounds, it has a higher branching fraction than the 4 lepton channel. This channel may be used to improve the combined search sensitivity of the experiment.

It may also provide an independent cross-check should a high mass excess be observed.

In chapter 3 the theoretical motivations for the Higgs mechanism, the properties of the Higgs boson and the current limits imposed on its mass are reviewed. LEP (Large Electron Positron collider) In chapter 4 the LHC and the ATLAS detector are described. In chapter 5 a study of the sensitivity to the Standard Model Higgs boson in the decay channel $H \rightarrow ZZ \rightarrow llbb$ is presented. Chapter 6 shows background studies with early data.

At the front-line of LHC physics is the Trigger: a physicist cannot analyse events that were not written to disk! The huge event rate at the LHC makes it unfeasible to readout and record every event. The Trigger must reject most events while retaining events with signatures of interest.

The ATLAS trigger is divided into multiple levels. The first level is implemented in custom-built hardware and makes a real-time decision to accept or reject events based on reduced information. If the first level Trigger accepts the event the entire detector is readout and the information is passed to the High Level Trigger. The High Level Trigger algorithms are implemented in software running on large computer farms and make the final trigger decision using the full detector information.

The first level trigger is further divided into subsystems. The focus of this thesis is the first level Calorimeter Trigger. The Calorimeter Trigger uses reduced granularity information from the calorimeters to search for high E_T e , γ , τ and jets as well as identifying high E_T^{miss} and total E_T events. Signals from the calorimeters are pre-processed to determine their energy and timing before being transmitted to the Processor modules which implement

the trigger algorithms. During the pre-processing, input signals are passed through a Finite Impulse Response (FIR) filter. This filter increases the signal to noise ratio and improves the energy measurement, noise rejection and bunch crossing assignment. In this thesis a study to determine the optimum filter coefficients is presented. The performance of these filters is investigated with commissioning data and cross-checks of the calibration with initial beam data are shown. From the studies presented in this thesis, the initial configuration of the digital filter was decided, and used for data taking during the LHC 2010 run.

An overview of the ATLAS Trigger can be found in chapter 4. In chapter 7 the ATLAS Level-1 Calorimeter Trigger is described in detail. In chapter 8 a study of the digital filter for the Calorimeter Trigger is described. In chapter 9 the results and conclusions are summarised.

Chapter 3

The Higgs Mechanism and Constraints on the Higgs Boson Mass

Theories based on the gauge principle, namely QED and QCD, can successfully describe the electromagnetic and strong forces. However, gauge theories alone are unable to explain the weak force, where the mediating bosons are massive. In the Standard Model, the boson masses are generated by the Higgs mechanism [5–7]. This also introduces a new particle: the Higgs boson, which has not yet been observed in experiment. In this section, electroweak theory and the Higgs mechanism are briefly summarised. The properties of the Higgs boson are discussed and the current theoretical and experimental limits on its mass are reviewed. This topic is extensively covered in the literature and more information can be found in references [10–12].

3.1 Higgs Mechanism

The electroweak part of the Standard Model Lagrangian, is derived by requiring local gauge invariance under the transformations described by the group $U(1)_Y \times SU(2)_L$, where $U(1)_Y$ corresponds to phase-transformations of hyper-charge, Y , and $SU(2)_L$ corresponds to rotations in weak-isospin space. Requiring this symmetry, introduces one field and coupling associated with the $U(1)_Y$ symmetry, and three fields and one coupling g , associated with the $SU(2)_L$ symmetry. However, these fields do not correspond to the bosons of the weak and electromagnetic force observed in nature. In the Standard Model, the Higgs mechanism is invoked to break the symmetry and reproduce the observed gauge bosons.

The symmetry is broken by the inclusion of Φ , a weak isospin doublet of complex scalar fields,

$$\Phi = \begin{pmatrix} \Phi^+ \\ \Phi^0 \end{pmatrix} = \sqrt{\frac{1}{2}} \begin{pmatrix} \Phi_1 + i\Phi_2 \\ \Phi_3 + i\Phi_4 \end{pmatrix}. \quad (3.1)$$

The Lagrangian for a scalar field in a potential is,

$$\mathcal{L}_{\text{Higgs}} = (\mathbf{D}_\mu \Phi)^\dagger (\mathbf{D}^\mu \Phi) - V(\Phi), \quad (3.2)$$

where \mathbf{D}^μ is the covariant derivative.

The potential assumed in the Standard Model is,

$$V(\Phi) = -\mu^2 \Phi^\dagger \Phi + \lambda (\Phi^\dagger \Phi)^2. \quad (3.3)$$

A diagram of this potential is shown in Figure 3.1. This potential introduces two parameters into the theory, μ and λ . If λ is positive and μ^2 is negative, then the potential has a minimum at $\Phi^\dagger\Phi = 0$. If λ is negative then the potential falls off to negative infinity at large Φ and the vacuum would be unstable. If both μ^2 and λ are positive, then there is a maximum at the origin. Instead, the stable minima lie at $\Phi^\dagger\Phi = \frac{1}{2}\mu^2/\lambda$. Thus, in the ground state the field Φ has a vacuum expectation value, v ,

$$\langle 0|\Phi|0\rangle = \frac{v}{\sqrt{2}}, \quad \text{with } v \equiv \frac{\mu}{\sqrt{\lambda}}. \quad (3.4)$$

The ground state is degenerate so one must be chosen. In the Standard Model it is chosen to be,

$$\Phi_0 = \sqrt{\frac{1}{2}} \begin{pmatrix} 0 \\ v \end{pmatrix}. \quad (3.5)$$

Φ can be re-written in terms of an expansion around this vacuum,

$$\Phi = \sqrt{\frac{1}{2}} \begin{pmatrix} 0 \\ v + H \end{pmatrix}, \quad (3.6)$$

where the scalar field H is the expansion in the radial direction, and is the physical field that is associated with the Higgs Boson.¹

Substituting equation 3.6 into equation 3.2 has the effect of mixing the gauge fields together to form the physical gauge bosons. This also generates

¹Only H is a physically observable field. The remaining three fields can be removed with a careful choice of gauge. These are massless ‘‘Goldstone Bosons’’ and are described in more detail in the referenced material.

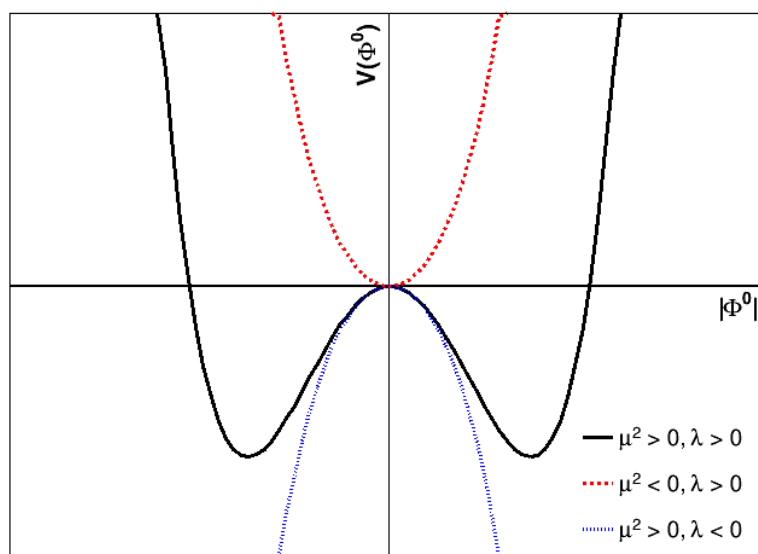


Figure 3.1: The Higgs potential of the Standard Model as described by equation 3.3. Three possible sets of the parameters, μ^2 and λ are shown. These are described in the text.

mass terms for the W and Z bosons but leaves the photon massless. The fermion masses can also be generated by adding interaction terms with the same Higgs doublet.

Finally, the Higgs boson itself has mass. Substituting 3.6 into equation 3.3 provides mass and self interaction terms for the Higgs field, H . The resulting mass is,

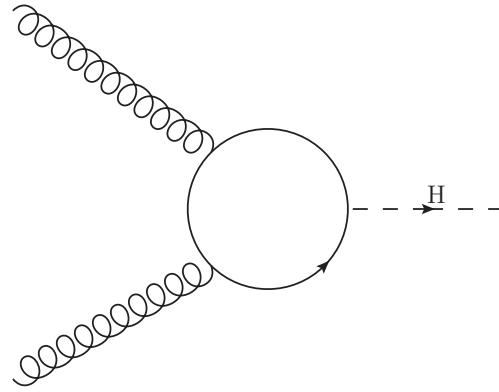
$$m_H = \sqrt{2\lambda}v. \quad (3.7)$$

The vacuum expectation value, v , can be determined from experiment (with measurements of G_F). λ has not been directly measured in experiment, therefore, the Higgs boson mass is not predicted by the theory. However, it is possible to set constraints on this parameter as described in section 3.3.

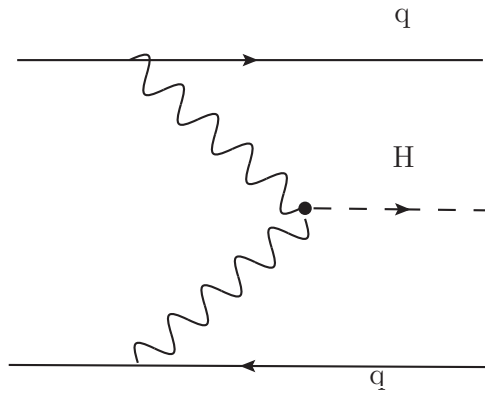
The inclusion of the Higgs doublet in the Standard Model Lagrangian provides a mechanism for generating masses for the W^\pm and Z bosons while leaving the photon massless. The interaction between this doublet and the fermions generates masses for them as well. The theory predicts a massive neutral scalar boson that couples to the fermions in proportion to their mass.

3.2 Higgs Boson Decay Properties and Production at the LHC

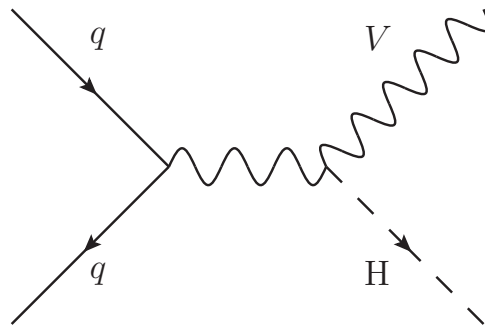
The leading order Feynman diagrams for Higgs boson production at the LHC are shown in Figure 3.2 and their predicted cross-sections are shown in Figure 3.3. Gluon fusion is the dominant process, though this cannot proceed directly as the Higgs boson does not couple to the gluon. Instead the process



(a) $gg \rightarrow H$



(b) $qq \rightarrow qqH$



(c) $qq \rightarrow VH$

Figure 3.2: Main Higgs production mechanisms at the LHC. (a) gluon fusion, (b) vector boson fusion, and (c) associated production, where V is W or Z .

goes via a quark loop, with the dominant contribution from the top quark as this is the heaviest known strongly interacting particle. There are other production mechanisms where the Higgs boson is produced in association with other particles. For example vector boson fusion with a final state qqH , or associated production with a final state WH or ZH . Though these have lower production cross-sections, the additional particles provide signatures that can be useful in selecting Higgs events in order to reduce backgrounds.

The decay properties of the Higgs boson are strongly dependent on its mass. As the couplings to fermions are proportional to the masses of the decay particles, the Higgs boson preferentially decays into the highest mass fermion that is kinematically allowed.

Figure 3.4 shows the branching fractions for Higgs boson decays as a function of mass. For masses below $m_H \approx 130$ GeV the channel $H \rightarrow b\bar{b}$ dominates. Unfortunately, this is a particularly difficult channel at a hadron collider such as the LHC due to the very large backgrounds. Searches for this decay mode typically require that the Higgs is produced in association with other particles. For example, the ZH channel where $Z \rightarrow ee$ or $Z \rightarrow \mu\mu$ provides two leptons that can be used to identify these events and allow them to efficiently pass the trigger. Alternatively, decay modes with lower branching fractions, such as $H \rightarrow \gamma\gamma$ can be exploited due to their low backgrounds.

At high masses, the Higgs boson decays to pairs of weak bosons, $H \rightarrow ZZ$ and $H \rightarrow W^+W^-$. Where one or more of the gauge bosons decays leptonically these provide an experimentally identifiable signature. The clearest signal, the so called “golden channel”, is $H \rightarrow ZZ \rightarrow l^-l^+l^-l^+$ where

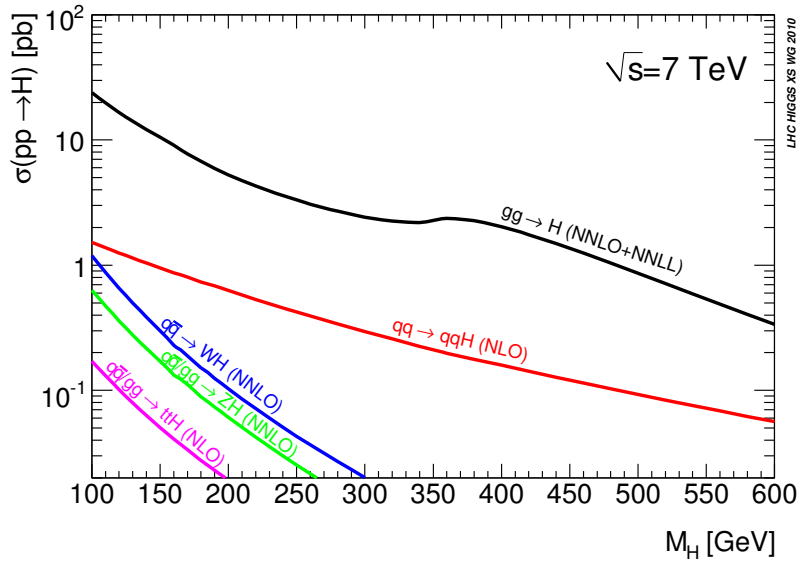


Figure 3.3: Standard Model Higgs boson production cross-sections for proton-proton collisions with a centre-of-mass energy of 7 TeV [13].

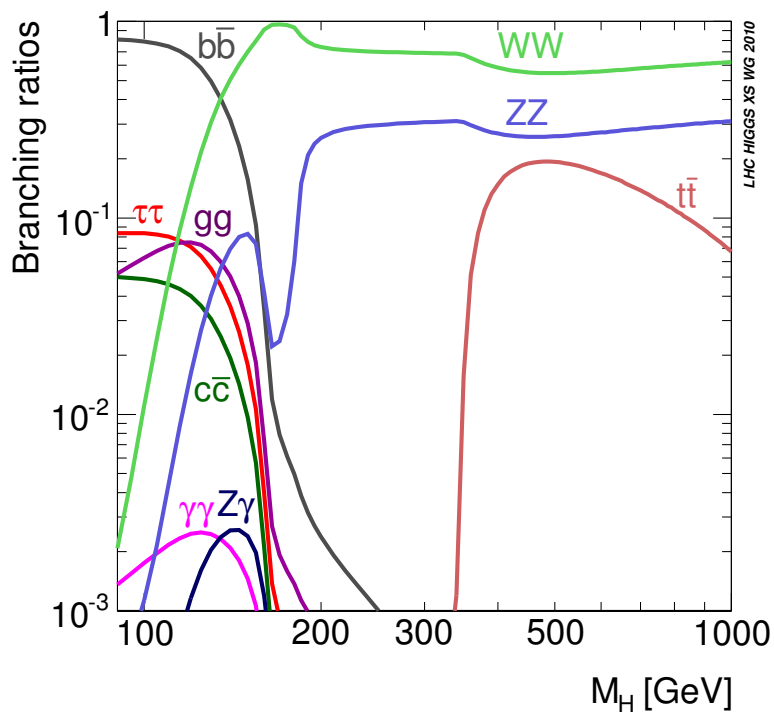


Figure 3.4: Branching fractions for Standard Model Higgs boson decays [13].

$l^\pm = e^\pm$ or μ^\pm . The dominant background to this channel comes from the irreducible di- Z -boson production.

The width of the Higgs boson resonance also has a strong dependence on its mass. This is shown in Figure 3.5. At low mass the width is very narrow, much narrower than typical experimental resolution. As the mass increases more decay modes become accessible, with stronger couplings, causing the width to increase. At very high mass, $O(1 \text{ TeV})$, the Higgs has a width almost equal to its own mass. This behaviour affects the experimental sensitivity; as the resonance becomes broader it becomes more difficult to distinguish from the background.

The focus of this thesis is the very high mass region, $m_H \gtrsim 200 \text{ GeV}$ where both gauge bosons are on mass shell. In this case the sensitivity of searches in the $H \rightarrow ZZ \rightarrow lll$ channel is statistically limited with the relatively low

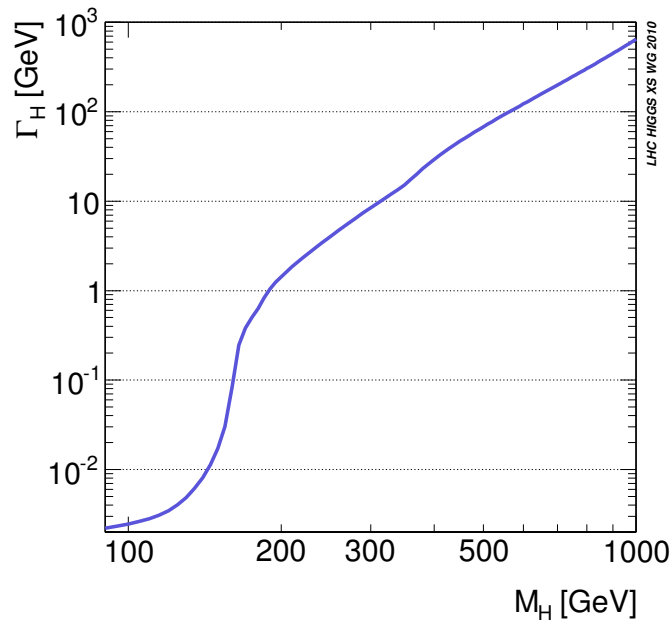


Figure 3.5: Standard Model Higgs boson total width [13].

luminosity expected in the early years of LHC running. Chapter 5, shows that the search sensitivity can be improved by the inclusion of other decay modes, including $H \rightarrow ZZ \rightarrow llbb$.

3.3 Constraints on m_H

Direct searches for the Higgs boson at collider experiments have yet to observe a statistically significant signal. However, upper limits have been placed on the production cross-sections for the Higgs boson and some mass regions have been excluded (assuming Standard Model cross-section). Searches at LEP have excluded the mass range $m_H < 114$ GeV at 95% confidence limit [8]. To date, searches at the Tevatron have excluded the mass range $158 \text{ GeV} < m_H < 175 \text{ GeV}$ at 95% confidence limit [14]. At the time of writing, the Tevatron experiments continue to collect data, and these limits are expected to change. The combined limits are shown in Figure 3.6.

While the Standard Model does not predict the Higgs boson mass, it is still possible to put constraints on m_H . To complete this chapter, these indirect limits will be summarised and their impact on searches at the LHC discussed.

Without a Higgs boson, the cross-section for $W^+W^- \rightarrow W^+W^-$, shown in figure 3.7, is proportional to s ; as s tends to infinity the probability for this process diverges. When the Higgs mechanism is introduced then the additional Feynman diagrams cancel this divergence leaving a term proportional to m_H^2 . The divergence in the high energy limit is fixed, however, unitarity can still be violated if m_H is too large. This imposes the limit

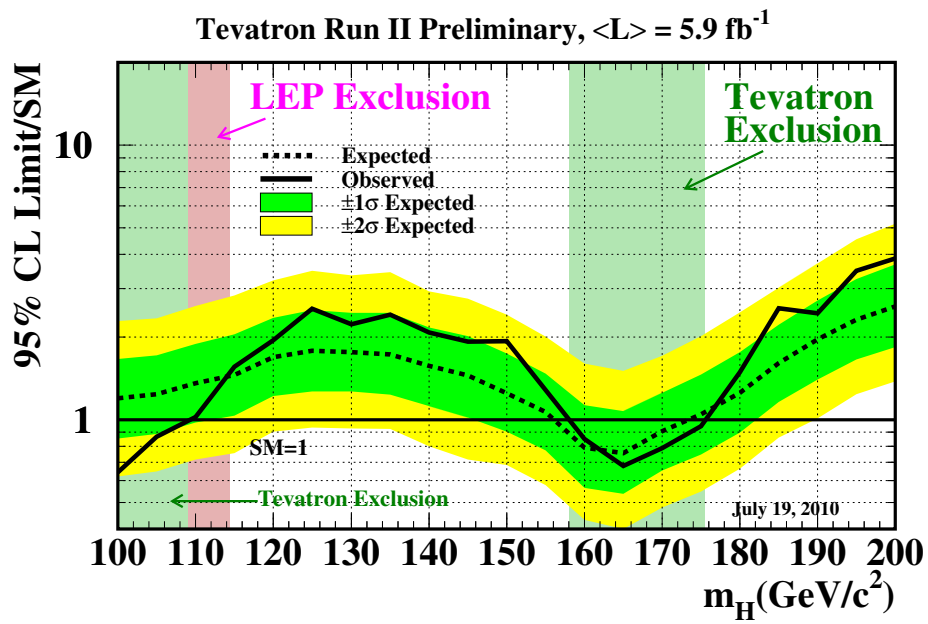


Figure 3.6: 95% confidence limits on m_H from direct searches. The Tevatron combined limits are shown as a multiple of the predicted Standard Model cross-section. The excluded mass ranges are highlighted in red (excluded by LEP) and light green (excluded by the Tevatron) [14].

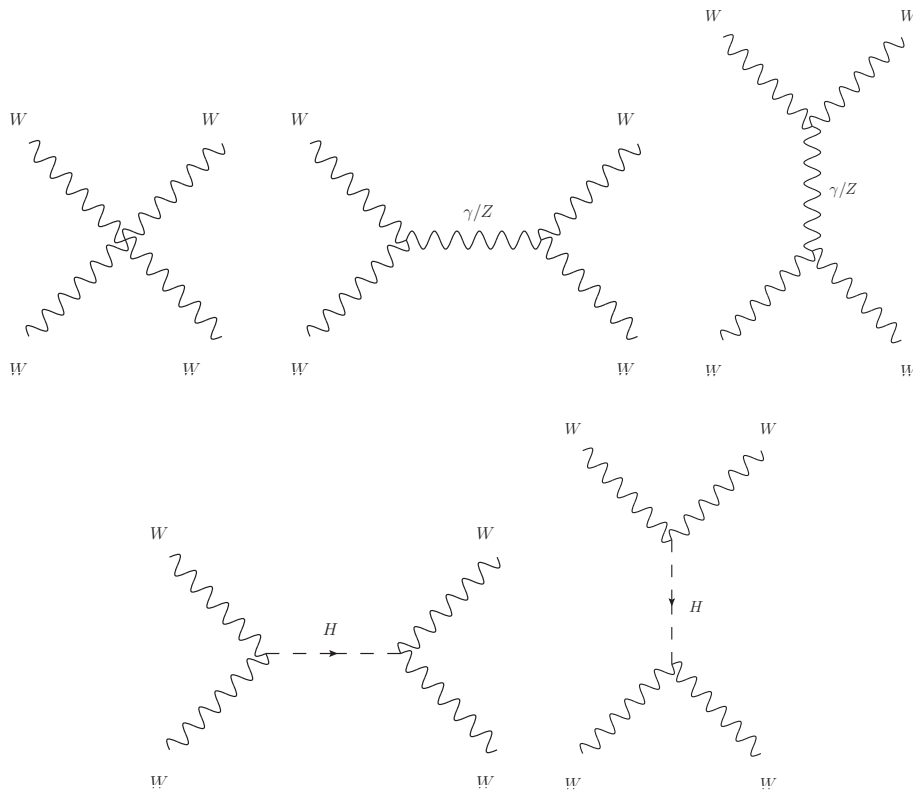


Figure 3.7: Leading order Feynman diagrams for WW scattering. Without the diagrams involving the Higgs boson the probability for this process diverges.

$m_H \lesssim 1 \text{ TeV}$ [9].

As with all coupling constants in the Standard Model, λ (which given that the vacuum expectation value is known determines m_H) changes with the energy scale. Two separate constraints can be placed on λ . Firstly, λ must remain positive, otherwise the vacuum is unstable (see the discussion in section 3.1). This imposes a lower bound on m_H . Secondly, λ increases with energy and at some energy scale perturbation theory breaks down. This imposes an upper limit on λ . These should not be interpreted as direct limits on m_H , instead they are limits on the energy scale at which new physics must become important. These limits are shown in Figure 3.8. If the Standard Model is to survive up to the Plank scale then this imposes the constraint $m_H \lesssim 180 \text{ GeV}$ [15]. If new physics has important effects at the TeV scale the constraints are much less stringent.

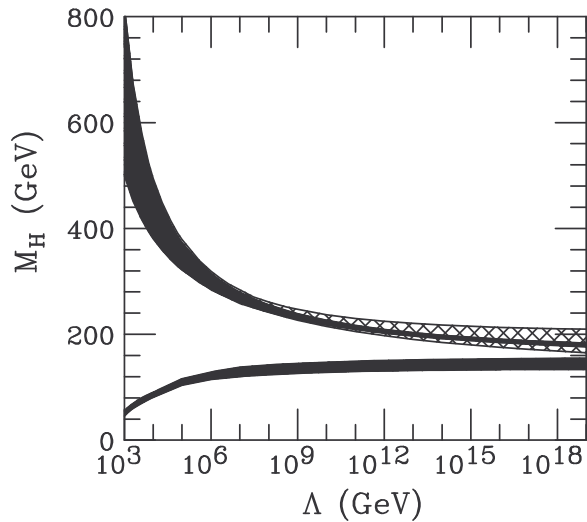


Figure 3.8: Limits on m_H from the running of the coupling λ . The lower band indicates the scale, Λ , at which the vacuum becomes unstable. The upper band indicates the scale at which the theory becomes non-perturbative. The widths of the grey bands indicate the theory uncertainty [15].

The Standard Model Higgs boson has not been directly observed, however, it can make corrections to measured parameters via virtual loops. By fitting the theory to precision measurements of the parameters of the Standard Model, it is possible to extract the Higgs mass. Results from the LEP electroweak fitting group, shown in figure 3.9, favour a low Higgs mass. When the fit is performed without using input from direct searches the preferred value is $m_H = 89^{+35}_{-26}$ GeV [16].

The focus of this thesis is searches for a high mass Higgs boson. Given that the electroweak fits to the Standard Model favour a low mass, one could ask the question: why study the high mass range at all? The electroweak fits assume that the Standard Model is the correct theory of nature. It is known that the Standard Model cannot be a complete theory. If there exists new physics, that modifies the Standard Model on the weak-scale, the electroweak fits would be invalid. Similar fits have been performed with BSM physics included (for examples see [17] and [18]). When new physics is included, the Higgs boson is often free to take much larger masses than those allowed by the Standard Model only fits. Also, from a purely pragmatic point-of-view, limits can be set on the high mass region with relatively small amounts of integrated luminosity at the LHC (assuming Standard Model cross-sections and branching fractions) compared with the difficult low mass range.

The prospect for an early discovery, as well as the potential to provide insight on BSM physics, makes high mass Higgs boson searches an interesting area for studies with early LHC data.

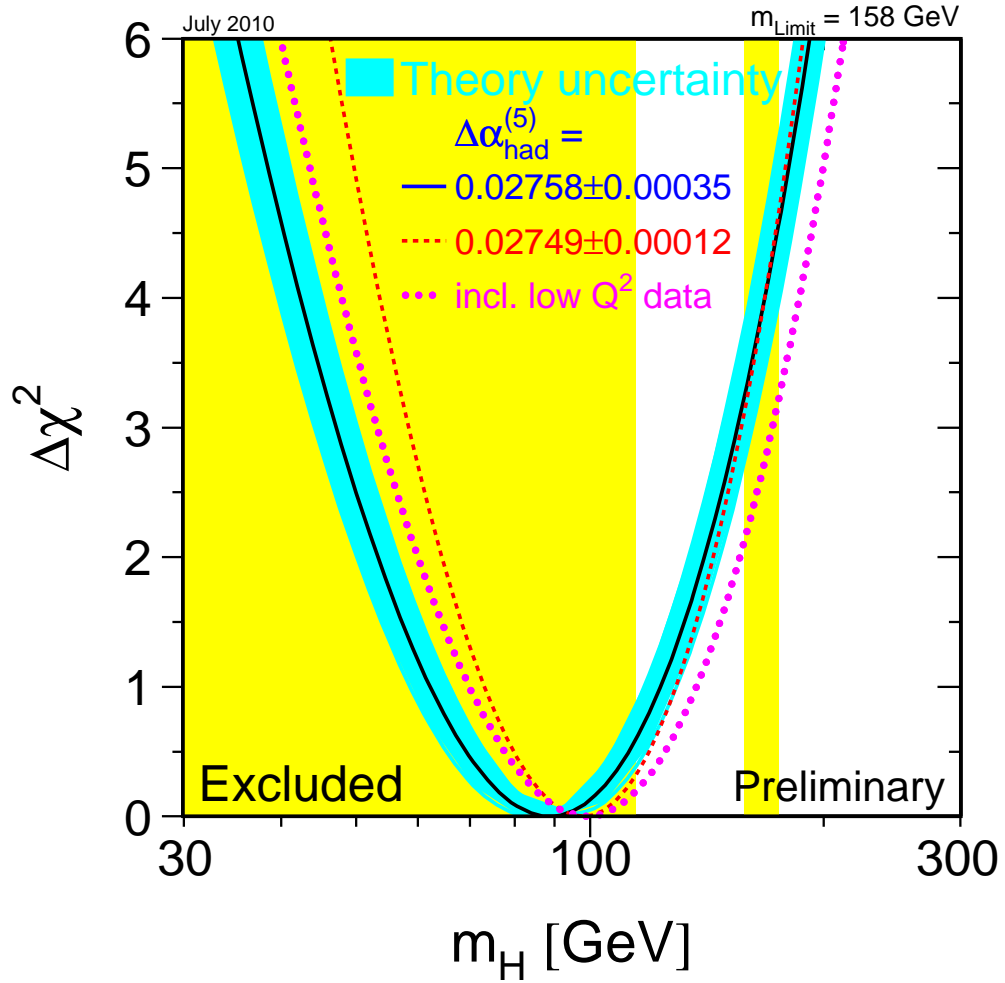


Figure 3.9: Results of fits to precision electroweak data [16]. The deviation of χ^2 from the minimum value as a function of m_H is shown. The yellow bands show the regions excluded at 95% confidence limit by direct searches at the Tevatron and LEP. Several curves are plotted using different input data. All of the fits favour a low mass Higgs. Indeed, the minima all lie in the LEP excluded region.

Chapter 4

The LHC and the ATLAS Detector

4.1 The Large Hadron Collider

The LHC is a superconducting hadron accelerator and collider installed in a 26.7 km ring beneath the French-Swiss countryside [19]. The ring consists of 8 arc sections and 8 straight sections. The arc sections contain the bending magnets and the straight sections contain the 4 main experiments (the remaining 4 are a relic from the preceding accelerator, LEP, where more RF cavities were required to compensate for synchrotron radiation).

It is a particle-particle collider, hence two beam pipes are required. To reduce cost and space a double-magnet design is used where a single superconducting magnet can provide an opposite field to both beams. Most of the LHC running time is devoted to proton-proton collisions.

The most important parameters of a collider are the luminosity and

centre-of-mass energy. The luminosity is defined as the proportionality between event rate, W , and the cross-section for a process, σ ,

$$W = L\sigma. \quad (4.1)$$

Such a definition is useful as the luminosity contains information about the experiment (i.e. beam parameters) and the cross-section contains information about the physics of the process. For two colliding beams with the same properties the luminosity is given by,

$$L = \frac{kN^2f}{4\pi\sigma_x\sigma_y}, \quad (4.2)$$

where k is the number of bunches, N is the number of particles per bunch, f is the revolution frequency and σ_x, σ_y are the transverse sizes of each bunch in the x and y directions [20].

The LHC has a design centre-of-mass energy of $\sqrt{s} = 14$ TeV and luminosity of $10^{34}\text{cm}^{-2}\text{s}^{-1}$ for proton-proton collisions. This luminosity is approximately equivalent to $860\text{pb}^{-1}\text{day}^{-1}$. In the 2010 proton run, the LHC achieved a centre-of-mass energy of $\sqrt{s} = 7$ TeV and a peak instantaneous luminosity of $2.1 \times 10^{32}\text{cm}^{-2}\text{s}^{-1}$ and ATLAS recorded a total of 45pb^{-1} with stable beams. To put these numbers into context, the Standard Model production cross-section for a 200 GeV Higgs boson is $\sim 5\text{pb}$ at $\sqrt{s} = 7$ TeV and $\sim 20\text{pb}$ at $\sqrt{s} = 14$ TeV [13]. These cross-sections are many orders of magnitude below the total cross-section for pp scattering ($\sim 0.1\text{b}$).

Such high luminosity is necessary in order to observe very low cross-

section processes. However, this comes at a price: at peak luminosity there will be on average ~ 23 pile-up interactions per event [21]. This adds additional background and makes reconstructing and understanding LHC events difficult.

4.2 ATLAS

ATLAS is a general purpose particle physics experiment. It is a “discovery” experiment and is capable of looking at a wide variety of signals. It was designed to reconstruct and accurately measure particles in the complicated environment provided by the LHC up to very high energies. The detector, shown in Figure 4.1 is huge in both size and complexity. Design, construction and installation has taken 15 years and the work of thousands of physicists, engineers and technicians. The combined detector weighs 7000 tonnes and is 46 m long and 25 m in diameter. The performance goals of ATLAS are shown in table 4.1.

Table 4.1: The performance goals of the ATLAS sub-detectors. E and p_T are in units of GeV [22].

Detector component	Required resolution
Tracking	$\sigma_{p_T}/p_T = 0.05\%p_T \oplus 1\%$
EM Calorimetry	$\sigma_E/E = 10\%/\sqrt{E} \oplus 0.7\%$
Hadronic calorimetry	$\sigma_E/E = 50\%/\sqrt{E} \oplus 3\%$
Forward calorimetry	$\sigma_E/E = 100\%/\sqrt{E} \oplus 10\%$
Muon spectrometer	$\sigma_{p_T}/p_T = 10\%$ at $p_T = 1\text{TeV}$

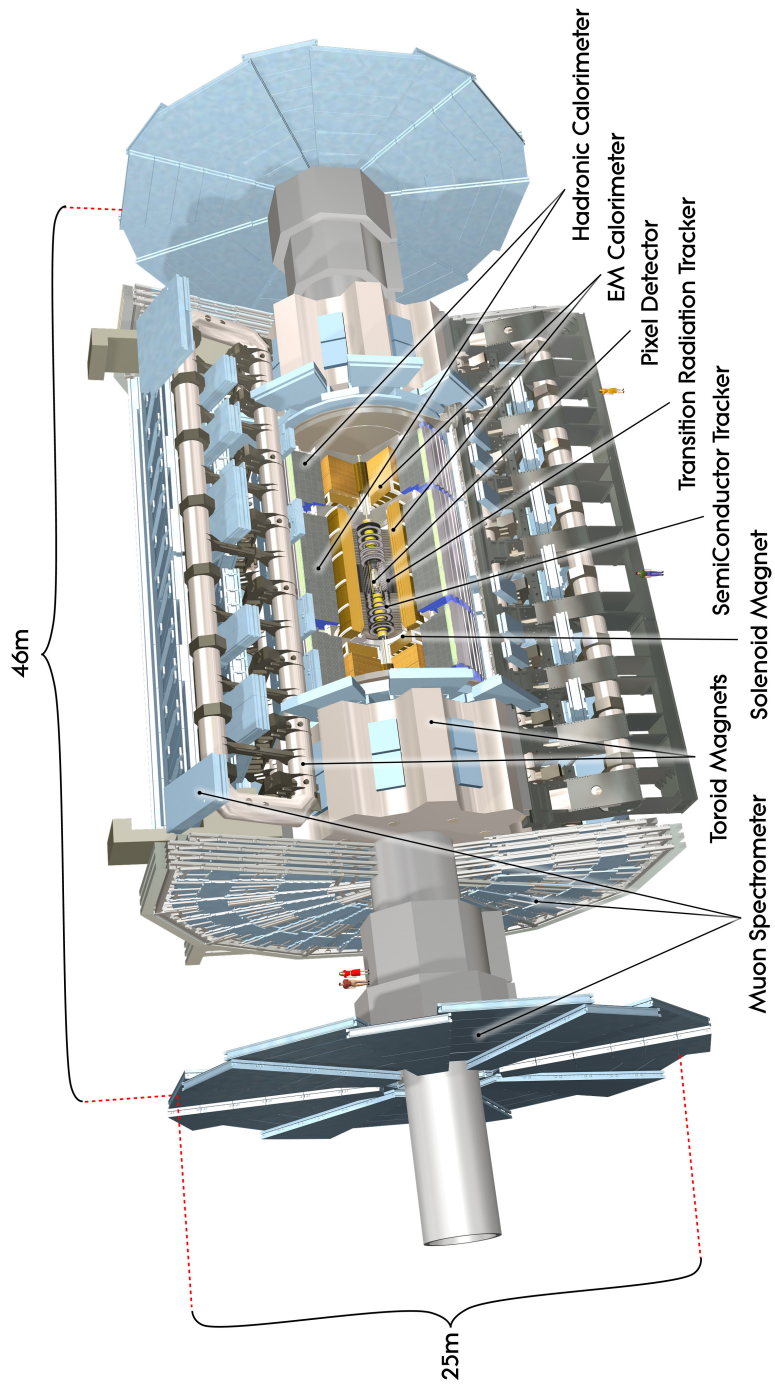


Figure 4.1: A cut away view of the ATLAS detector showing its main components [22].

ATLAS has a cylindrical, layered structure consisting of several sub-detectors: the inner tracking detectors are used to measure the momenta of charged particles, the calorimeters are used to measure the energy of particles by stopping and absorbing them, and the muon spectrometers are used to measure the momenta of muons (typically the only charged particles capable of penetrating the calorimeters). In the following sections, the sub-detectors that make up ATLAS are described [22]. An overview of the coverage of these detectors is shown in Figure 4.2.

4.2.1 Nomenclature

In ATLAS the z -direction is defined as parallel to the beam direction. The positive x -direction points to the centre of the LHC ring and the positive y -direction points upwards towards the surface. The half of the detector in the positive z region is referred to as side-A and the half in the negative z region is referred to as side-C. ϕ is the azimuthal co-ordinate around the beam axis.

Transverse momentum, p_T , is the component of momentum in the x - y plane. Often p_T is used rather than momentum, p , because in hadron collisions the lab frame is not the centre-of-mass frame, even with equal beam energies. This is because protons are composite objects and, in a hard scatter, it is the partons within the hadron which scatter in a collision. Each parton carries an unknown fraction of the hadron momentum. In any collision all transverse momenta should balance out to zero. Similarly, transverse

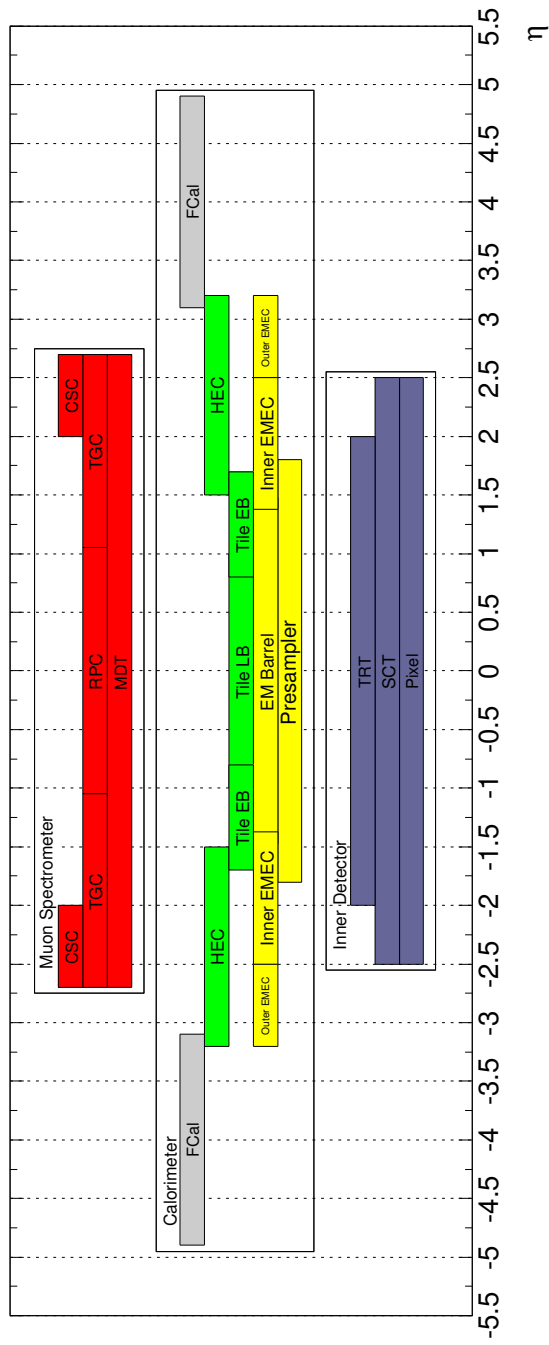


Figure 4.2: A diagram showing the η coverage of each sub-detector in ATLAS. In blue are the inner tracking detectors including the Pixel Sensors, the Silicon-microstrip Tracker (SCT) and the Transition Radiation Tracker (TRT). In yellow are the e.m. calorimeters including the Presampler, the EM Barrel and the Electro-magnetic End-cap (EMEC). In green are the hadronic calorimeters including the Tile Long Barrel (Tile LB), the Tile Extended Barrel (Tile EB) and the Hadronic End-cap (HEC). In grey are the Forward Calorimeters (FCals). In red are the muon detectors, Monitored Drift Tubes (MDTs), Resistive Plate Chambers (RPCs), Thin Gap Chambers (TGCs) and Cathode Strip Chambers (CSCs).

energy, E_T , is used instead of energy, E , and is defined as,

$$E_T = E \sin \theta. \quad (4.3)$$

Pseudo-rapidity, η , is often used rather than the polar angle, θ . Rapidity, y , is defined as,

$$y = \frac{1}{2} \ln \left| \frac{E + p_z}{E - p_z} \right|. \quad (4.4)$$

A Lorentz boost in the z -direction simply adds a constant. Hence the shape of a y -distribution is invariant under such transformations. In the ultra-relativistic limit this becomes equivalent to pseudo-rapidity,

$$\eta = -\ln(\tan(\theta/2)). \quad (4.5)$$

Neutrinos rarely interact with matter and so escape the detector unseen. Their presence can be inferred from an imbalance in the p_T of the particles that are observed. This is referred to as missing transverse momentum, the magnitude of which is missing transverse energy, E_T^{miss} .

4.2.2 Tracking

The high level of pile-up expected when the LHC reaches high luminosity, combined with the intrinsically “busy” nature of hadron collisions, demands that the ATLAS detector has excellent tracking to cope with the high track multiplicity expected. At peak luminosity each collision will produce in the order of 1000 particles in $|\eta| < 2.5$ which is the range of the inner tracking. High granularity detectors are required to disentangle such events. Three

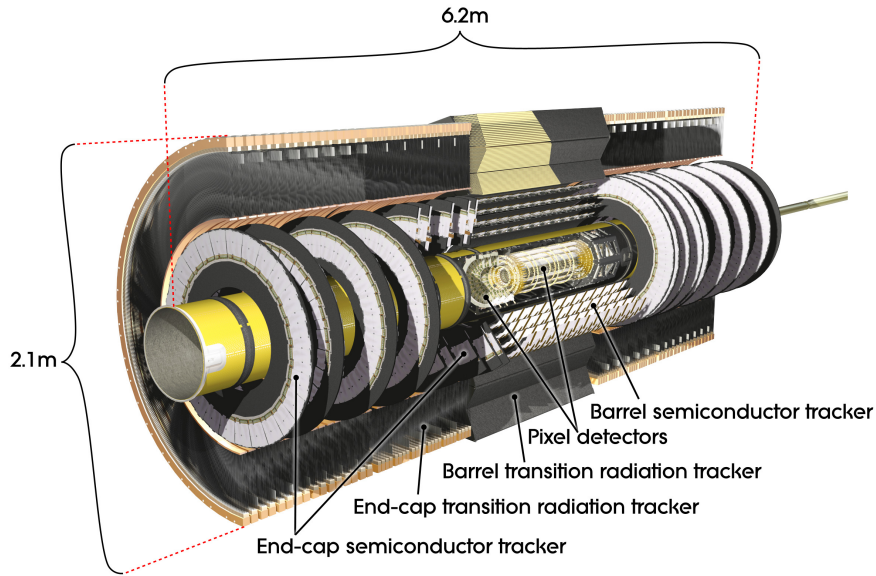


Figure 4.3: A three-dimensional representation of the ATLAS inner detector. Depicted (from centre outwards) are the pixel sensors, the SCT and the TRT [22].

sub-detectors combine to make the inner detector in ATLAS: the Pixel Sensors, Silicon-microstrip Tracker (SCT) and the Transition Radiation Tracker (TRT). These are shown in figure 4.3. Momentum is measured from the curvature of a track in a magnetic field, which is supplied by a super-conducting solenoid surrounding the inner detector. This provides a 2 T field parallel to the beam direction.

Pixel Sensors

The closest to the interaction point is the semi-conductor pixel detector. This provides the highest position resolution and granularity of the three detectors. There are over 80 million channels. Each cell (of size $50 \times 400 \mu\text{m}$ in ϕ - z) gives a precise measurement of all three dimensions of a particles

position. The pixel sensors are responsible for detecting secondary vertices, which allows the tagging of short lived particles such as B -hadrons and τ -leptons. Typically each track crosses 3 pixel layers. Tracks are fitted through these points and can be extrapolated back to the interaction point. If tracks from particles do not cross at the primary interaction point a secondary vertex is detected which indicates the decay in-flight of a short lived particle.

The pixels must survive in a high-radiation environment. To reduce noise from radiation damage the sensors are operated at a temperature around -10°C . Nevertheless, the inner layer of the pixel sensors will need to be replaced after 3 years of high luminosity running.

Semi-Conductor Tracker

The semiconductor tracker surrounding the pixel detector consists of long silicon strips $80\ \mu\text{m}$ in width but $64\ \text{mm}$ long. This reduces the total number of channels to read out (approx 6 million), however, the strips do not provide a full measurement of position. It cannot be determined where along a strip a hit happens, only two components of the position vector can be resolved. To compensate for this the layers are double-sided. Strips on either side are placed at an angle of $40\ \text{mrad}$. By combining hits at two strips, all three spatial co-ordinates of the hit can be reconstructed. The semiconductor tracker complements the measurements of the pixel and transition radiation detectors. Typically, each track crosses eight strips which corresponds to 4 position measurements.

Transition Radiation Tracking

Finally, the transition radiation tracker covers a large volume but has a lower granularity (with a total of 300,000 channels). It is made up of straw tube detectors containing xenon gas. Each straw tube is 4mm in diameter. The reduced granularity is compensated by the increased number of hits and larger volume. Typically, 36 measurements are made along each track. Charged particles traversing the detector ionise the xenon gas. The liberated electrons travel towards the cathode with a known drift velocity. Therefore, the position of the hit can be measured from the drift-time of electrons. The primary purpose of this detector is to measure the curvature of the tracks. They are also capable of electron identification through the measurement of transition radiation. Transition radiation is emitted by a charged particle when it moves between materials with different dielectric constants [23]. The total transition radiation emitted is dependent on the particle's Lorentz factor. Hence, measurement of transition radiation allows electrons to be distinguished from other charged particles due to their very small mass and thus higher Lorentz factor.

4.2.3 Calorimetry

While the tracking detectors only detect charged particles, all particles (with the exception of neutrinos) deposit some energy in the calorimeters. Calorimeters complement the momentum measurement from the inner detector as their resolution improves with energy, whereas the ID momentum resolution gets worse at high energy. The calorimeters must also contain the e.m. and

hadronic showers they cause to prevent punch-through to the muon system. The electromagnetic calorimetry is approximately 22 radiation lengths deep. In total the calorimetry is approximately 9.7 nuclear interaction lengths. The calorimetry is depicted in Figure 4.4. The ATLAS calorimetry consists of LAr calorimeters surrounded by the tile calorimeter. In the very forward regions specialised LAr forward calorimeters are installed, which are designed for the harsh environment.

Electromagnetic Calorimetry

Electromagnetic calorimeters are designed for the detection and measurement of electrons and photons. Within the calorimeter an electromagnetic shower of particles is created through repeated bremsstrahlung radiation and

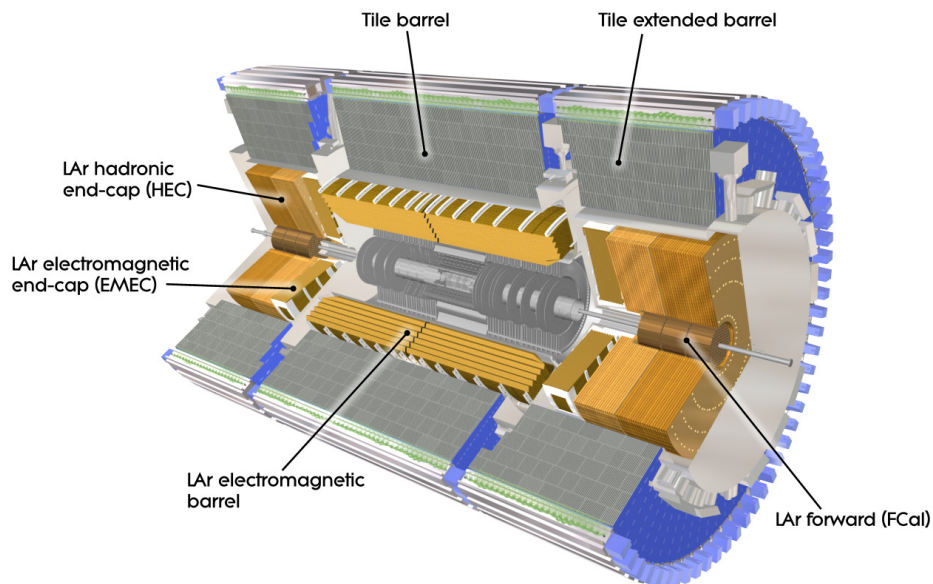


Figure 4.4: A three-dimensional representation of the ATLAS calorimetry [22].

electron-positron pair production. Electromagnetic showers are simple and well understood. Thus, e.m. calorimeters provide better energy resolution than their hadronic counterparts.

The e.m. calorimeters are sampling calorimeters with liquid Argon active layers and lead absorber layers. In a sampling calorimeter plates of a dense material are used to induce showers. Placed between the plates is an active medium which measures the ionisation caused by shower particles. The use of liquid Argon necessitates the cryostats in which the calorimeters are contained. To reduce the amount of material in front of the calorimeter, its cryostats are integrated into the solenoid cryostat. The e.m. calorimeter is divided into 3 sub-detectors: the LAr Barrel, and two end-caps. The e.m. calorimeter has a so-called “accordion” geometry, designed to provide full ϕ symmetry and complete ϕ coverage.

The e.m. calorimeter has fine granularity over the η range of the precision tracking ($\eta \times \phi = 0.025 \times 0.025$ in places) for precision measurements of electrons and photons. Lower granularity is used in the region $|\eta| > 2.5$ where precision electron and photon measurements are not possible. The e.m. calorimeter is also segmented longitudinally into 3 layers.

In the region $|\eta| < 1.8$ a pre-sampler detector is placed before the solenoid. This is used to correct for the energy lost before particles enter the calorimeter.

Hadronic Calorimetry

Hadronic calorimeters are designed to measure the energy of jets and hadrons. Unlike e.m. showers, the content of hadronic showers fluctuates between

events. Much of the energy can go unmeasured through the creation of neutrinos and muons within the shower or in nuclear excitation or spallation. This is the reason for the intrinsically lower energy resolution of hadronic calorimeters.

The hadronic calorimetry uses steel as an absorber layer and scintillator tiles for the active part in the barrel region. The light produced is measured by photo-multiplier tubes. The scintillator tiles are orientated perpendicular to the beam line (i.e. they lie parallel to the x - y plane). As with the LAr accordion geometry this allows almost full ϕ coverage. The Tile calorimeter is separated into three sections: a central barrel calorimeter and the extended barrel calorimeters which surround the end-caps.

LAr is used again (with copper as the absorber layer) in the end-caps due to the high radiation environment. Finally, another LAr based system within the end-caps provides forward calorimetry.

4.2.4 Muon Spectrometer

A large proportion of the volume of ATLAS is the muon spectrometer, shown in figures 4.5 and 4.6. Three toroidal magnets provide the magnetic field for the muon system: one in the barrel region and one for each end-cap. Each toroid consists of a set of 8 super-conducting coils. The toroidal magnets provide a field mostly orthogonal to the muon momentum while minimising the effects of multiple scattering. Four types of chambers are used: Monitored Drift Tubes (MDTs) and Cathode Strip Chambers (CSCs) provide precision measurements in the bending plane (R - z). Faster Resistive Plate Chambers

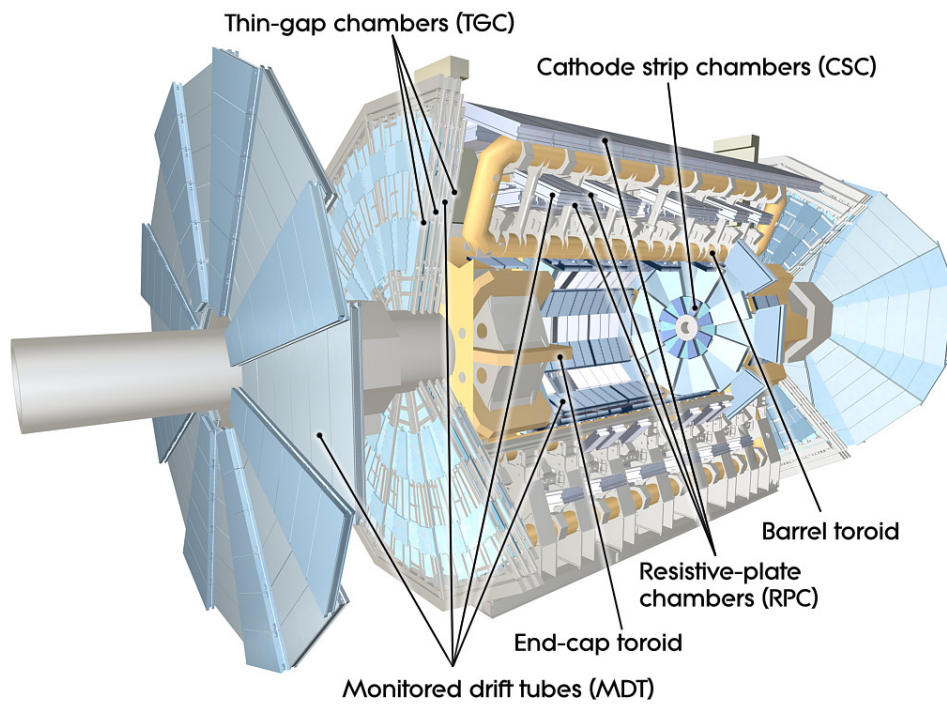


Figure 4.5: A three-dimensional representation of the ATLAS muon spectrometer [22].

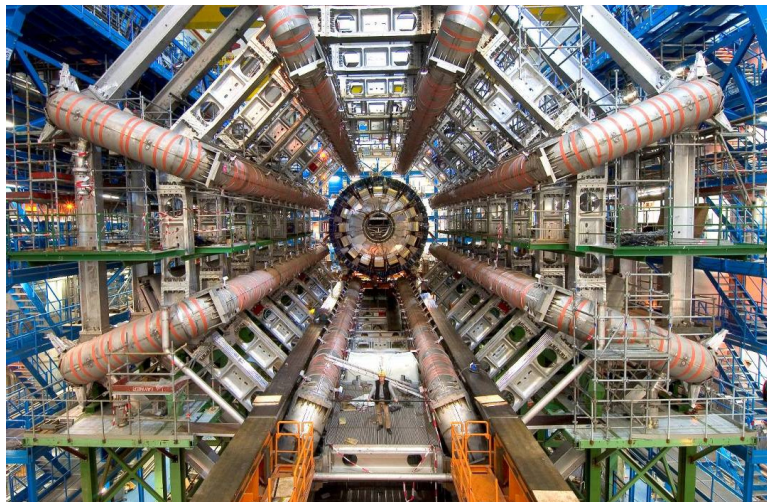


Figure 4.6: A photograph of the barrel toroid during ATLAS installation. 8 coils enclosed in independent cryostats make up the barrel toroid, providing a field orthogonal to the muon momentum. A person can be seen in the centre to show the huge scale of the muon system.

(RPCs) and Thin Gap Chambers (TGCs) provide the muon trigger, identify the bunch-crossing signals belong to, and provide a measurement of the third component of position, (ϕ). Each type of chamber is arranged into three concentric cylindrical shells in the barrel region or circular plates in the end-cap, as shown in Figure 4.5.

As with the inner detector, numerous precision hits are required for the track reconstruction and accurate momentum measurement. MDTs provide these measurements over most of the η range of ATLAS. An MDT consists of a chamber filled with straw tubes. Each tube consists of a 30mm diameter cylindrical cathode with a 50 μm anode wire filled with Ar/CO₂ gas. As the electron drift time is known, a precision position measurement can be made with a resolution of 80 μm . A chamber consists of 3 - 8 layers of drift tubes with a combined precision of around 35 μm per chamber.

At high η the greater track multiplicity demands higher granularity detectors. Hence in the range $2 < |\eta| < 2.7$ CSCs are used which consist of multi-wire proportional chambers. These provide a precision of 40 μm in the bending plane. The cathode strips are orthogonal to the anode wires providing a position measurement in the ϕ direction with 5 mm precision.

The barrel trigger chambers, RPCs, are simple gas filled, parallel plate chambers. The end-cap trigger chambers, TGCs are multi-wire proportional chambers. The muon trigger covers the range $|\eta| < 2.4$. The muon trigger looks for coincidences of hits between inner and outer layers. The wider the region in the outer layers included in the coincidence measurement, the lower the p_T threshold it corresponds to.

4.2.5 Trigger and Data Acquisition

The ATLAS trigger consists of three levels, shown in Figure 4.7. The first level is implemented in custom-built hardware and must reduce the 40 MHz event rate down to 75 kHz (a limit imposed by the maximum detector readout rate). Level-1 must make a decision every 25 ns whether to reject the event or pass it on to the next level. In practice this is difficult, not least because signals travelling at the speed of light cannot reach the trigger electronics in such a short time scale. The solution is memory buffers on the detector. Data are stored in on-detector memory which awaits the Level-1 accept (L1A). A maximum latency of $2.5 \mu\text{s}$ is allowed before the on-detector memory is full and the data for that bunch-crossing are lost. The Level-1 Trigger hardware is located off detector in a separate cavern adjacent to the cavern housing the main experiment. Approximately $1 \mu\text{s}$ are taken by transmitting the

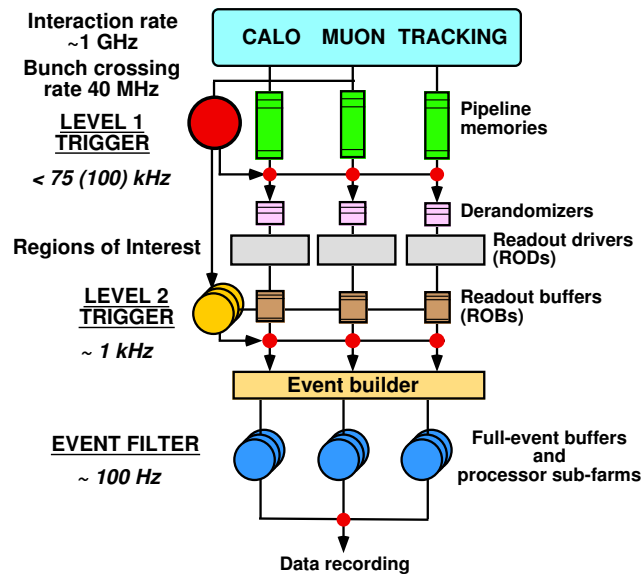


Figure 4.7: A diagram showing the 3 levels of the ATLAS Trigger and the reduction in event rate after passing each trigger level [21].

required detector information to the trigger and sending the Level-1 accept signal. The system was designed to leave $0.5 \mu\text{s}$ as a contingency. A total of $1 \mu\text{s}$ remains in which to make the decision. The data from each event are pipe-lined into custom-built hardware where relatively simple, but very fast, trigger algorithms using limited information are implemented. The main Level-1 trigger system at ATLAS is divided up into a muon trigger and calorimeter trigger. In chapter 7 the Level-1 calorimeter trigger is described in detail.

The multiplicities of candidate trigger objects are passed from each trigger to the Central Trigger Processor (CTP). The CTP compares the found trigger items to the trigger menu and sends the L1A signal to the sub-detectors. The L1A triggers the entire event information to be readout from the detector to be processed by the next trigger levels. The CTP also applies pre-scales to the Level-1 menu items. Pre-scales allow only a fraction of events meeting a certain trigger menu criteria to pass. This allows low thresholds to be used whose rates would otherwise be too high to readout.

In addition to sending multiplicities of trigger items to the CTP, Level-1 Trigger hardware also send RoIs (Regions of Interest) to the Level-2 Trigger. An RoI consists of the η - ϕ co-ordinate of a Level-1 trigger object and the thresholds that were passed. Level-2 and the Event Filter, together referred to as the High Level Trigger (HLT), are implemented in software running on large computer farms. Level-2 uses only a sub-set of the data read-out from the detector (guided by the RoIs) and reduces the rate to below 3.5 kHz with an average event processing time of 40 ms. The event filter uses the full-detector readout and performs the same event reconstruction used in

offline analysis. It reduces the rate to the order of 200 Hz (a limit imposed by bandwidth and disk space constraints) with an average processing time of 4 seconds.

Chapter 5

Search Prospects for a High Mass Higgs in the Channel

$$*H \rightarrow ZZ \rightarrow llbb*$$

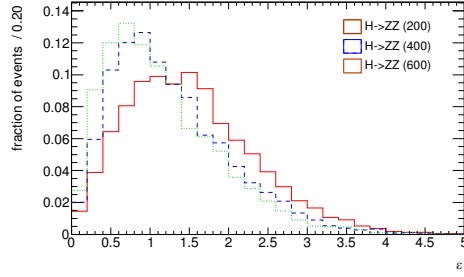
The search for the Higgs boson is one of the primary goals of the ATLAS experiment. The Standard Model predicts all of the properties of the Higgs boson except for its mass. Searches must be made over the entire mass range, from the excluded lower region, 114 GeV, up to 1 TeV. This analysis examines the search prospects for the Higgs boson in the channel $H \rightarrow llbb$ where the leptons are required to be either electrons or muons. Note that l will be used to refer to only electrons and muons and not τ -leptons or neutrinos. This channel is most sensitive at high mass, $m_H > 200$ GeV, where the Higgs can decay to two on mass shell Z bosons. It is here where the branching fraction for decay to massive vector bosons dominates. Also, as the Z bosons are on mass shell, the well defined Z invariant mass helps to distinguish this

signal from the background. In this chapter, a cut based analysis to isolate $H \rightarrow llbb$ events is presented and its performance is evaluated by examining the exclusion confidence limits that can be placed on the production cross-section.

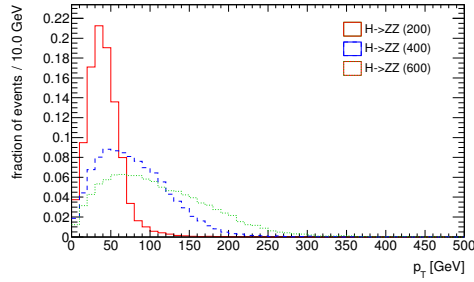
5.1 Signal Properties and Dominant Backgrounds

5.1.1 $H \rightarrow llbb$

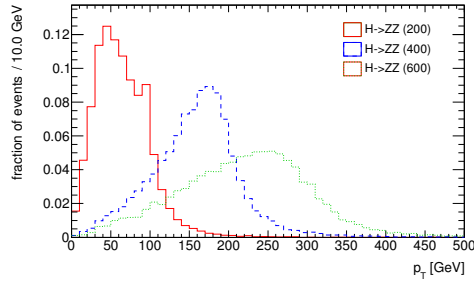
The leading order Feynman diagrams for Higgs production are shown in figure 3.2. The dominant production mechanism at the LHC is $gg \rightarrow H$ and is the focus of the analysis presented here. The vector boson fusion process also contributes with an additional pair of forward jets in the final state. This production channel is included in the simulation but no specific cuts are applied to select this final state. Figure 5.1 shows the truth level kinematic distributions from simulated events for several generated Higgs masses. The final state leptons and jets are predominantly produced in central pseudorapidity and, as expected from the decay of a high mass state, are produced with very high transverse momentum. At very high mass, the intermediate Z -bosons are highly boosted, causing their decay products to be produced close together in the lab frame. A Higgs signal will appear as a resonance in the $lljj$ invariant mass distribution. At large Higgs masses the natural width of the Higgs boson also becomes very large, making distinguishing a peak above background increasingly difficult.



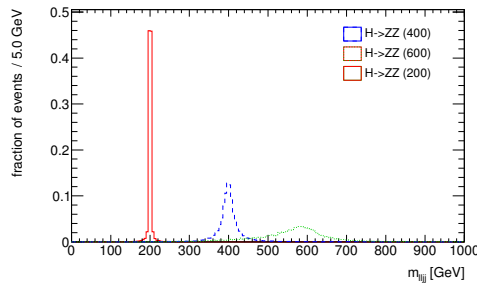
(a) Lepton maximum $|\eta|$



(b) Lepton p_T



(c) $Z p_T$



(d) m_H

Figure 5.1: Truth-level kinematic distributions for $H \rightarrow llqq$ events for several Higgs masses. (a) $|\eta|$ of the highest $|\eta|$ lepton, (b) lepton p_T distribution, (c) the intermediate Z -boson p_T and (d) the invariant mass of the Higgs boson.

The $gg \rightarrow H$ ($qq \rightarrow Hqq$) cross-section has been calculated to NNLO (NLO) precision. The production cross-section multiplied by the $H \rightarrow llqq$ branching-fraction is strongly mass dependent. It ranges from 213 fb for $m_H = 200$ GeV to 14.8 fb for $m_H = 600$ GeV. A selected list of signal and background cross-sections are shown in table 5.1. A full list of cross-sections used for this analysis is included in Appendix A. All cross-sections are for proton-proton collisions at $\sqrt{s} = 7$ TeV. It should be noted that the ultimate design energy of the LHC is $\sqrt{s} = 14$ TeV. Increasing the centre-of-mass energy increases the production cross-section for high mass states and so a significant improvement can be expected when the LHC achieves full centre-of-mass energy.

5.1.2 Z +jets

The dominant background comes from Z +jets final states. Zbb , Zbq and Zqq final states contribute. Much of this background can be rejected by requiring the reconstructed di-jet mass to be close to the Z boson mass. However, the Z boson production cross-section is many orders of magnitude greater than the signal cross-section. The NLO inclusive Z boson production cross-section is 1.07 nb. The predicted cross-section for Z boson associated with two or more partons is 82.6 pb. When two of those partons are required to be b -quarks, the predicted cross-section is 12.8 pb. By requiring the two jets to be b quarks, the Z background is reduced by a factor of 6.4 while the signal is only reduced by a factor of $BR(Z \rightarrow qq)/BR(Z \rightarrow bb) \approx 4.5$. Consequently, the best signal to background ratio is in the $llbb$ channel assuming that light

Table 5.1: A selection of relevant processes and their cross-sections. A complete set is available in Appendix A.

Process	$\sigma \times \text{BR}$ [pb]
$H(200) \rightarrow ZZ \rightarrow llqq$	0.213
$H(400) \rightarrow ZZ \rightarrow llqq$	0.0834
$H(600) \rightarrow ZZ \rightarrow llqq$	0.0148
$Z \rightarrow ll$	1070.
$ZZ \rightarrow llqq$	0.591
$WZ \rightarrow llqq$	0.817
$t\bar{t}$	165.
Process	$\sigma \times \text{BR}$ [pb]
$H(200) \rightarrow ZZ \rightarrow llbb$	0.0473
$H(400) \rightarrow ZZ \rightarrow llbb$	0.0185
$H(600) \rightarrow ZZ \rightarrow llbb$	0.0032
Zbb	12.8
$ZZ \rightarrow llbb$	0.131
$t\bar{t} \rightarrow l\nu l\nu bb$	1.46

jets can be efficiently rejected.

5.1.3 Top-quark Pair Production

The top quark almost always decays to Wb , and the W to a pair of quarks or charged-neutral lepton pair. This gives three distinct event signatures for $t\bar{t}$ events: di-leptonic ($l\nu l\nu bb$), semi-leptonic ($l\nu qqbb$) and fully-hadronic ($qqqqbb$). The di-leptonic channel has the same set of final state particles as the signal, with the exception of the unmeasured neutrinos. As well as the invariant mass of the lepton and jet pairs, these events can be distinguished from the signal due to their high E_T^{miss} . The predicted total $t\bar{t}$ cross-section is 165 pb, and the cross-section times branching fraction of a single same-flavour di-leptonic final state is 1.46 pb.

5.1.4 Di-boson Production

ZZ events have an almost identical signature to the Higgs signal events, with the exception that the decay products are not constrained to the Higgs boson invariant mass. However, the predicted production cross-section is of a similar order to the signal cross-section. The total ZZ cross-section is predicted to be 5.64 pb. The cross-section times branching fraction for $ZZ \rightarrow llqq$ and $ZZ \rightarrow llbb$ are 0.591 pb and 0.131 pb respectively. Another di-boson background, WZ , was also considered in this study. Due to the limited jet energy resolution, hadronic W decays can be reconstructed within the Z mass window.

5.1.5 QCD

There are two sources of background from QCD events. Firstly, jets of hadrons can some times produce fake electrons and prompt muons which are misidentified as isolated leptons from the primary interaction. Although it is rare for jets to fake leptons, QCD multi-jet production has a very high cross-section, and so must be considered. The multi-jet predicted production cross-section is $\mathcal{O}(1\text{mb})$ for processes with $p_T > 17$ GeV. In sections 5.2.1 and 5.2.3 the choice of lepton quality cuts is motivated from studies of simulated QCD events. However, it is difficult to generate enough Monte Carlo events to match or exceed the luminosity that will ultimately be collected. For such high cross-section processes these studies suffer from large statistical uncertainties. A data driven method for estimating the QCD background is shown in section 6.4.

Secondly, hadrons containing heavy quarks must decay weakly and so can produce leptons. This background is considered separately from the inclusive QCD background. As the production cross-section for this process is predicted to be much smaller, $\mathcal{O}(10 \text{ nb})$, simulation statistics are not as limited.

In the following analysis, two distinct QCD samples were studied: an inclusive QCD sample which is dominated by light flavoured jets; and a dedicated QCD di-jets sample with b/c -flavoured jets is also shown. These are labelled Multi-jet and $b\bar{b} + c\bar{c}$ respectively in figures 5.3 and 5.8.

5.2 Event Selection

5.2.1 Electron Reconstruction

The ATLAS reconstruction selects electrons by matching calorimeter clusters, with $E_T > 3 \text{ GeV}$, to tracks reconstructed within the inner detector, within a wide window of $\eta \times \phi = 0.05 \times 0.10$ [24]. This is a very efficient selection but has poor background rejection. Additional cuts are applied to select a clean sample. There are three standard sets of electron ID cuts used in ATLAS: “Loose”, “Medium” and “Tight”. These correspond to an increasingly stringent set of isolation cuts applied to the reconstructed electron. The tighter selections each contain the cuts from previous looser selections; it is guaranteed that all medium electrons pass the loose selection and all tight electrons pass the medium selection. The electron ID cuts are summarised in table 5.2.

Table 5.2: A summary of the Electron ID cuts. These are explained in detail in the referenced material. [24]

Electron ID	Cuts
Loose	Detector acceptance ($ \eta < 2.47$)
	Hadronic leakage veto
	Shower lateral width and shape (2nd calo. layer)
Medium	Veto two maxima in shower transverse profile (rejects $\pi^0 \rightarrow \gamma\gamma$)
	Shower width and shape (1st calo. layer)
	Track quality cuts ($N_{\text{Hits}}^{\text{SCT}}$, $N_{\text{Hits}}^{\text{pixels}}$ and impact parameter)
Tight	Track-cluster match ($\Delta\eta < 0.005$, $\Delta\phi < 0.02$)
	E/p (ratio of cluster energy to track momentum)
	TRT total hits and high threshold hits.

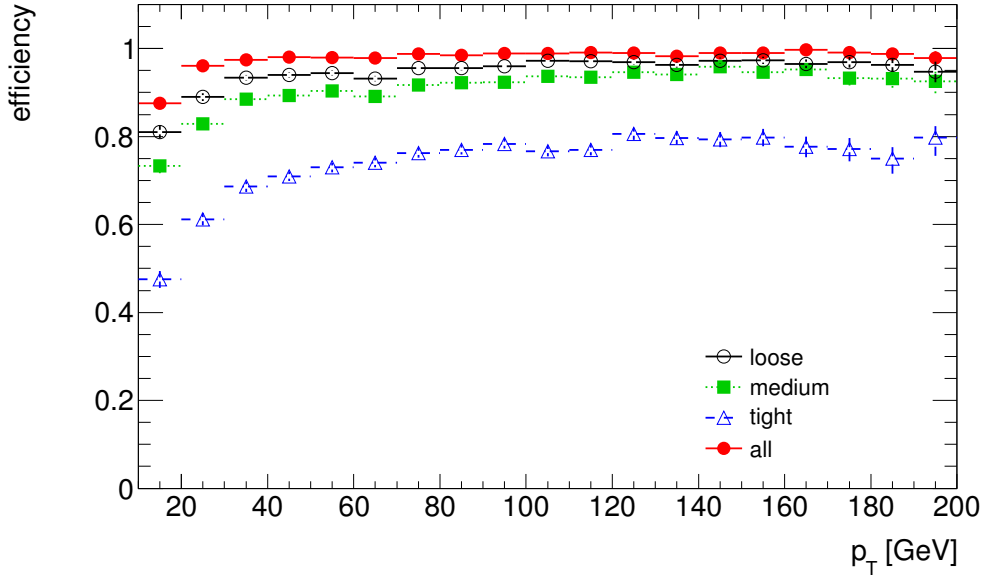


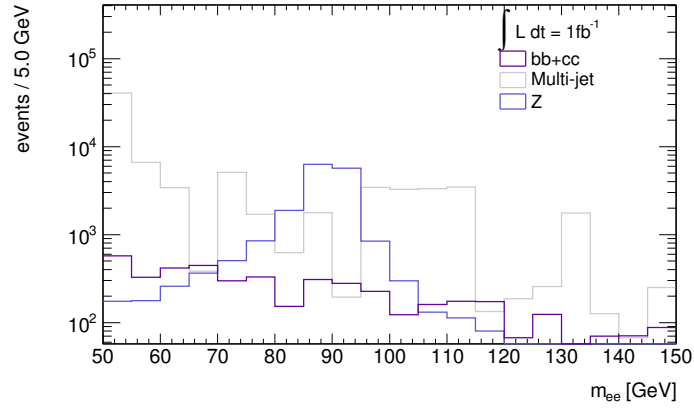
Figure 5.2: Electron reconstruction efficiency binned in electron p_T for each set of electron ID cuts.

Figure 5.2 shows the efficiency turn-on curves for each electron ID type in $H \rightarrow eeqq$ events. The reconstruction efficiencies for the Loose, Medium and Tight electrons, with $p_T > 20$ GeV and $|\eta| < 2.5$, are 95%, 91% and 74% respectively. Figure 5.3 shows the estimated background rates from simulated QCD events compared with simulated inclusive Z events. Events were required to have at least 2 electrons and at least 2 jets. The jets were selected as described in section 5.2.2. Requiring 2 Loose electrons leaves a very large QCD background, much greater than the Z background. The Medium electron ID cut provides greater rejection of QCD background while maintaining a high efficiency. In the signal region around the Z -boson mass, the QCD background is several orders of magnitude below the dominant Z background. In the following analysis only medium electrons were selected with $p_T > 20$ GeV and $|\eta| < 2.5$.

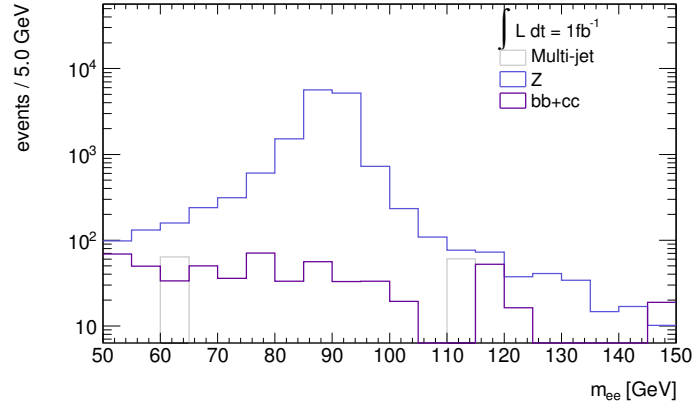
5.2.2 Jet Reconstruction and b -tagging

Jets are formed by combining calorimeter clusters with the anti- k_T algorithm [25]. All individual clusters, k , and all possible pairs of clusters, ij , are sorted by an ordering parameter, d_{ij} and d_k , which depends on the p_T of the object and the distance between the objects, ΔR , where,

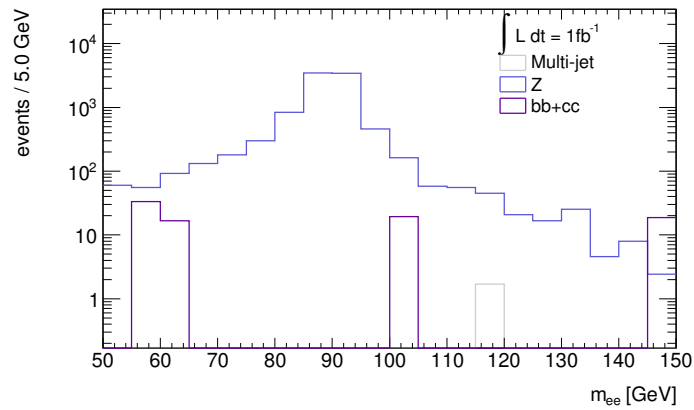
$$\begin{aligned}
 \Delta R^2 &= \Delta\eta^2 + \Delta\phi^2 \\
 d_{ij} &= \min(p_{Ti}^2, p_{Tj}^2) \frac{\Delta R_{i,j}^2}{R^2}, \\
 d_k &= p_{Tk}^2.
 \end{aligned}
 \tag{5.1}$$



(a) Loose electrons



(b) Medium electrons



(c) Tight electrons

Figure 5.3: Simulated QCD di-electron invariant mass spectrum compared to Z events. Events were required to have at least two electrons and at least two jets. (a) Loose-Loose, (b) Medium-Medium, (c) Tight-Tight.

If the minimum is a pair, ij , the objects are combined and the process is repeated. If the minimum is a single object, k , it is removed from the list and declared a jet. This process is repeated until all remaining objects have been included in a jet. As this analysis deals with jets from a boosted object, a narrow distance parameter, $R = 0.4$ was chosen.

Figure 5.4 shows the jet p_T distributions for the signal and dominant backgrounds. Jets overlapping electrons, within $\Delta R < 0.4$, were removed to prevent double counting of objects. As the signal decay products are produced centrally, and the analysis relies on precision tracking for b -tagging, only jets with $|\eta| < 2.5$ and $p_T > 20$ GeV were used in this analysis. Figure 5.5 shows the jet multiplicities for the signal and dominant backgrounds. Events were required to have at least 2 jets. An additional jet was accepted, to allow for initial and final state QCD radiation.

The decay of b -hadrons must proceed via the weak interaction which leads to experimentally observable decay lengths. This allows b -jets to be distinguished from those containing only light quarks. The default ATLAS b -tagging algorithm, SV1+IP3D, was used in this analysis [24]. This is formed from the sum of weights from the SV1 and IP3D algorithms. SV1 forms a weight based on reconstructed secondary vertices. IP3D forms a weight based on the impact parameter. Figure 5.6 shows the jet weight distributions for light and heavy jets, as well as the distribution for signal and background.

Jets with a weight, $w_{\text{SV1+IP3D}} > 3.0$ were selected as b -jets. All other jets were assumed to be light jets. This cut corresponds to a b -jet tagging efficiency of 67% in signal events ($m_H = 400$ GeV) and a light jet rejection factor of 140.

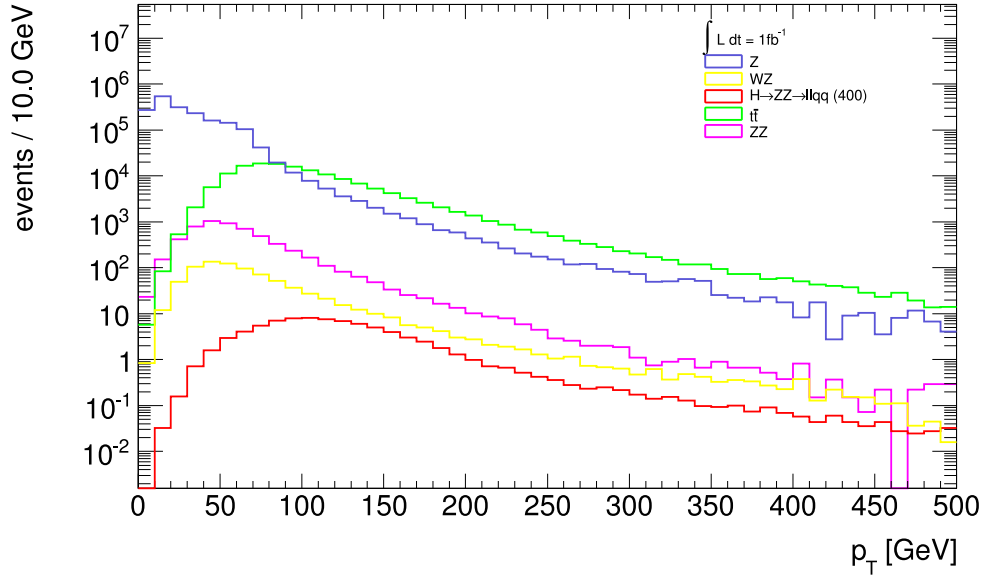


Figure 5.4: Simulated signal and background jet p_T distribution. Events were required to have at least 2 reconstructed leptons.

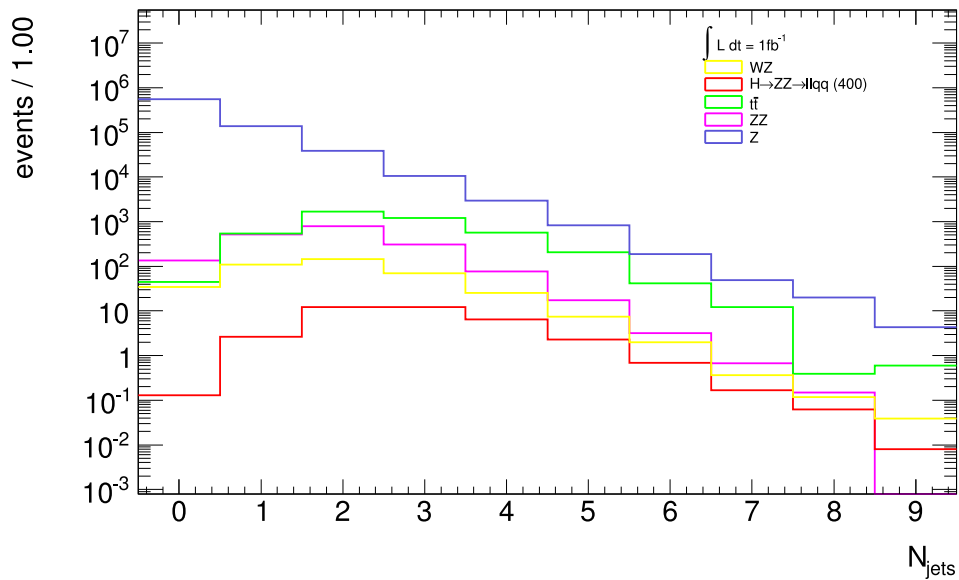
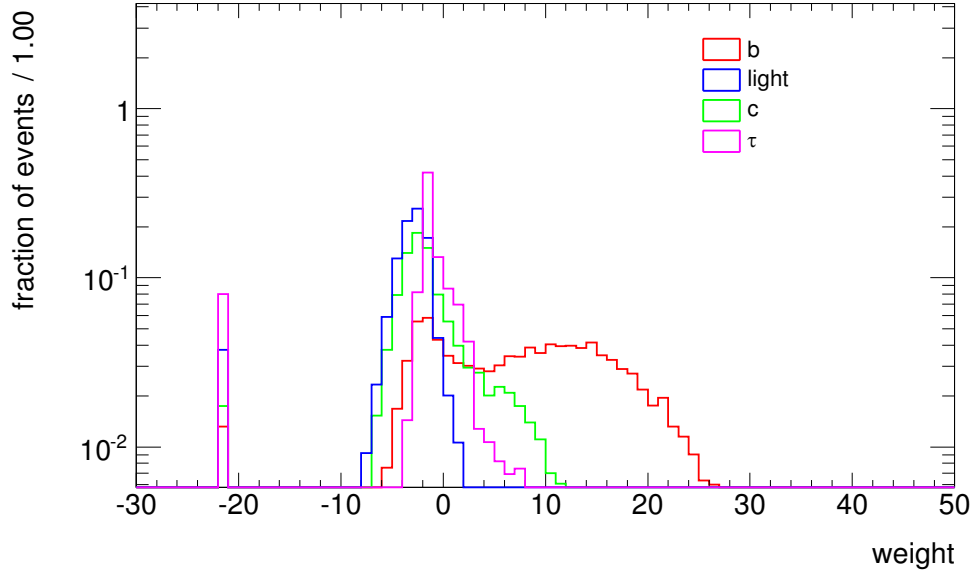
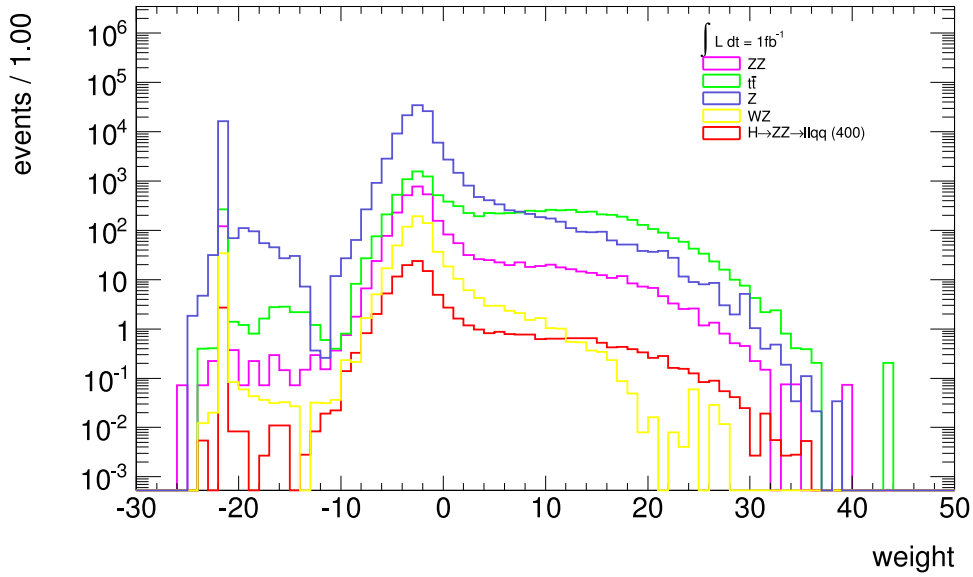


Figure 5.5: Simulated signal and background jet multiplicity distribution for $lljj$ events. Events were required to have 2 reconstructed leptons.



(a)



(b)

Figure 5.6: Simulated jet b -tag weight distributions, (a) for different jet flavours in $H \rightarrow ZZ$ ($m_H = 400$ GeV) events and (b) all signal and background samples. Events were required to have 2 reconstructed leptons and 2 reconstructed jets.

5.2.3 Muon Selection

Muons were reconstructed by combining tracks reconstructed in the muon spectrometer with those in the inner detector [24]. The momentum resolution is improved by taking the weighted mean of the reconstructed momentum vectors from each sub-detector. These are referred to as STACO (Statistically Combined) muons. Muons overlapping jets, within $\Delta R < 0.4$, were removed to reduce backgrounds from secondary muons from weakly decaying hadrons inside jets. Figure 5.7 shows the muon reconstruction efficiency. Muon reconstruction is almost 90% efficient. The 10% loss in efficiency is mostly due to detector acceptance. In this analysis, only muons with $p_T > 20$ GeV and $|\eta| < 2.5$ were selected.

Figure 5.8 shows the background from QCD in di-muon events with 2 jets. This comes predominantly from the weak decays of heavy flavours. Very few simulated QCD events pass this selection; those that do typically are reconstructed with very small invariant masses. Muons can be very efficiently and cleanly reconstructed and no additional muon ID or jet veto cuts were required.

5.2.4 Lepton and Jet Invariant mass cut

The two highest p_T leptons were selected. In the case that pairs of both electrons and muons were found, the lepton flavour with the highest p_T object was selected. Figure 5.9 shows the reconstructed di-lepton invariant mass distribution. This provides a powerful cut against $t\bar{t}$ background. The reconstructed di-lepton mass was required to lie in the range $83 < m_{ll} < 99$ GeV.

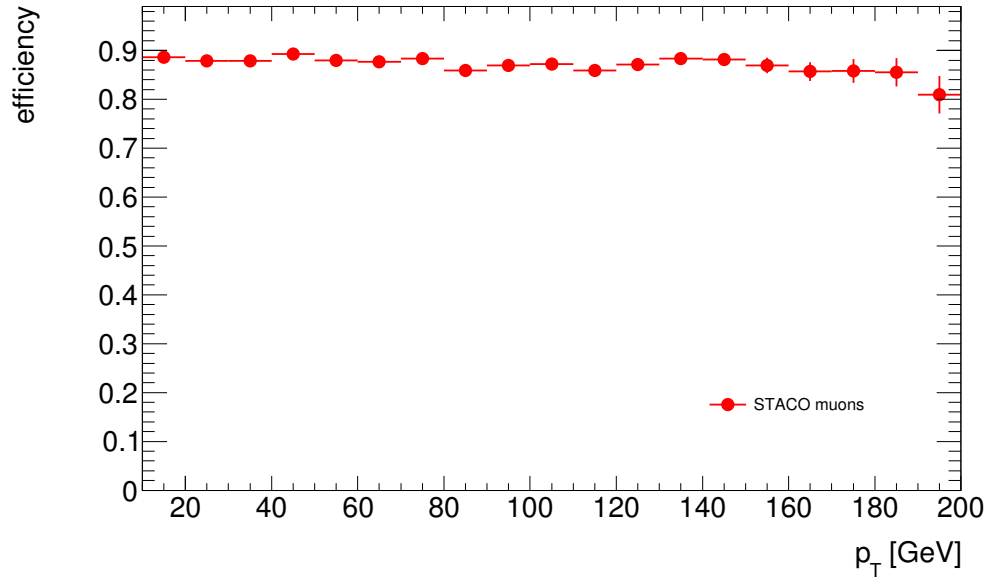


Figure 5.7: Muon reconstruction efficiency binned in muon p_T .

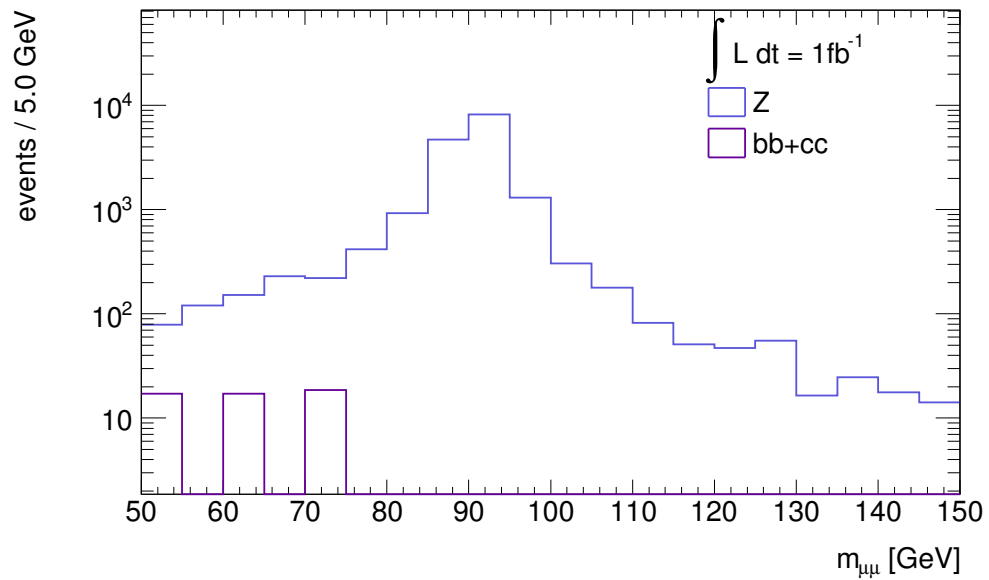
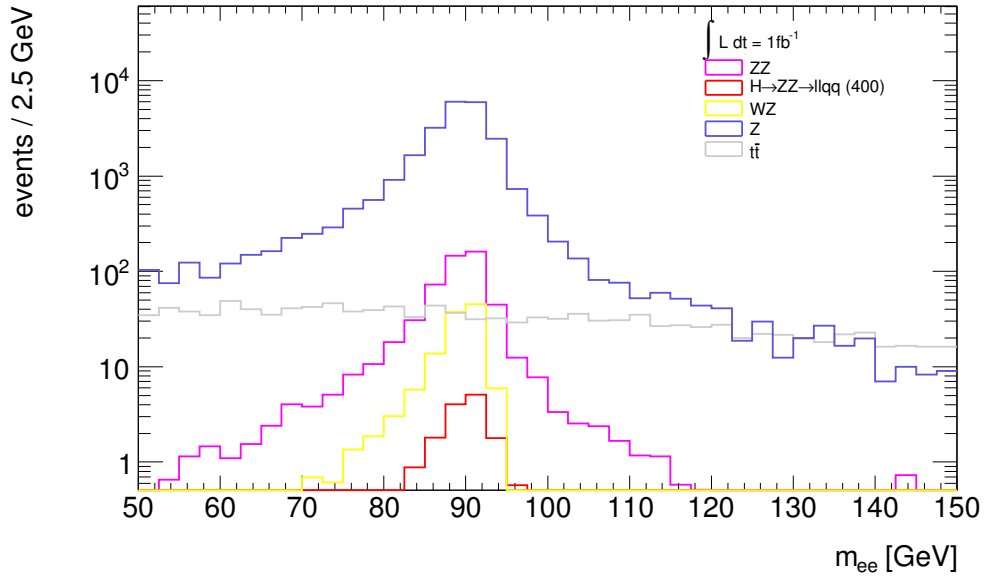
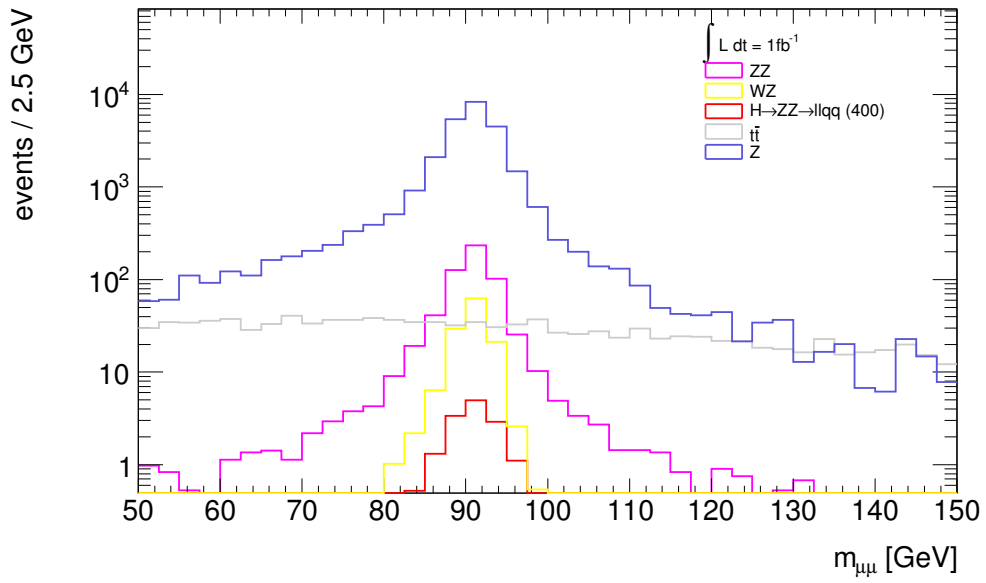


Figure 5.8: Di-muon mass distribution for Z and QCD backgrounds. Events with at least 2 muons and at least 2 jets were selected.



(a)



(b)

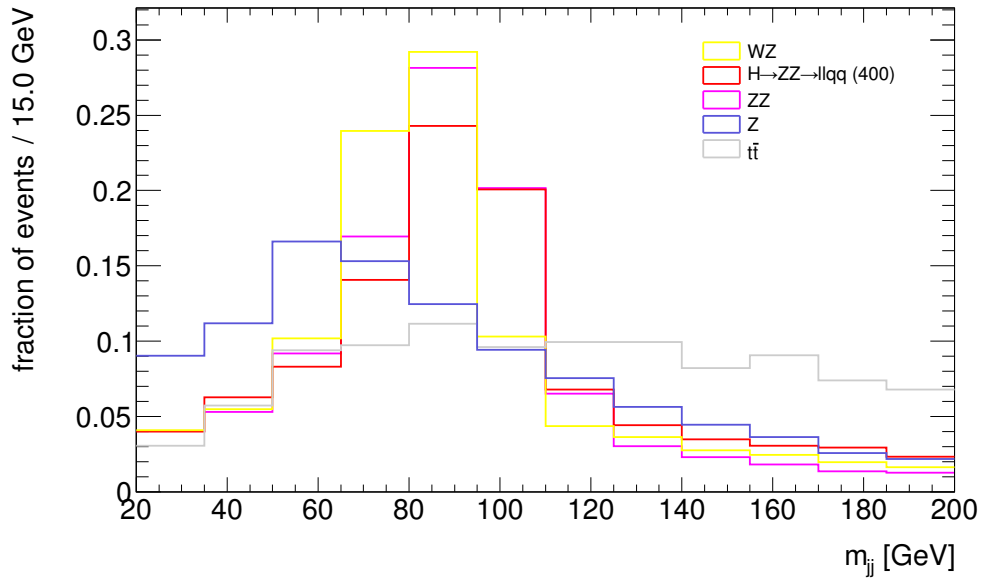
Figure 5.9: Di-lepton mass distributions for (a) $eejj$ events and (b) $\mu\mu jj$ events.

Figure 5.10 shows the di-jet invariant mass distribution, after applying the lepton mass cut. The distribution is shown both with and without b -tagging cut applied. In the un-tagged distribution, there is a continuum in the signal under the peak. This is due to additional jets in the event, and the wrong jet pair being selected. An additional benefit of selecting the lbb channel over the $llqq$ is that the correct jets are selected more often, making the di-jet invariant mass cut more efficient. The jet resolution is significantly worse than the lepton resolution, so a wider mass window was necessary. The reconstructed di-jet mass was required to lie in the range $70 < m_{jj} < 110$ GeV.

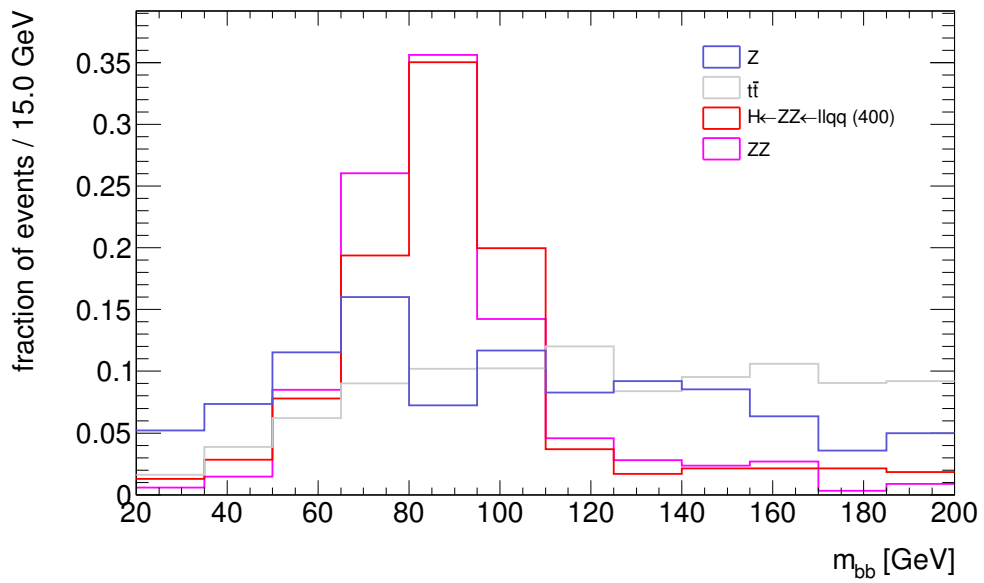
5.2.5 Jet Angular Correlation

For very high mass Higgs bosons, the Z -bosons are boosted causing their decay products to be correlated in ϕ , in the lab frame. Figure 5.11 shows the difference between the ϕ of the selected jets, $\Delta\phi_{jj}$. There is marked difference between the signal and ZZ background. This is due to the difference in p_T distributions between the two data samples. Figure 5.12 shows the reconstructed Z -boson p_T distribution. The ZZ background peaks at low p_T which leads to the decay products appearing back-to-back in the detector.

Only events with $|\Delta\phi_{jj}| < \pi/2$ were accepted. This cut was not applied in cases where the test Higgs mass was less than or equal to 300 GeV.



(a)



(b)

Figure 5.10: Di-jet mass distributions, after m_U cut, for (a) all events and (b) those with 2 b -tagged jets.

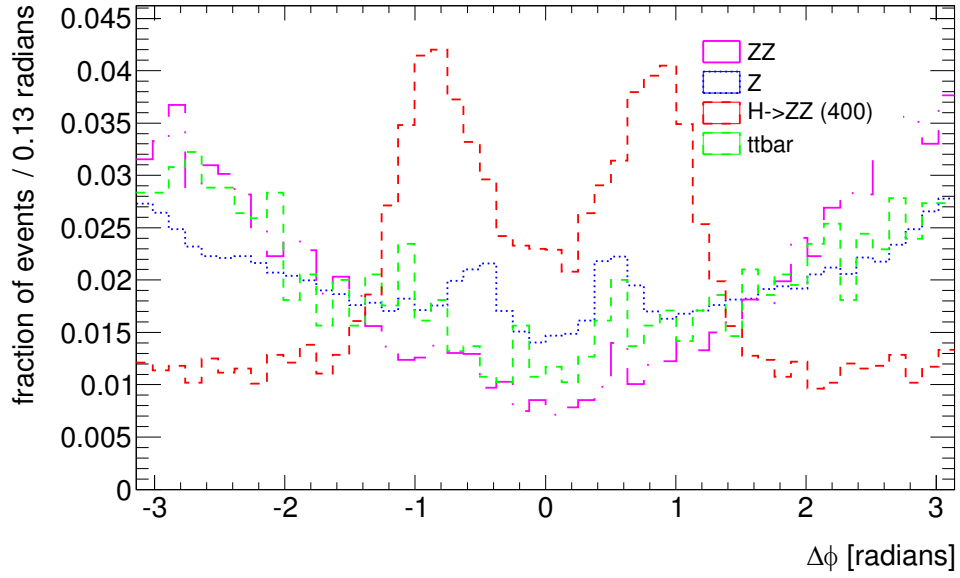


Figure 5.11: The difference in ϕ between the selected jets, $\Delta\phi_{jj}$, for signal and background events.

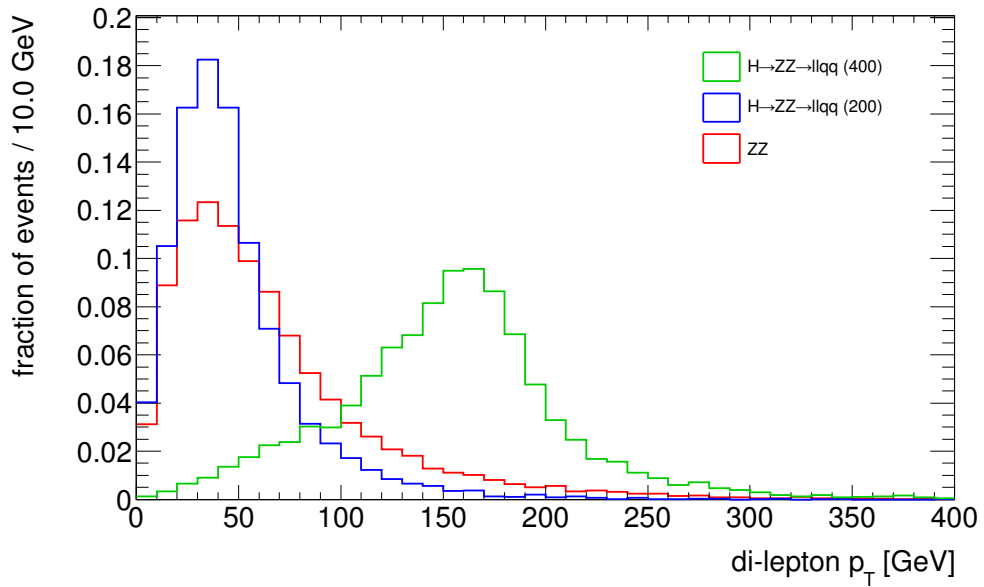


Figure 5.12: The p_T distribution of the reconstructed Z -boson from $Z \rightarrow ll$ decays in Higgs signal and di-boson events.

5.2.6 Missing E_T

The signal has no primary neutrinos in the final state and so is expected to have low E_T^{miss} . Figure 5.13 shows the E_T^{miss} distribution for signal and background. Events with $E_T^{\text{miss}} > 35$ GeV were rejected. This cut helps to reject $t\bar{t}$ events.

5.2.7 Trigger

As the signal events contain two high- p_T leptons, the trigger efficiency is expected to be very high. Table 5.3 shows the trigger efficiencies relative to the event selection for $m_H = 400$ GeV. Trigger menu items were selected to closely match the primary electron and muon triggers for the $10^{31}\text{cm}^{-2}\text{s}^{-1}$ and $10^{32}\text{cm}^{-2}\text{s}^{-1}$ trigger menus included in the simulation at the time of processing. A high trigger efficiency is achieved for both single and di-lepton triggers with the exception of the di-muon trigger. This is due to reduced geometrical acceptance of the muon trigger relative to the offline muon reconstruction. This inefficiency is compounded when requiring 2 muon triggers as both muons are required to be within the trigger acceptance. However,

Table 5.3: Trigger efficiency for signal events passing the event selection.

L [$\text{cm}^{-2}\text{s}^{-1}$]	Trigger Item	$H \rightarrow eeqq$ (%)	$H \rightarrow \mu\mu qq$ (%)
10^{31}	e10 medium	100	-
10^{32}	15 GeV loose e	100	-
10^{32}	2×5 GeV medium e	95.9	-
10^{31}	10 GeV μ	-	97.3
10^{32}	13 GeV μ	-	96.9
10^{32}	2×6 GeV μ	-	71.6

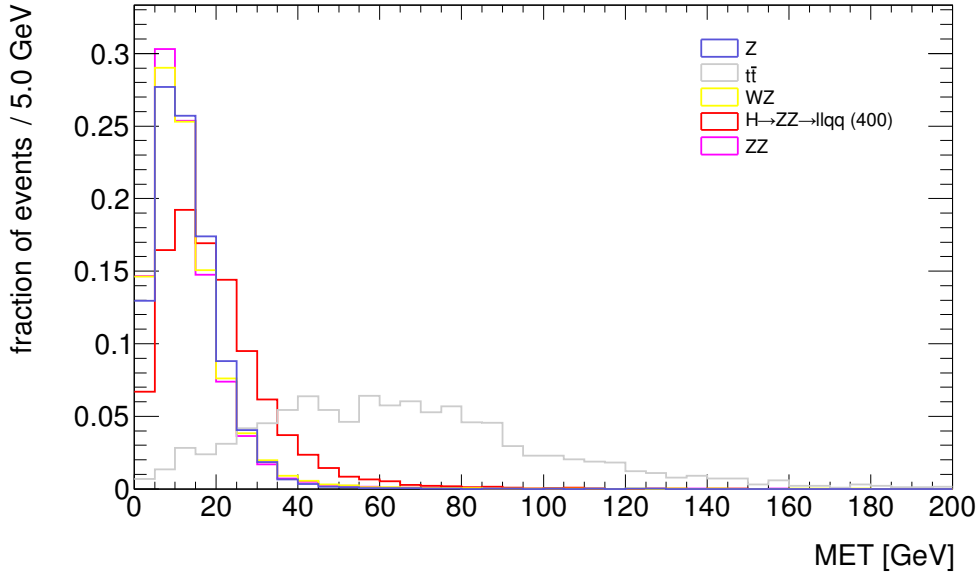


Figure 5.13: E_T^{miss} distributions for signal and background.

di-lepton triggers provide a useful backup trigger solution if the rates for single lepton triggers with p_T less than 20 GeV prove to be unsustainable in very high luminosity running.

The online trigger selection is highly variable as it must change over time to adapt to changing beam conditions, such as instantaneous luminosity or the pileup rate. However, as this study always requires two high p_T isolated leptons, it is reasonable to assume that a high trigger efficiency will be achievable over the entire lifetime of the experiment.

No trigger requirement is applied in the selection in this analysis and hence the effect of trigger inefficiencies is neglected.

5.2.8 Event Reduction

After applying the full event selection, a total of 1.3 (1.4) signal events are expected to pass the high (low) mass selection per inverse femtobarn assuming $m_H = 400$ GeV. Figure 5.14 shows how the signal efficiency varies with Higgs mass in the low and high mass selections. The total expected background is 32 (100) events per inverse femtobarn in the high (low) mass selection. The expected number of events to survive each cut are shown in table 5.4.

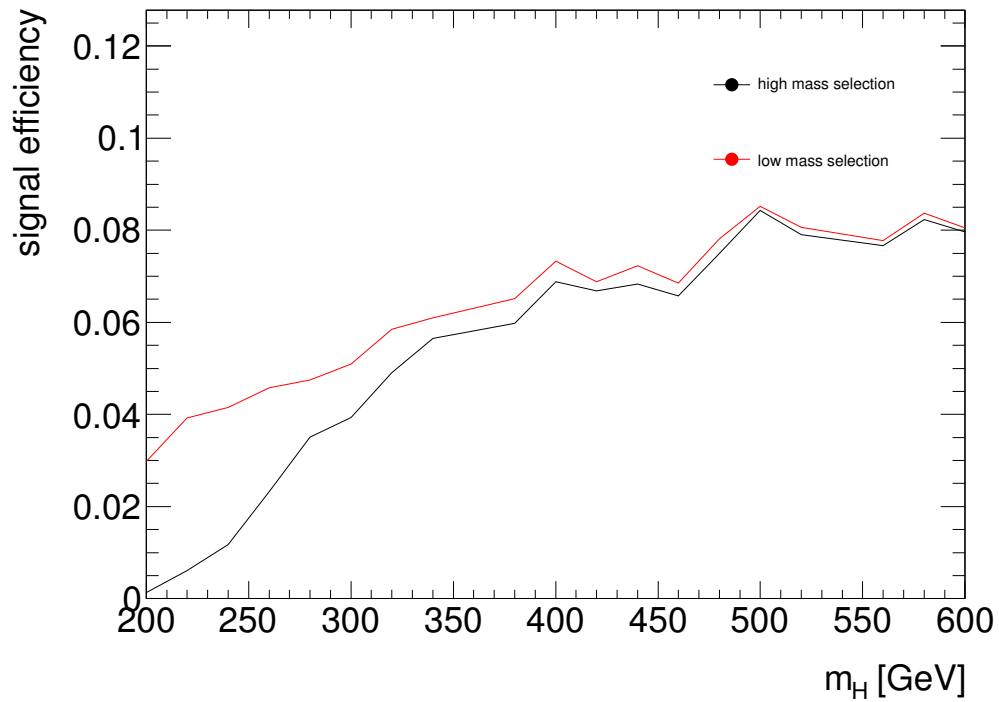


Figure 5.14: Selection efficiency for $H \rightarrow llbb$ events for each generated Higgs mass. Efficiencies are shown for both the high and low Higgs mass selection.

Table 5.4: Expected number of events passing the analysis cuts with an -integrated luminosity of 1 fb^{-1} . The signal event yields are shown for $m_H = 400 \text{ GeV}$. The signal efficiency and background rejection (defined as $1/\epsilon_{\text{background}}$) are also shown.

Cut	$H \rightarrow llqq$	WZ	ZZ	Z	$t\bar{t}$
No cuts	90.0	1100.0	12000.0	2900000.0	320000.0
$2e$ or 2μ	43.0	550.0	3900.0	1100000.0	11000.0
$83 \text{ GeV} < m_{ll} < 99 \text{ GeV}$	37.0	520.0	3300.0	910000.0	1300.0
$E_T^{\text{miss}} < 35 \text{ GeV}$	32.0	510.0	3300.0	910000.0	250.0
$2 \leq N_j \leq 3$	22.0	280.0	1900.0	47000.0	170.0
IP3D+SV1 $j_1 > 3, j_2 > 3$	2.2	0.4	95.0	140.0	53.0
$70 \text{ GeV} < m_{jj} < 110 \text{ GeV}$	1.4	0.2	67.0	27.0	5.7
$\Delta\phi_{jj} < \pi/2$	1.3	0.1	20.0	9.9	1.6
Signal Efficiency (low mass selection)	7.3%	-	-	-	-
Signal Efficiency (high mass selection)	6.8%	-	-	-	-
Background Rejection (low mass selection)	-	5.5×10^3	1.8×10^2	1.1×10^5	5.6×10^4
Background Rejection (high mass selection)	-	1.1×10^4	6.0×10^2	2.9×10^5	2.0×10^5

5.3 Kinematic Fitting

A search for a high mass Higgs boson in the channel $H \rightarrow llbb$, as compared to $H \rightarrow llll$, suffers from two main problems. As discussed previously, the $llbb$ sample suffers from larger backgrounds because, at a hadron collider, leptons naturally provide a cleaner event sample. Secondly, the use of jets leads to a lower mass resolution; it is inherently more difficult to measure the energy of jets than leptons. Kinematic fitting to the Z -boson mass can be used to significantly improve the Higgs mass resolution of the experiment. By improving the experimental resolution, the Higgs resonance will appear sharper, and hence stand out more easily against background. Also, in the case of a discovery this will provide a better measurement of the Higgs mass, which is a fundamental parameter of the Standard Model.

Figure 5.15 shows the reconstructed Higgs mass peaks for several generated Higgs masses. A Breit-Wigner distribution, to model the particle's decay width, convoluted with a Gaussian distribution, to model the detector resolution, was fitted to each signal mass distribution. The width parameter, Γ , of the Breit-Wigner component was fixed to the theoretical value while the width of the Gaussian, σ and mean μ , were left free. The results of the fit are shown in figure 5.16. At large mass the resolution is dominated by the width of the Higgs boson. In the region 200 to 400 GeV, the experimental resolution is either greater than or comparable to the particle width. In this region significant improvements can be made with kinematic fitting. Also, the reconstructed mass is systematically lower than the generated mass when using uncorrected jets.

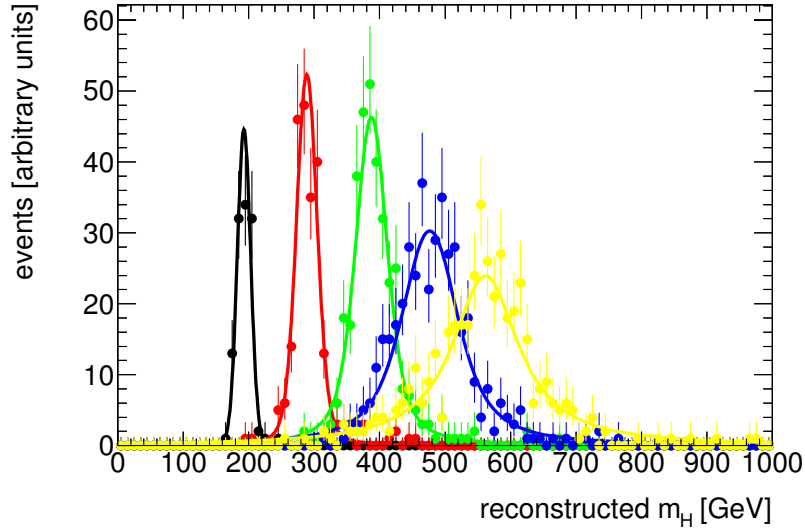


Figure 5.15: The reconstructed mass for five Higgs samples generated at mass points 200 to 600 GeV with intervals of 100 GeV. The data are fitted with the convolution of a Breit Wigner distribution with a Gaussian distribution. The fit width parameters are shown in figure 5.16.

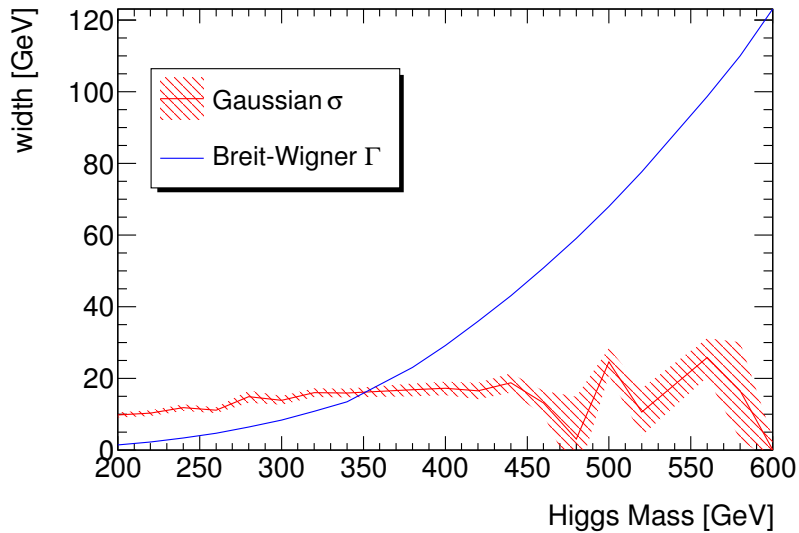


Figure 5.16: Contribution of the decay width, Γ , and experimental resolution, σ , to the overall width of the Higgs invariant mass distributions shown in figure 5.15.

5.3.1 Fitting Procedure

The method of maximum likelihood was used. Likelihood fitting provides a natural framework with which to implement kinematic constraints by adding additional terms to the likelihood function. For an event with two jets with true energies E_1^T and E_2^T , the probability density function, p , for reconstructing the jets with energies E_1^R and E_2^R is assumed to be Gaussian,

$$p(E_1^R, E_2^R; E_1^T, E_2^T, \sigma_1, \sigma_2) \propto \exp\left(\frac{-(E_1^R - E_1^T)^2}{2\sigma_1^2}\right) \times \exp\left(\frac{-(E_2^R - E_2^T)^2}{2\sigma_2^2}\right), \quad (5.2)$$

where σ_1 and σ_2 are the uncertainties on the measured jet energies.

This choice of PDF implicitly assumes that the errors on reconstructed jet energies are uncorrelated. Figure 5.17 shows the deviation of reconstructed jet energies from the truth values for simulated $H \rightarrow llbb$ events. No strong correlation was observed suggesting that the assumption that E_1^R and E_2^R are independent is reasonable.

The log-likelihood function to be minimised, $-\ln L(E_1^T, E_2^T)$, contains the following terms,

$$-\ln L(E_1^T, E_2^T)_{\text{Gaussian}} = \left(\frac{E_1^R - E_1^T}{\sqrt{2}\sigma_1}\right)^2 + \left(\frac{E_2^R - E_2^T}{\sqrt{2}\sigma_2}\right)^2 + \text{normalisation terms}. \quad (5.3)$$

The log-likelihood function was minimised with MINUIT using the MIGRAD algorithm [26]. In this case the likelihood function is trivially maximised with $E_1^R = E_1^T$ and $E_2^R = E_2^T$. In section 5.3.3 additional terms are added rep-

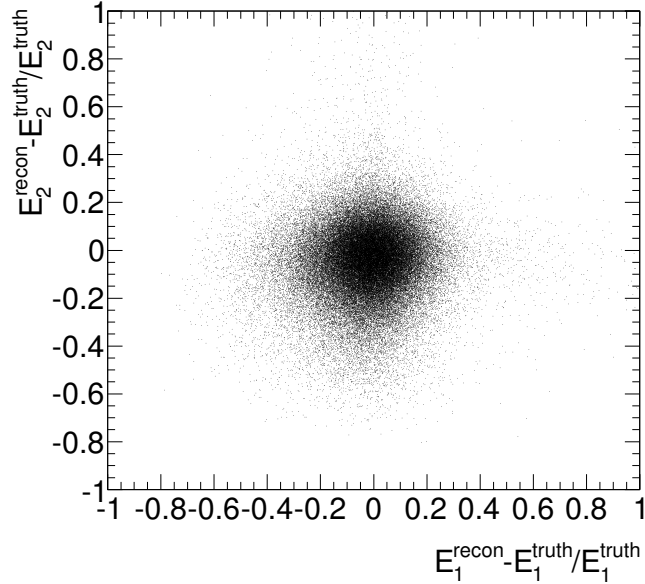


Figure 5.17: The relative error on the leading jet energy versus the second leading jet energy for $H \rightarrow llbb$ events. No strong correlation was observed.

representing the kinematic constraints which allow the likelihood function to provide useful information.

5.3.2 Jet Energy Resolution

For the kinematic fit to work effectively, the jet energy uncertainties must be accurately described. Firstly, scale corrections must be applied to ensure that the mean jet energy coincides with the true jet energy. Secondly, the widths of the Gaussian PDFs must be accurately described to allow the fit to vary the jet energies in the right range. The signal Monte Carlo jets were histogrammed into equal sized 10 GeV bins from 0 to 500 GeV of truth energy. The distribution was further divided into jets in the barrel ($|\eta| < 1.45$) and those in the end cap ($|\eta| > 1.5$). A Gaussian was fitted to

the reconstructed minus truth distribution in each bin. An asymmetric fit range was used because the low energy tail was found not to be well described by a Gaussian distribution. Figure 5.18 shows an example of one such fit in the barrel and the end-cap.

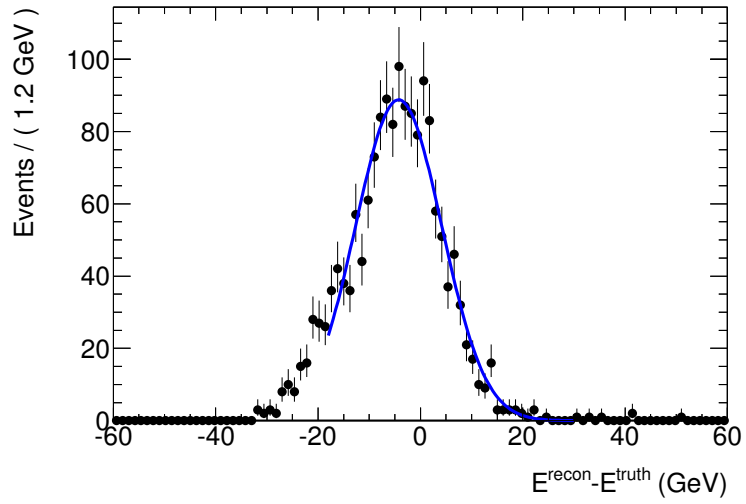
The extracted means are shown in figure 5.19 (5.20) for the barrel (end-cap). The extracted variances are shown in figure 5.21. The jets were corrected using the scale parameter directly from the fit in the appropriate bin. The correction varied from 5% (15%) to 1% (8%) in the barrel (endcap). After the correction is applied, there remains a small systematic shift (1–2%) in the fit means due to the excess in the low energy tail. As the overall jet energy uncertainty is typically much greater than 1% this systematic shift in the means can be neglected.

For the Gaussian parameter, a second order polynomial was fitted to the variance versus energy distribution. This parametrisation was used to calculate the jet energy resolution parameter input to the kinematic fit on a jet by jet basis.

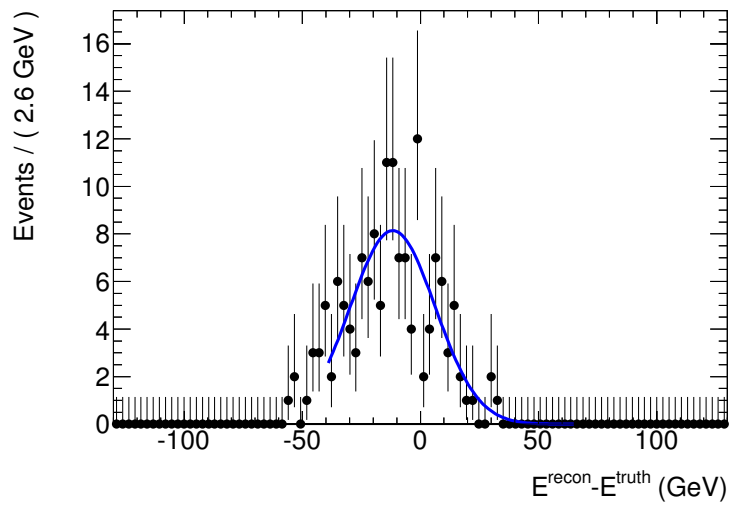
5.3.3 Kinematic Constraints

For signal events, the di-jet invariant mass should be consistent with the Z resonance. This is enforced in the fit by multiplying the probability density function by a Breit-Wigner term,

$$p(m_Z^T) \propto \frac{1}{(m_Z^T - m_Z)^2 + \Gamma^2/4}, \quad (5.4)$$

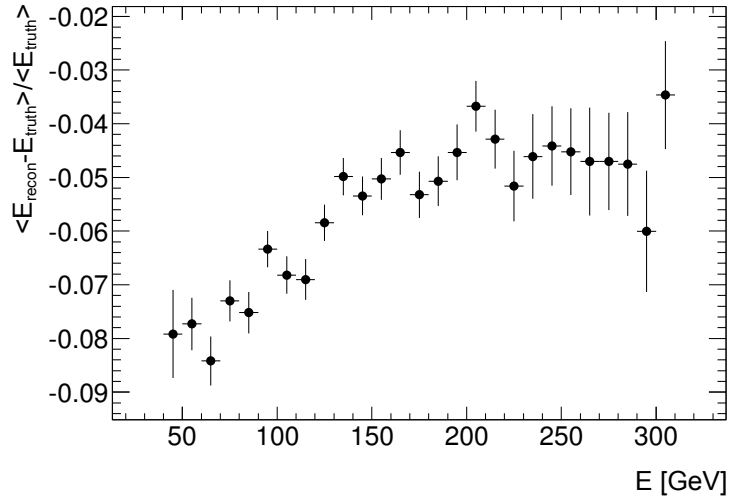


(a) Barrel

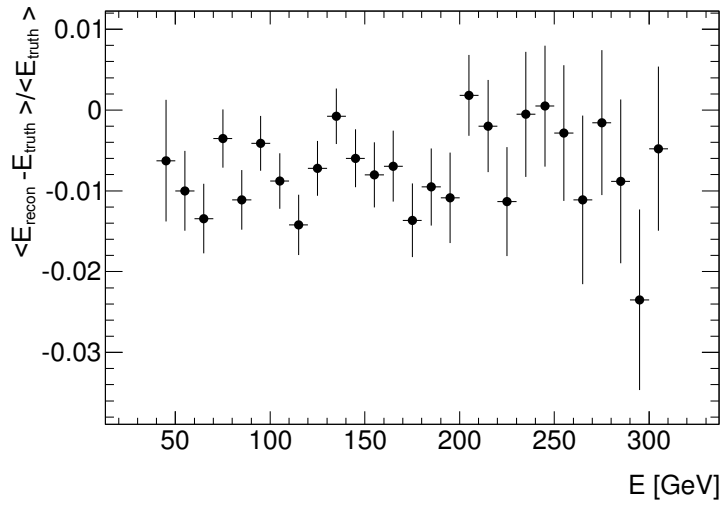


(b) End-cap

Figure 5.18: An example jet energy statistical error distribution in one energy bin slice in (a) the end-cap and (b) the end-cap.

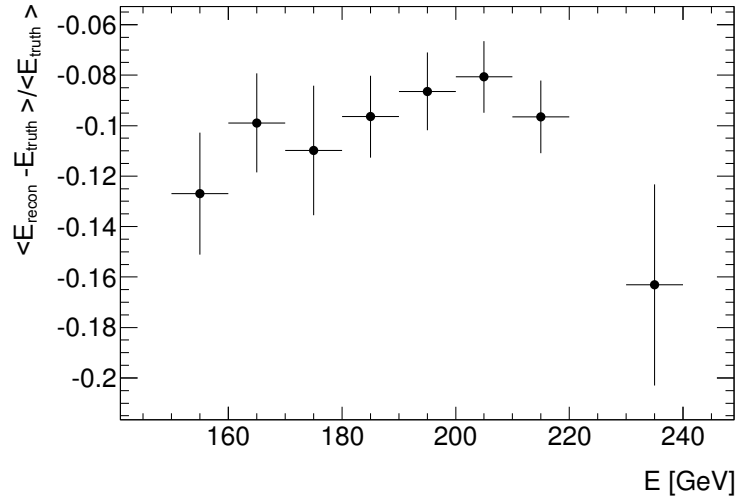


(a) Before correction

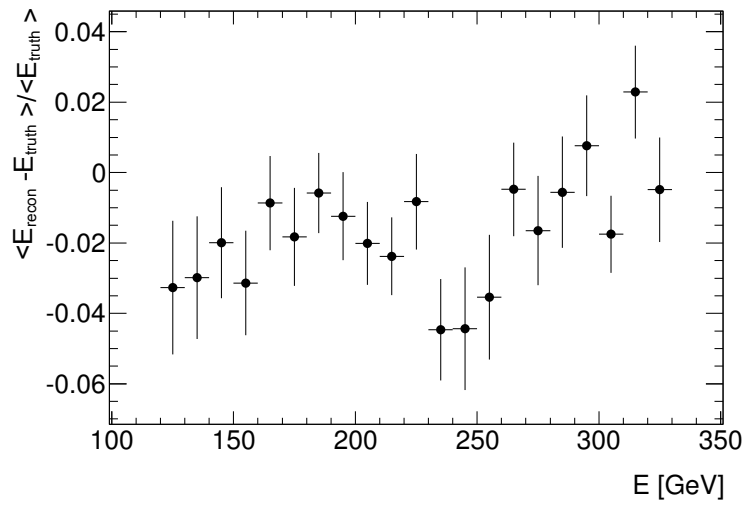


(b) After correction

Figure 5.19: Barrel jet energy fractional deviation from the truth energy ($\langle E_{recon} - E_{truth} \rangle / \langle E_{truth} \rangle$) as a function of true jet energy, shown (a) before and (b) after the correction is applied. After the correction the mean deviations are reduced to $O(1\%)$.

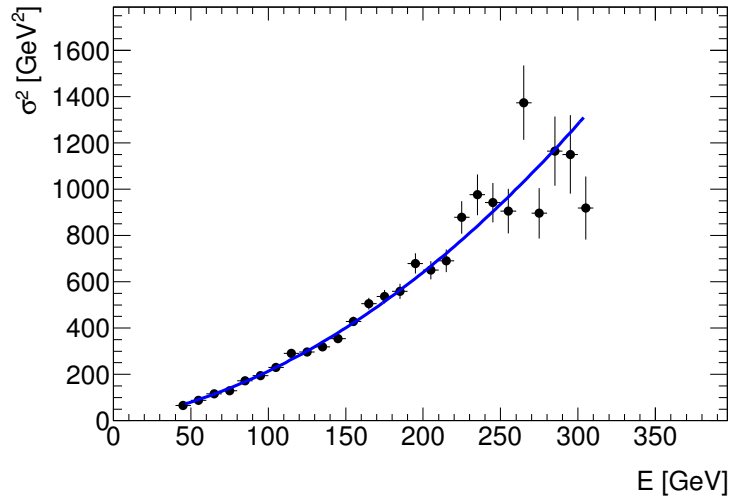


(a) Before correction

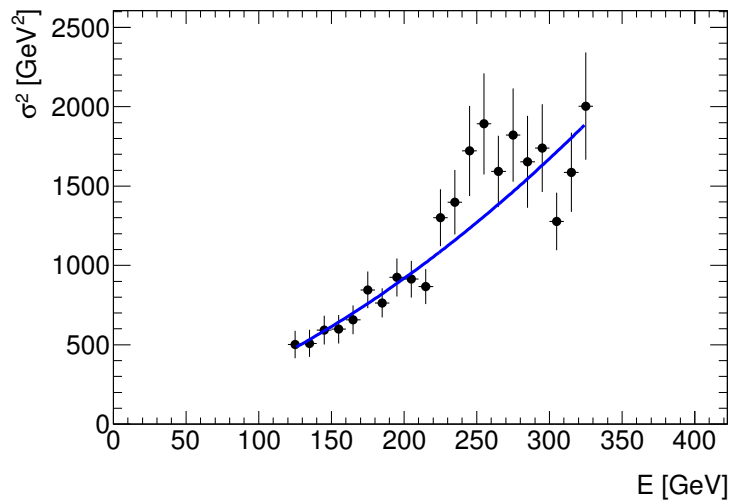


(b) After correction

Figure 5.20: End-cap jet energy fractional deviation from the truth energy ($\langle E_{recon} - E_{truth} \rangle / \langle E_{truth} \rangle$) as a function of true jet energy, shown (a) before and (b) after the correction is applied. After the correction the mean deviations are reduced to $O(2\%)$.



(a) Barrel



(b) End-cap

Figure 5.21: Jet energy variance as a function of true jet energy for jets in (a) the barrel and (b) the end-cap.

Therefore the log-likelihood function will contain a corresponding term of the form,

$$-\ln L(E_1^T, E_2^T)_{\text{BW}} = \ln |(m_Z^T(E_1^T, E_2^T) - m_Z)^2 + \Gamma^2/4| \quad (5.5)$$

where m_Z and Γ are fixed to the PDG central values of the Z boson mass (91.2 GeV) and decay width (2.50 GeV) [20]. m_Z^T , was calculated as,

$$m_Z^T(E_1^T, E_2^T) = \sqrt{2E_1^T E_2^T (1 - \cos \theta)}, \quad (5.6)$$

where the approximation that the jet mass is zero was used. θ is the reconstructed opening angle between the jets. This was not allowed to vary in the fit. Hence, the fit only corrects the overall energy and not the direction of the jets.

The combined log-likelihood function to be minimised is,

$$-\ln L(E_1^T, E_2^T) = -\ln L(E_1^T, E_2^T)_{\text{Gaussian}} - \ln L(E_1^T, E_2^T)_{\text{BW}} \quad (5.7)$$

There are two free parameters in the fit, therefore this constraint alone does not provide a unique solution. Instead, the constraint corresponds to a band of most probable values in (E_1^T, E_2^T) space, as shown for an example event in figure 5.22. For the same event, the resolution PDF described by equation 5.2 is shown in figure 5.23. The combined likelihood function is shown in figure 5.24. For this example event, the best fit point lies much closer to the true value than the initial measurement.

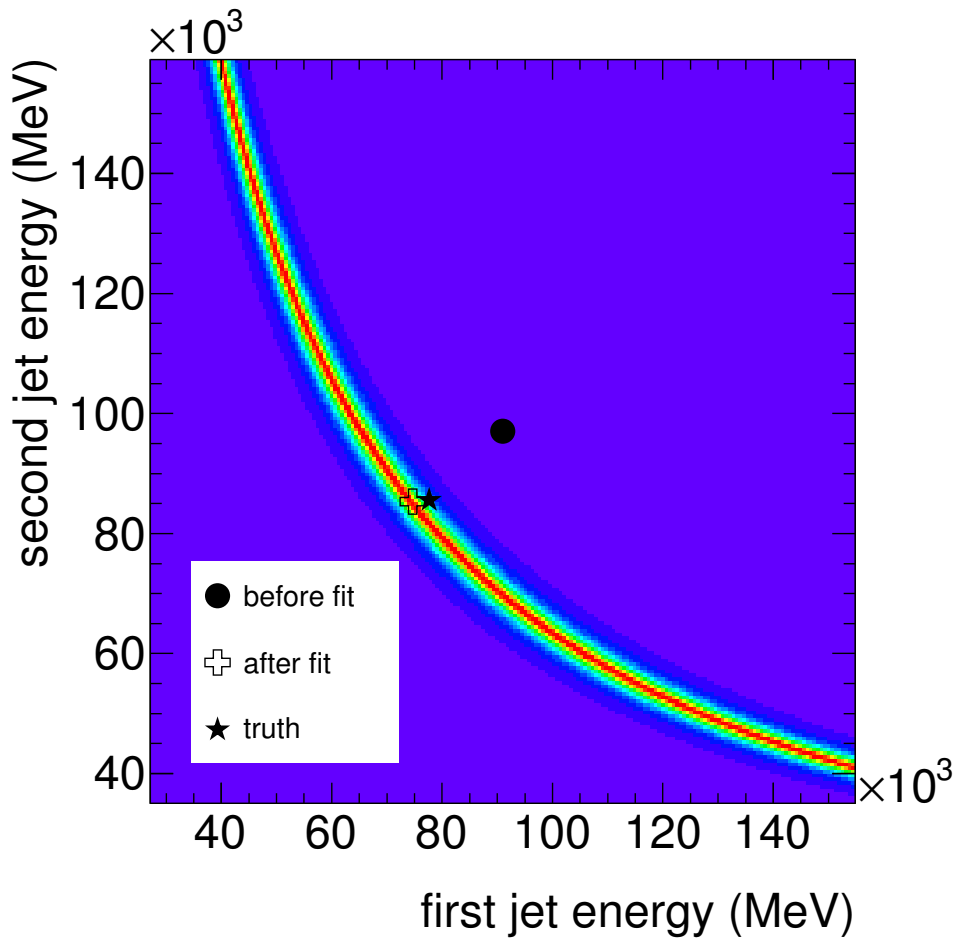


Figure 5.22: The component of the likelihood from the Z-mass constraint shown as a function of E_1^T and E_2^T for an example event. This is a visual representation of equation 5.5 for this particular event. Red values correspond to areas of high likelihood and blue values correspond to areas of low likelihood. The markers show the values before and after the fit, as well as the true value.

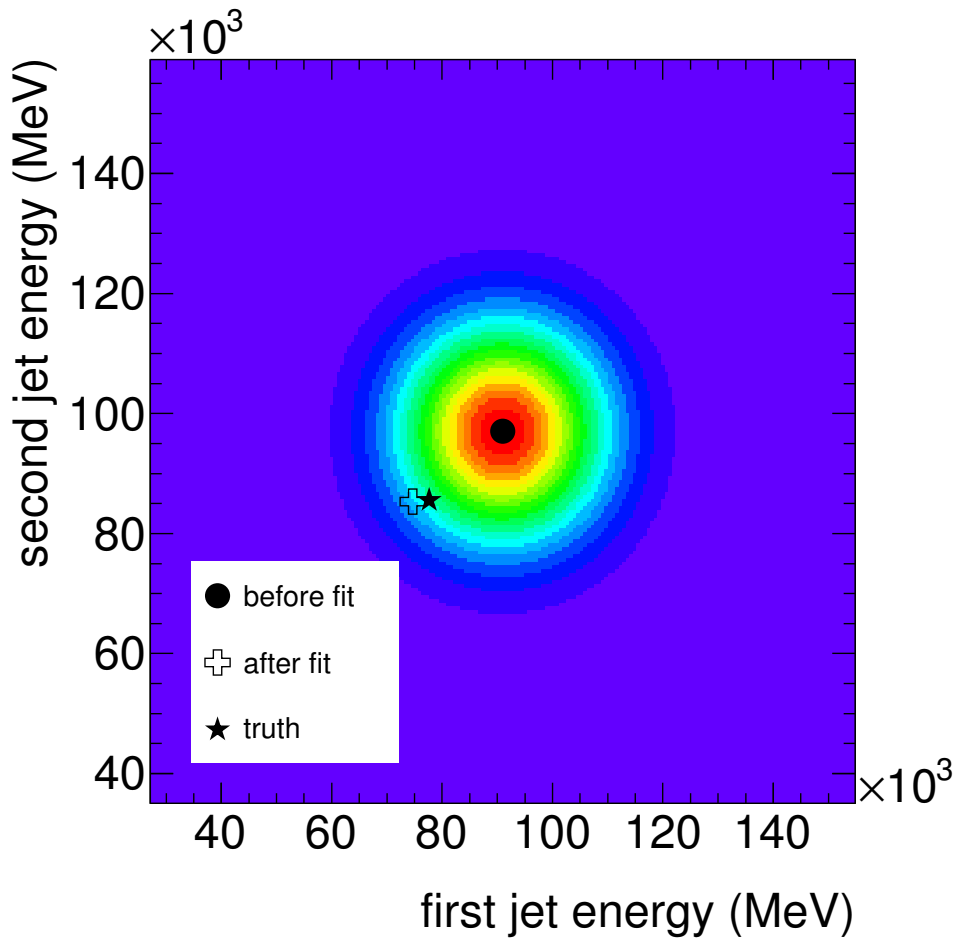


Figure 5.23: The component of the likelihood from the jet energy resolution constraint shown as a function of E_1^T and E_2^T for an example event. This is a visual representation of equation 5.3 for this particular event. Red values correspond to areas of high likelihood and blue values correspond to areas of low likelihood. The markers show the values before and after the fit, as well as the true value.

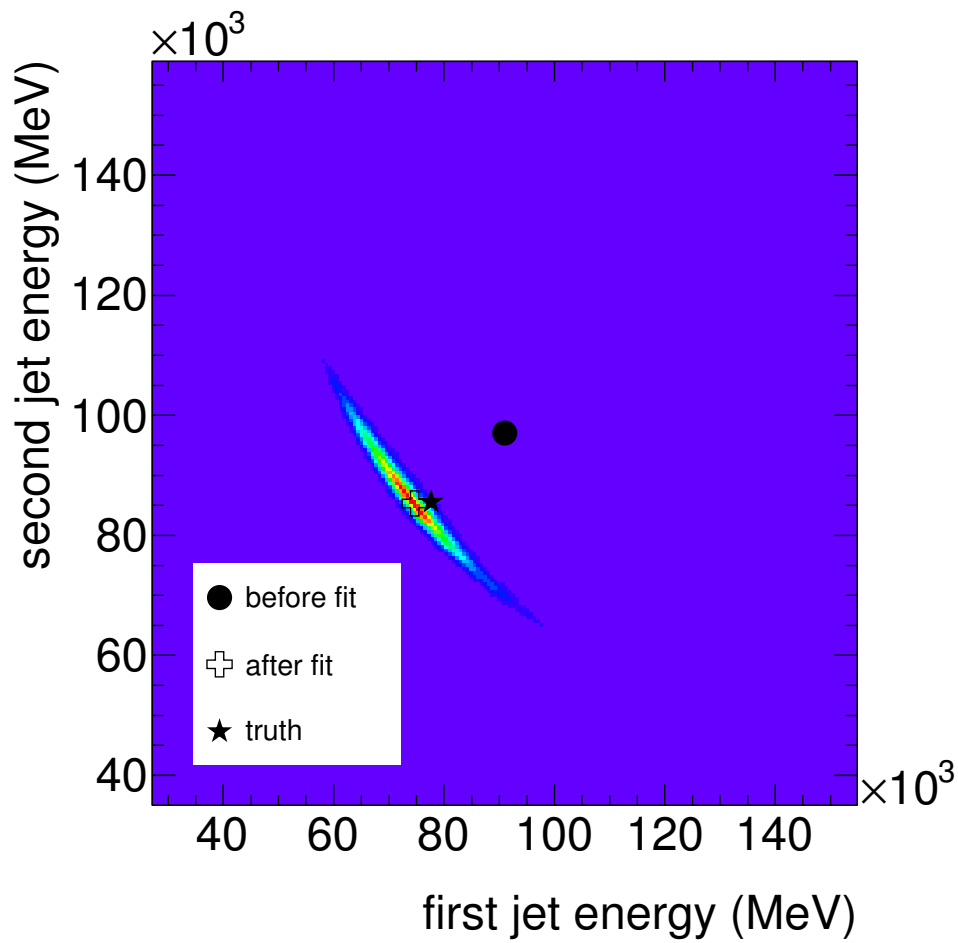


Figure 5.24: The combined likelihood surface shown as a function of E_1^T and E_2^T for an example event. This takes into account the terms in equations 5.3 and 5.5.

5.3.4 Performance of Kinematic Fit

The effect of the fit on the reconstructed $llbb$ mass distribution for signal events is shown in figure 5.25. At low mass, where the detector resolution dominates the width, there is a significant narrowing of the peak compared to figure 5.16. The widths extracted from a Breit-Wigner convoluted with a Gaussian fit are shown in figure 5.26. At $m_H = 200$ GeV, the resolution is improved by around 40% compared to the widths shown in figure 5.16. Furthermore, the mass value where the experimental resolution becomes less than the natural width of the Higgs boson has been lowered from around 350 GeV to 300 GeV. Finally, the kinematic fit improved the linearity between the reconstructed Higgs mass and the truth mass, as shown in figure 5.27.

The final reconstructed invariant mass distributions including backgrounds are shown in figure 5.28. Due to low Monte Carlo statistics, the shape determination was improved by taking the shape of the Z +jets and $t\bar{t}$ distributions from selection with no b -weight cut applied and normalizing it to the number of events passing the full selection.

5.4 Background Control Regions

It is desirable to have a data driven method to study the background contamination. This provides a useful cross-check of the simulated results and also these control samples can be used to constrain the background event rate expected in the signal region.

A control sample to isolate Z +jet events was defined by applying all

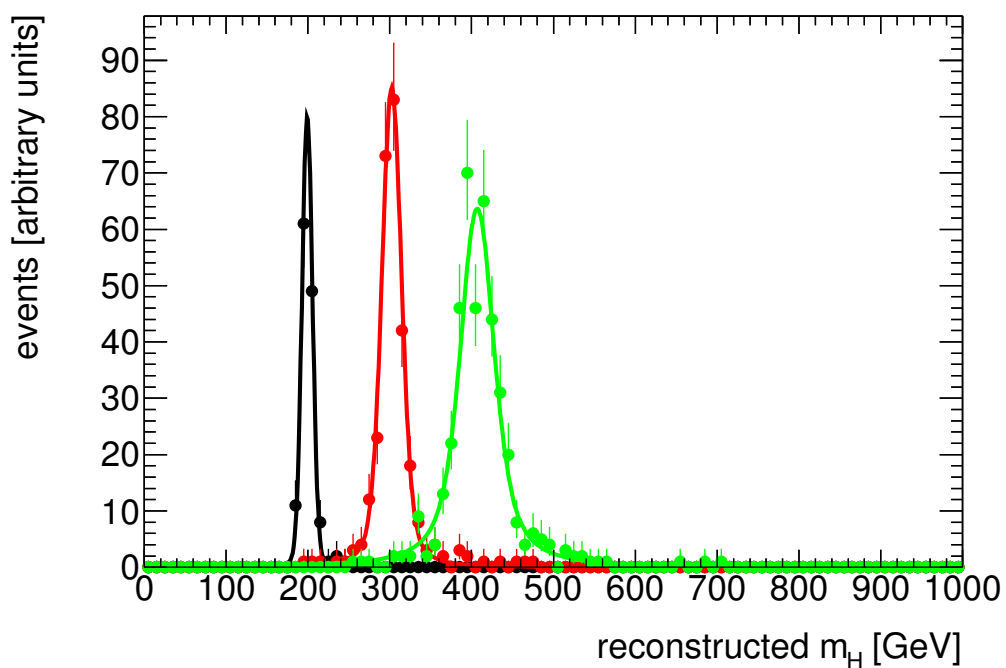


Figure 5.25: The reconstructed mass distribution, after the kinematic fit has been applied, for three Higgs samples generated at mass points: 200 GeV, 300 GeV and 400 GeV. The data are fitted with the convolution of a Breit Wigner distribution with a Gaussian distribution. The fit width parameters are shown in figure 5.26.

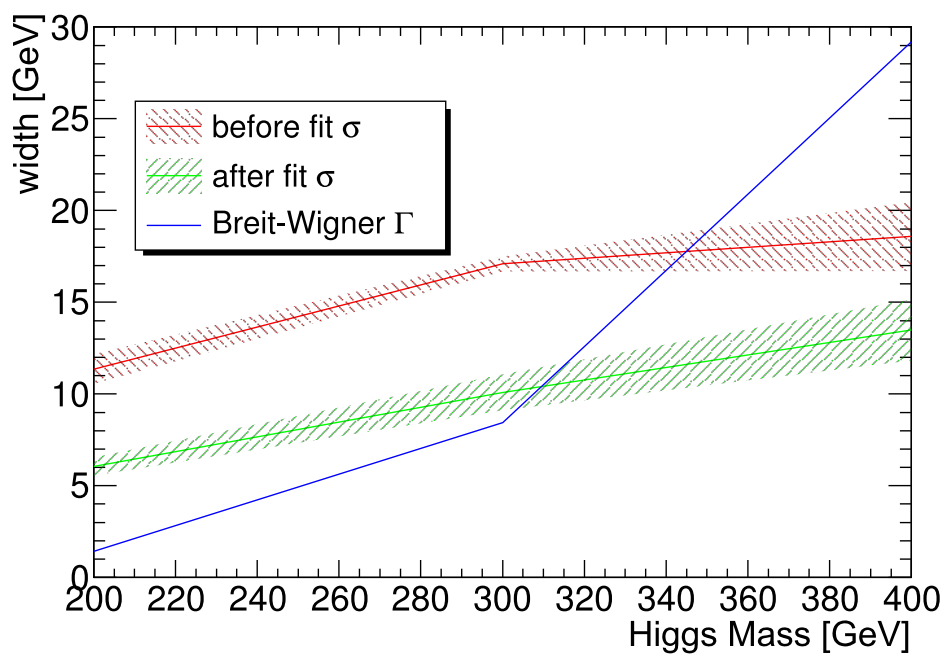


Figure 5.26: Contribution of the decay width and experimental resolution to the overall width of the reconstructed Higgs invariant mass distributions. The Gaussian resolution parameter is shown before and after the application of the kinematic fit.

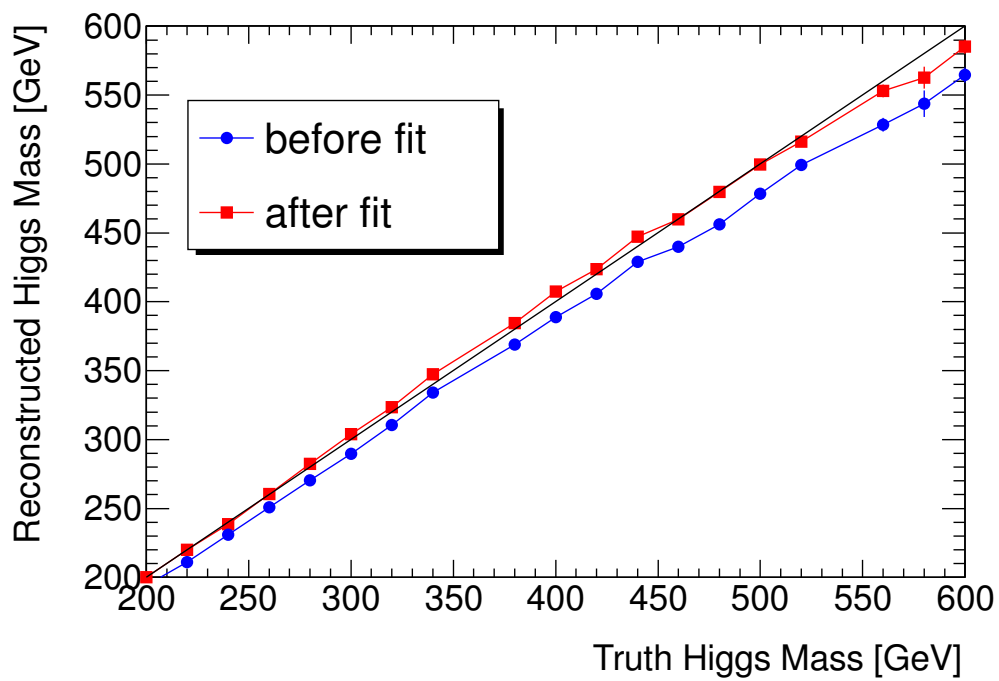
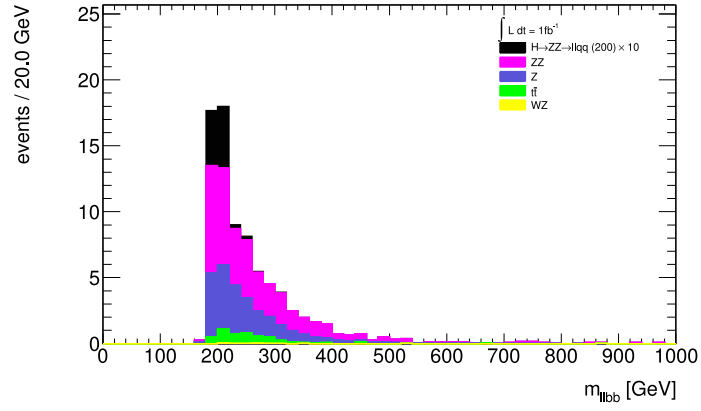
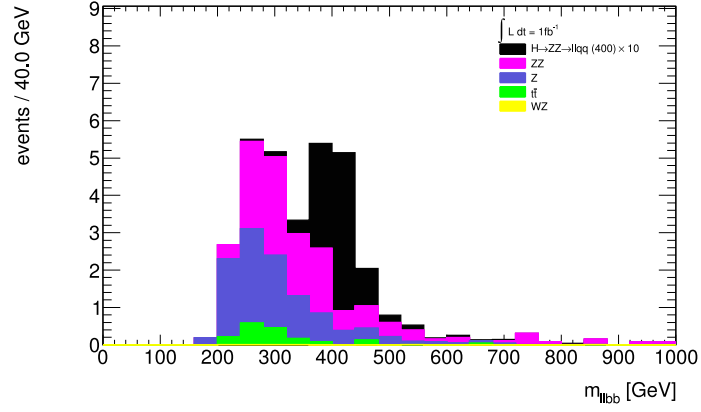


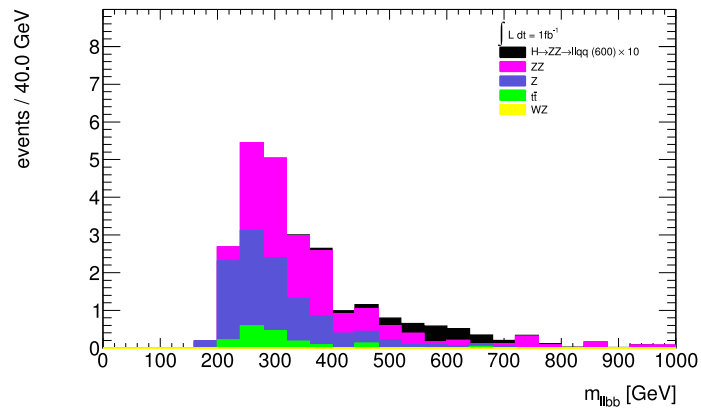
Figure 5.27: Reconstructed mass versus the truth mass for several mass points. The fit provides an improvement in the mass measurement.



(a) $m_H = 200 \text{ GeV}$



(b) $m_H = 400 \text{ GeV}$



(c) $m_H = 600 \text{ GeV}$

Figure 5.28: Reconstructed $llbb$ mass distribution including backgrounds after the full event selection and kinematic fit.

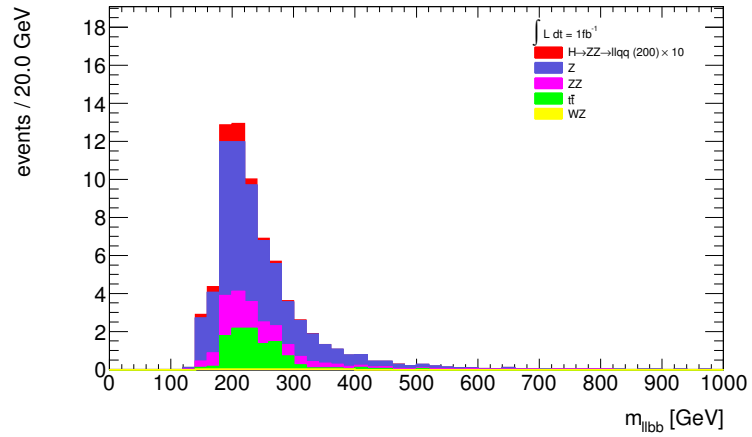
analysis cuts except for the di-jet invariant mass cut. Events in the di-jet mass sidebands, $40 < m_{jj} < 70$ GeV or $110 < m_{jj} < 150$ GeV, were selected for the control sample. Figure 5.29 shows the m_{ljj} distribution for this control sample. A total of 45 (18) Z +jets events per inverse femtobarn are expected to pass in this control region with the low mass (high mass) selections.

A control sample to isolate $t\bar{t}$ events was defined by applying all analysis cuts except for the di-lepton invariant mass cut and the E_T^{miss} cut. Events with $60 < m_{ll} < 83$ GeV or $99 < m_{ll} < 150$ GeV, and $E_T^{\text{miss}} > 30$ GeV were selected. Figure 5.30 shows the m_{ljj} distribution for this control sample. A total of 73 (41) $t\bar{t}$ events per inverse femtobarn are expected to pass in the control region with the low mass (high mass) selections.

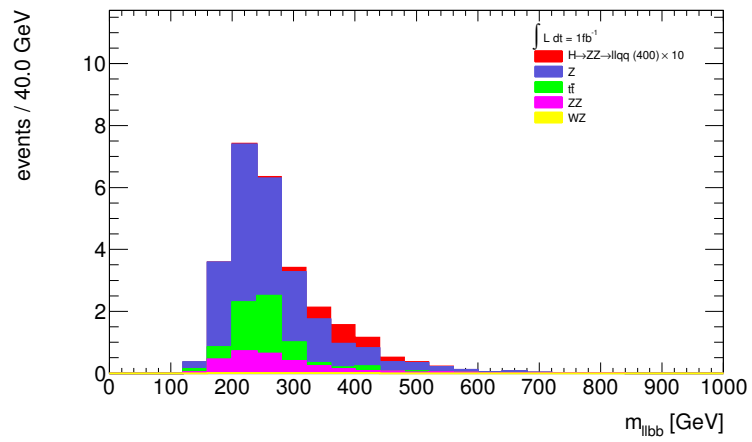
5.5 Systematic Effects

The following systematic effects were estimated. The scale of systematic uncertainties were taken from [27] unless otherwise stated below.

- The uncertainty in signal cross-section varies with the Higgs mass. The error on the overall normalisation varies from 15% to 20% [13]. This was conservatively taken to be 20% for all mass points. Improved theoretical calculations and better constraints on PDFs may reduce this uncertainty in future.
- The background rates will be constrained by normalising to event rates in background dominated control samples defined in section 5.4. In

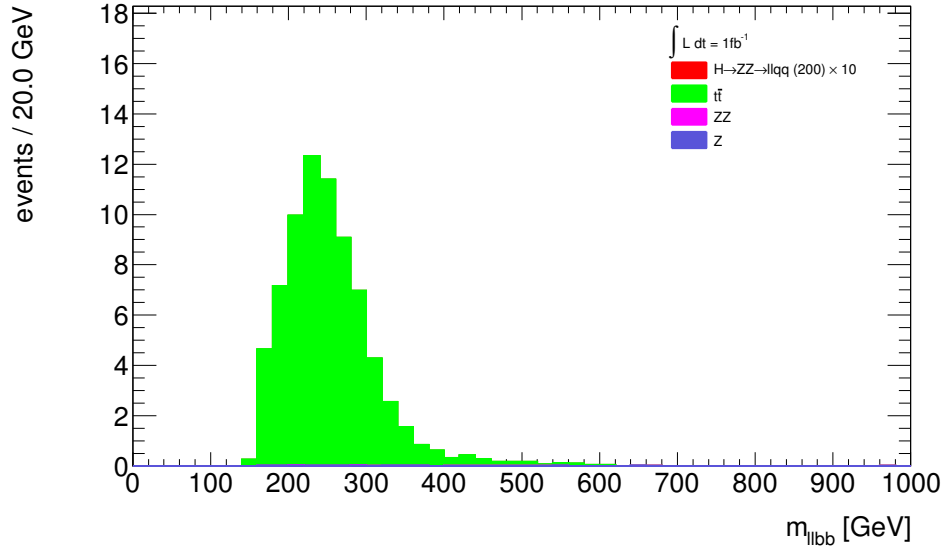


(a) Low mass selection

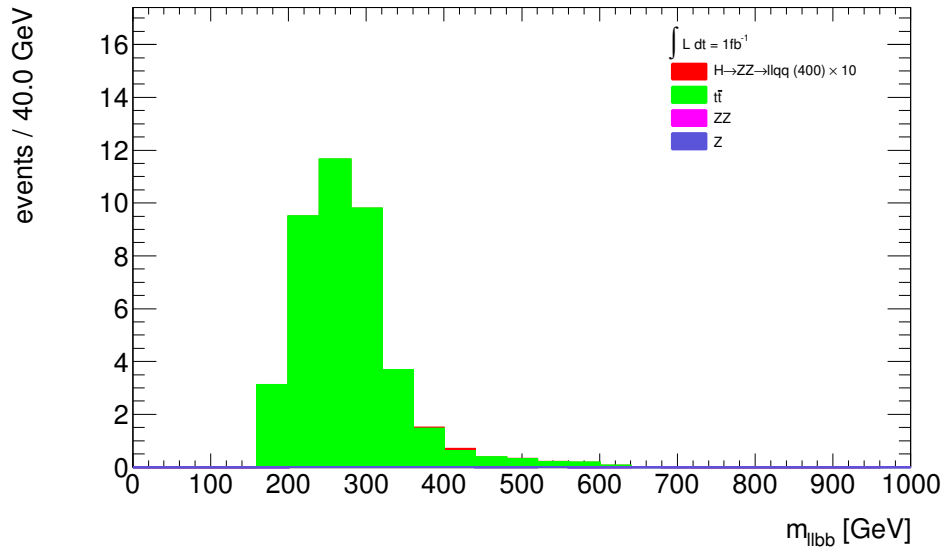


(b) High mass selection

Figure 5.29: m_{ljj} distribution for events in the Z control region normalised to 1 fb^{-1} .



(a) Low mass selection



(b) High mass selection

Figure 5.30: m_{ljj} distribution for events in the $t\bar{t}$ control region normalised to 1fb^{-1} .

this case the systematic error may be taken from the statistical error in the control sample. Based on the statistics in these control regions expected for 1 fb^{-1} , systematic shifts of 13% and 17% were applied to the Z and $t\bar{t}$ background normalisations respectively. These errors were assumed to be uncorrelated between channels. As data are accumulated, these statistical uncertainties will be reduced. Normalising to the control regions also has the advantage of cancelling out some of the other systematic effects.

- Uncertainty on the luminosity has the effect of scaling the event rate across all channels. This systematic was only applied to the signal and its irreducible di-boson background. A nominal uncertainty of 10% was applied. This is a conservative estimate as the ultimate luminosity precision is expected to be much smaller ($\sim 3\%$). When setting limits, the uncertainty was assumed to be 100% correlated across all affected channels.
- As tight cuts are imposed on the di-jet invariant mass distribution, the variations in the jet energy scale can have significant effects on the event yields. The jet energy scale was varied by 7%. As shown in tables 5.5 and 5.6, these shifts can cause significant shifts in the overall event yield for some processes. When setting limits, the effects were assumed to be 100% correlated across all processes.
- Tight cuts are placed on the b-tagging weight and an accurate modelling of tagging efficiency and light jet rejection is required for this analysis. The effects of systematic shifts in the b-tag weight distri-

bution can affect both the efficiency for tagging true b-jets and the rejection rate of light jets. A 5% uncertainty on the tagging efficiency is assumed for true b-jets. This is implemented by shifting the b-weight cuts applied by ± 0.3 and comparing the event yields to the nominal cut. When setting limits, the effects were assumed to be 100% correlated across channels.

- The electron efficiency was varied by 1%. This was implemented by reweighting the events by a factor $1 \pm \epsilon^N$ where $\epsilon = 1\%$ and N is the number of reconstructed medium electrons in the event. The electron energy scale was also varied by 1%. As shown in tables 5.5 and 5.6, these shifts have a negligible effect on the overall event yields.
- The muon efficiency was varied by 0.3%. This was implemented by reweighting the events by a factor $1 \pm \epsilon^N$ where $\epsilon = 0.3\%$ and N is the number of reconstructed muons in the event. The muon energy scale was also varied by 0.3%. As shown in tables 5.5 and 5.6, these shifts have a negligible effect on the overall event yields.
- The very low rate of signal events necessitates harsh cuts which cut out much of the background. With such high background rejection, even with large Monte Carlo event samples, the statistical uncertainty on the simulated backgrounds can become significant. This is estimated as $1/\sqrt{N}$ where N is the number of unweighted simulated events that pass the selection. As shown in tables 5.5 and 5.6, this can become significant for some channels. Indeed, it is the dominant uncertainty in the $t\bar{t}$ channel. These uncertainties could be reduced by generating

larger samples of Monte Carlo data.

The effects of these systematics on the overall event yield are summarized in tables 5.5 and 5.6.

5.6 Expected Limits

Expected confidence limits were calculated using the CL_s method [28]. This method of calculating confidence limits has been used in previous Higgs searches at both LEP and Tevatron experiments. The results are binned in terms of a discriminating variable, in this case the reconstructed mass, m_{lljj} , and each bin is treated as a statistically independent counting experiment. This method allows results from multiple search channels to be combined by adding them in as additional statistically independent bins.

The likelihood given N observed events in the i -th bin is calculated with the Poisson distribution,

$$L(N_i, \mu) = \frac{\mu^{N_i} e^{-\mu}}{N_i!}, \quad (5.8)$$

where μ is the expected number of events. A test statistic, Q , is constructed from the likelihood ratio,

$$Q = \prod_i L(N_i, s_i + b_i) / L(N_i, b_i), \quad (5.9)$$

where s_i and b_i are the expected number of signal and background events in the i -th bin. Typically, the log likelihood ratio, $-2 \ln Q$, is used instead of

Table 5.5: Systematic effects on event yield for signal and background with the low mass selection. The signal mass is $m_H = 400$ GeV. Effects of 1% or less have been omitted.

Systematic Effect (%)	Channel			
	$H \rightarrow llqq$	ZZ	Z	$t\bar{t}$
normalisation	± 20	± 11	± 15	± 12
jet energy scale	-7, -2	2, -12	1, 1	2, 13
b-tagging efficiency	-2, 3	-2, 4	± 0	-3, 2
electron efficiency	-	-	-	-
electron energy scale	-	-	-	-
muon efficiency	-	-	-	-
muon energy scale	-	-	-	-
luminosity	± 10	± 10	-	-
MC statistics	± 3	± 4	± 5	± 21

Table 5.6: Systematic effects on event yield for signal and background with the high mass selection. The signal mass is $m_H = 400$ GeV. Effects of 1% or less have been omitted.

Systematic Effect (%)	Channel			
	$H \rightarrow llqq$	ZZ	Z	$t\bar{t}$
normalisation	± 20	± 11	± 15	± 12
jet energy scale	-8, -1	-2, -14	3, 1	-2, 8
b-tagging efficiency	-2, 3	-4, 1	± 0	-2, 4
electron efficiency	-	-	-	-
electron energy scale	-	-	-	-
muon efficiency	-	-	-	-
muon energy scale	-	-	-	-
luminosity	± 10	± 10	-	-
MC statistics	± 3	± 8	± 8	± 29

using Q directly.

In the CL_s technique, the probability density functions of the test statistic are computed under the background only and signal plus background hypotheses. The p -value of the data being consistent with the signal plus background hypothesis, p_{s+b} , is the probability to find $-2\ln Q$ greater than or equal to the observed value under the signal plus background hypothesis. Similarly, the p -value for the background hypothesis, p_b , is the probability to find $-2\ln Q$ less than or equal to the observed value under the background only hypothesis. CL_s is defined as,

$$CL_s = \frac{p_{s+b}}{1 - p_b}. \quad (5.10)$$

If $CL_s < 5\%$ then the signal hypothesis is excluded at 95% confidence level or higher.

The CL_s calculation was performed with the MCLIMIT program [3] [4]. Systematic uncertainties are included as a modified¹ Gaussian uncertainty on the s_i and b_i parameters of the model and the effect on the confidence limits are evaluated with a Monte Carlo method.

Systematic uncertainties were implemented as normalisation uncertainties on each background using the values shown in tables 5.5 and 5.6. Uncertainties were assumed to be uncorrelated across channels except where noted in section 5.5.

Figure 5.31 shows the exclusion limits expected with 1 fb^{-1} both with

¹An additional term is added to model asymmetric uncertainties. In the case of symmetric errors the function reduces to a Gaussian distribution. Further details can be found in the referenced material [4]

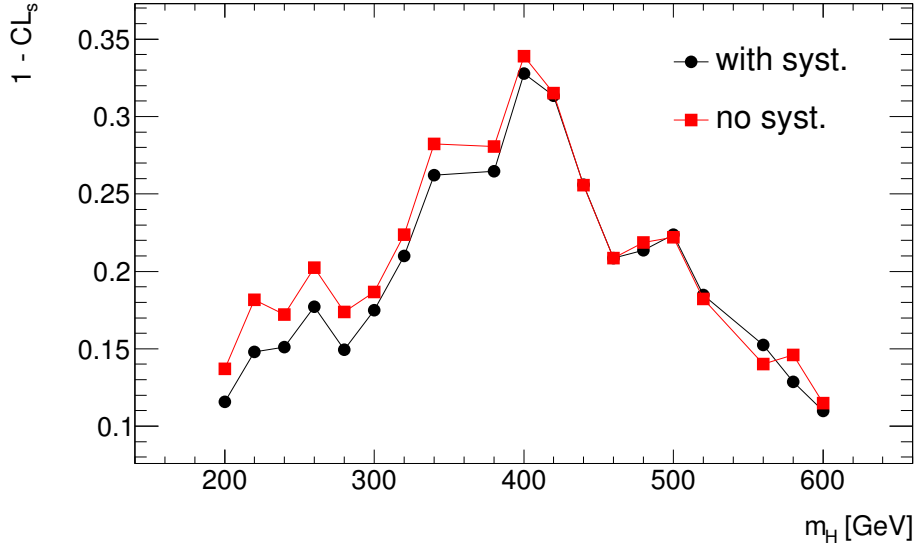


Figure 5.31: Median exclusion confidence limit for 1 fb^{-1} with and without systematic uncertainties.

and without systematic uncertainties included in the calculation. The systematic uncertainties only have a small effect with this quantity of data, the sensitivity is dominated by statistical uncertainties. Figure 5.32 shows the CL_s values with $\pm 1\sigma$ and $\pm 2\sigma$ statistical uncertainties. The statistical uncertainty on the expected limit is large. For example, it is possible to set a tighter limit on the signal production cross-section if the background fluctuates downwards.

The best limits are obtained at $m_H = 400 \text{ GeV}$. At low mass, there are two main causes for the reduced sensitivity. Firstly, as the $\Delta\phi_{jj}$ cut is not applied in the low mass selection and the overall background rates are higher. Secondly, the cuts on the di-lepton and di-jet invariant mass distributions around the Z -boson mass naturally cause the backgrounds to peak around twice the Z mass. In the mid-range mass region, greater than 300 GeV , the

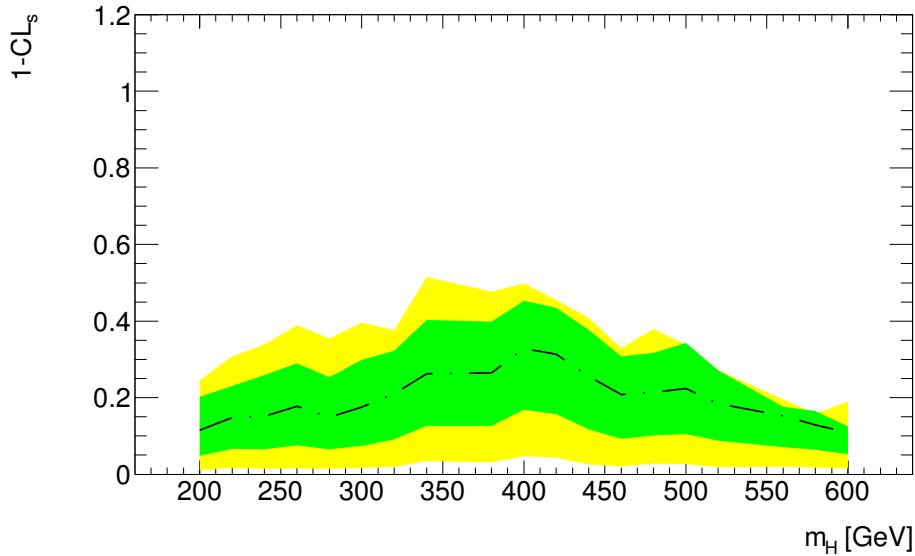


Figure 5.32: Exclusion confidence limits expected at 1 fb^{-1} . The black line shows the median expected limits. The green and yellow bands show the $\pm 1\sigma$ and $\pm 2\sigma$ limits, respectively.

background peak begins to fall and the $\Delta\phi_{jj}$ cut is applied which improves the signal to background ratio. In the high mass range the search sensitivity again begins to fall. Even though the background rates at very high masses are low the signal production cross-section also falls. This is compounded by the increasing width of the signal resonance, which effectively increases the total background in the signal region.

The exclusion limits can be recalculated as the fraction of the Standard Model signal cross-section that would be excluded at the 95% confidence level, as shown in figure 5.33. With 1 fb^{-1} it is possible to excluded a standard-model-like Higgs boson with a mass of 400 GeV and a production cross-section around 8 times the Standard Model. Note that this is using the $H \rightarrow llbb$ channel alone. When combined with other channels

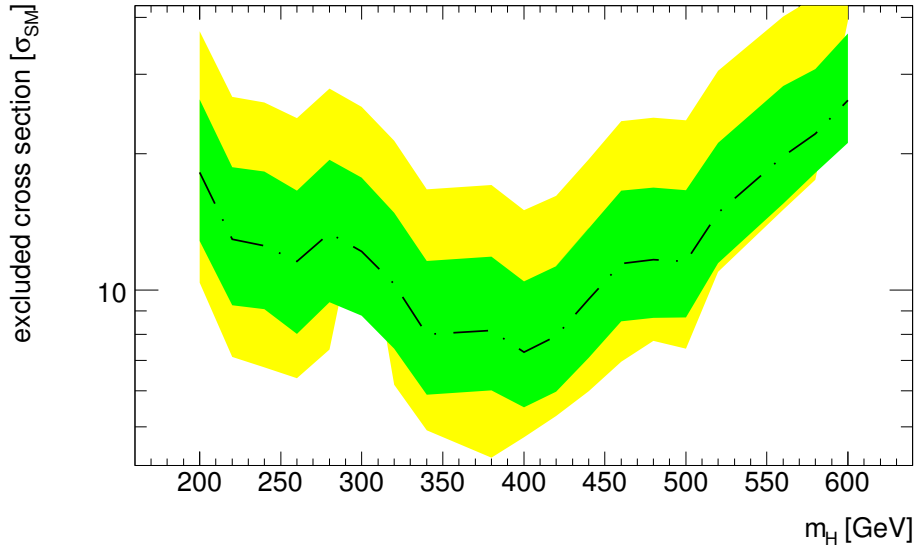


Figure 5.33: Expected exclusion limits shown as a ratio of the predicted Standard Model cross-section. The black line shows the median expected limits. The green and yellow bands show the $\pm 1\sigma$ and $\pm 2\sigma$ limits, respectively.

(and experiments), the overall sensitivity of ATLAS (the LHC) will be much stronger.

The expected excluded cross-section for various total integrated luminosities are shown in figures 5.34 and 5.35 including and excluding systematic uncertainties. Without systematic uncertainties, these channels begin to exclude the Standard Model Higgs boson for some mass ranges around 50 fb^{-1} . However, at large luminosities the systematic effects begin to dominate. Future analyses will need to work to bring down the systematic uncertainties. It should be noted, however, that the estimates here are conservative and section 5.5 highlights several ways in which the overall uncertainty may be reduced.

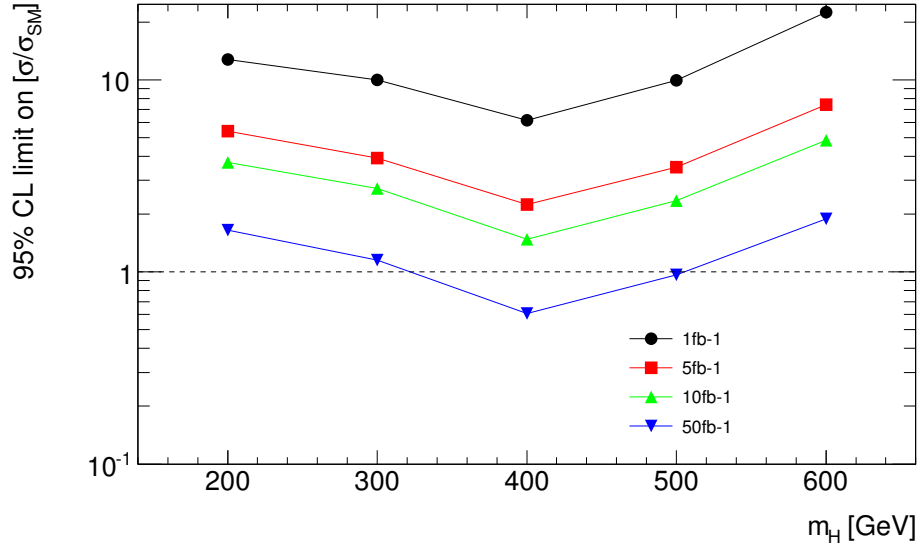


Figure 5.34: Median exclusion limits shown as a ratio of the predicted Standard Model cross-section for various integrated luminosities. No systematic uncertainties were included.

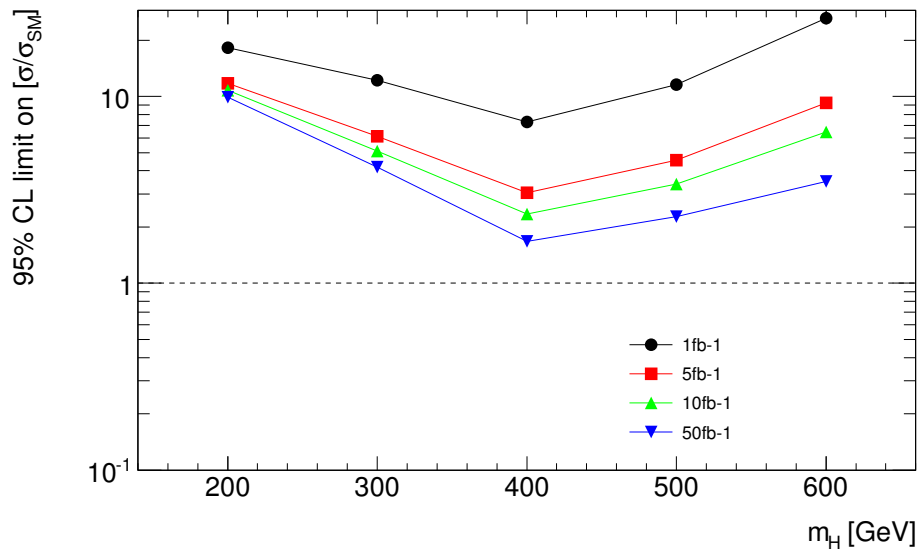


Figure 5.35: Median exclusion limits shown as a ratio of the predicted Standard Model cross-section for various integrated luminosities. The nominal systematic uncertainties were included.

5.7 Future Improvements

This analysis suffers from a very low signal efficiency as harsh cuts are required to reduce the substantial backgrounds. There are several areas where this analysis may be improved.

b -tagging provides one of the best cuts against the Z plus light jets background, but it also proves to be one of the most inefficient cuts. As two b -tags are required, an improvement in b -tagging performance would significantly improve the signal efficiency. More advanced b -tagging algorithms exist that make improvements over the simple impact parameter and single secondary vertex reconstruction. For example the JetFitter algorithm attempts to find the secondary vertices from the decay of both the b and c hadrons [29].

The use of multi-variate techniques, for example artificial neural nets, may be necessary to maximise the potential of this channel. A multi-variate technique typically can achieve better separation of signal from background with greater efficiency than a cuts based approach. They may also be used to provide higher statistics distributions that may be fitted to extract the Z and $t\bar{t}$ background rates with lower uncertainty.

Chapter 6

Backgrounds to $H \rightarrow ZZ \rightarrow llqq$ in Early LHC Data

During the 2010 run of the LHC, ATLAS recorded 45.0 pb^{-1} of data. Much more integrated luminosity is needed to exclude or observe a Standard Model Higgs signal. However, these are sufficient data to observe the dominant backgrounds to the $H \rightarrow llqq$ process. In this chapter, methods to isolate the main backgrounds and to determine their normalisation from data are presented. Event yields observed in data are compared with those predicted with Monte Carlo simulation.

6.1 Monte Carlo Corrections

The 2010 run was the first time that the LHC collided beams at high intensity and with significant amounts of integrated luminosity delivered. These data were used by both the LHC and the experiments to commission the

apparatus. Consequently, some parts of the reconstruction that were used in the analysis of chapter 5 were not fully commissioned. There are several areas where the simulation and data do not agree. Eventually, as the understanding of the detector is improved, the simulation will describe the data. At present, several corrections must be applied to the Monte Carlo simulation. The following modifications to the analysis presented in chapter 5 were made.

- The IP3D+SV1 b -tagging algorithm was not commissioned at the time of this analysis. Instead, a less sophisticated secondary vertex algorithm, SV0, was used. This algorithm is based on the distance between the primary vertex and the secondary decay vertex. The weight is formed from the ratio of the decay length to its uncertainty. The cut was placed at a weight of 5.72 giving an efficiency of 54% for $H \rightarrow llbb$ events with $m_H = 400$ GeV.
- A simplified missing energy calculation based on calorimeter clusters was used. No information from reconstructed electrons or jets was used. Additional muon momentum terms were added as these typically leave little energy in the calorimeters. The E_T^{miss} cut was widened to 50 GeV to account for the reduced resolution of this algorithm.
- The electron ID cuts, described in section 5.2.1, were modified. Electron shower shape distributions were found to differ between data and simulation. The definition of the “Medium” electron ID was modified to relax these poorly described cuts, to ensure that the electron ID efficiencies in simulation more closely match that observed in data.

- The detector suffers from various dead regions in the calorimeter which are not included in the simulation. In particular, large dead regions in the e.m. calorimeters lead to low electron reconstruction efficiency. Electrons impacting these regions were excluded from the analysis in both data and simulation.
- The trigger menus were constantly evolving during 2010. As a result, the trigger set-up in data and the simulation are not identical. For data events, the lowest p_T , unscaled, single lepton trigger item for each run was used. As the analysis requires two isolated high- p_T leptons, the trigger efficiency with respect to the analysis cuts is very high. Consequently, the discrepancy between trigger definitions used in simulation and data has no significant effects.

6.2 Event Preselection

ATLAS produces huge amounts of data. A pre-selection was applied to reduce the data volume to a manageable level. Only events passing certain data quality flags were accepted. During each run, data quality flags were recorded detailing the status of each part of the detector. Runs are sub-divided and data quality flags are set for each luminosity block. This analysis required the following detector components to have “good” status: the solenoid and toroid magnets, the Level-1 Trigger and the inner tracking. Also, data quality flags were set for higher level reconstructed objects. This analysis required “good” status for: electrons, muons, jets, E_T^{miss} and b -tagging. A total integrated luminosity of 34.6 pb^{-1} was collected passing

these data quality criteria.

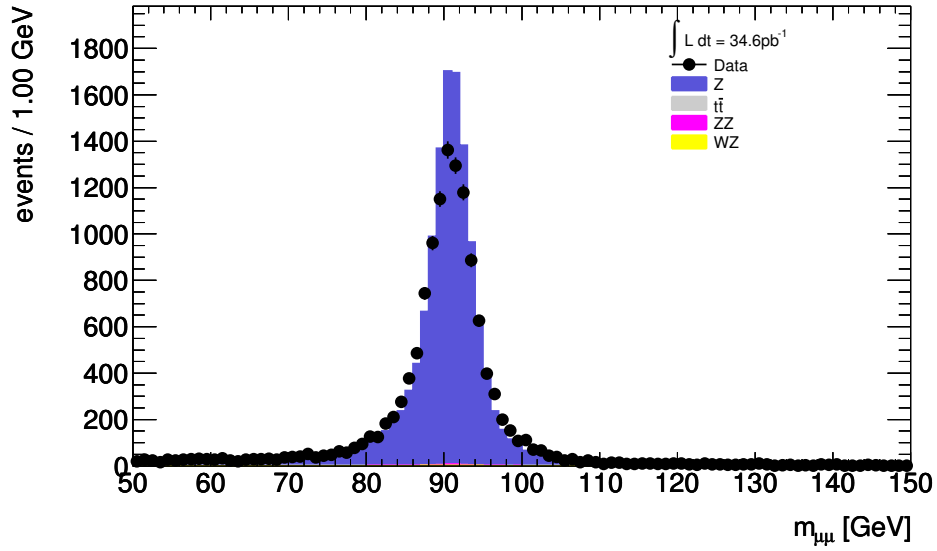
Only events with at least 2 electrons (muons) with $p_T > 10$ GeV and $|\eta| < 2.5$ ($|\eta| < 2.7$) were accepted. Both electrons were required to pass the loose electron ID. Muons were required to have combined tracks in the inner detector and muon spectrometer except beyond the range of the precision inner tracking, $|\eta| > 2.5$, where stand-alone muons were accepted.

6.3 Kinematic Distributions

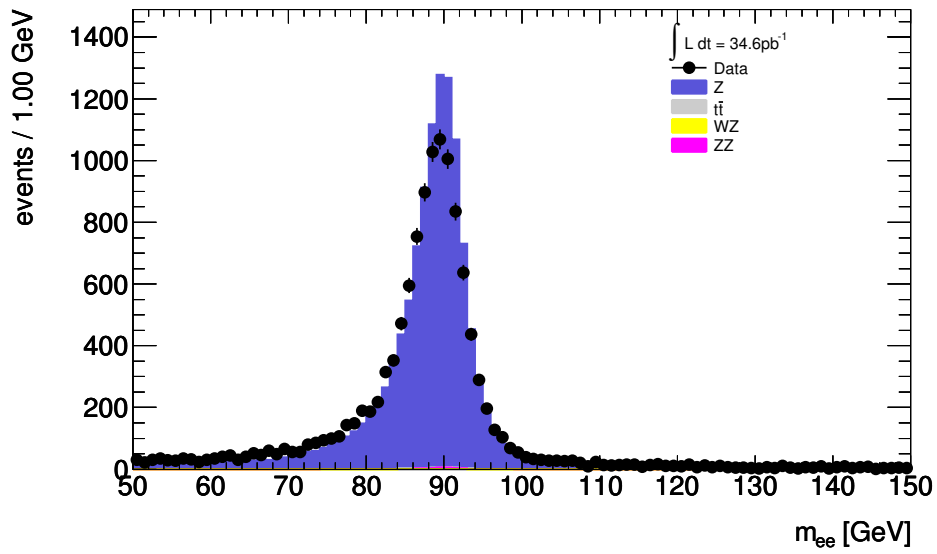
The object selection described in sections 5.2.1, 5.2.2 and 5.2.3, with the modifications described in section 6.1, was applied to the pre-selected dataset. Figure 6.1 shows the observed di-lepton mass distribution.

The jet multiplicity in events passing the di-lepton mass cut is shown in figure 6.2. Monte Carlo samples of Z +jet events were generated with both Pythia [30] and ALPGEN [31]. ALPGEN was found to more accurately reproduce the observed jet multiplicity distribution. Therefore the ALPGEN sample was chosen to model the Z +jet processes in this analysis.

Events were required to have 2 or 3 jets. The lepton invariant mass distributions after making this cut are shown in figure 6.3. This selection is dominated by Z +jets processes. Kinematic distributions on which cuts were placed are shown in figure 6.4 and the resulting $lljj$ invariant mass distribution is shown in figure 6.5. The simulation provides a good description of the shapes of these distributions.



(a) $\mu\mu$



(b) ee

Figure 6.1: Inclusive di-lepton invariant mass spectra for (a) electrons and (b) muons.

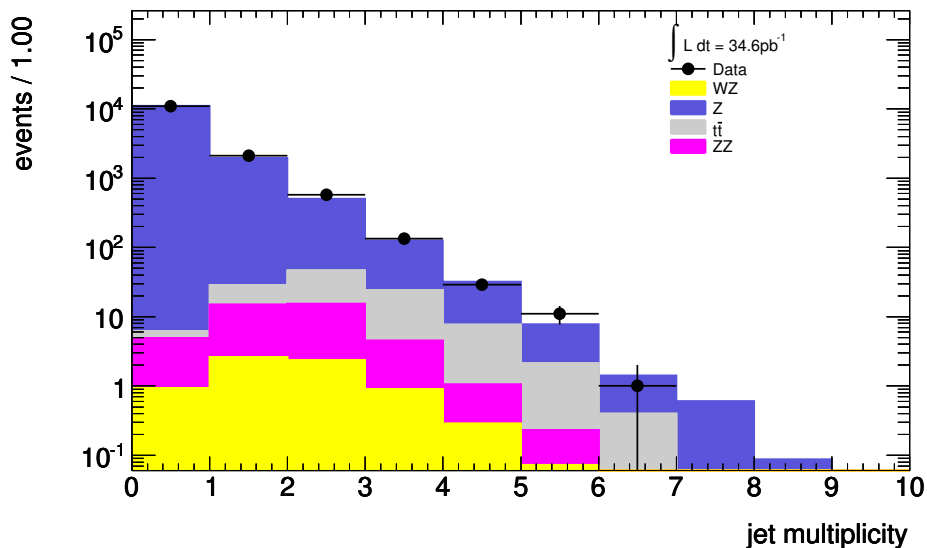
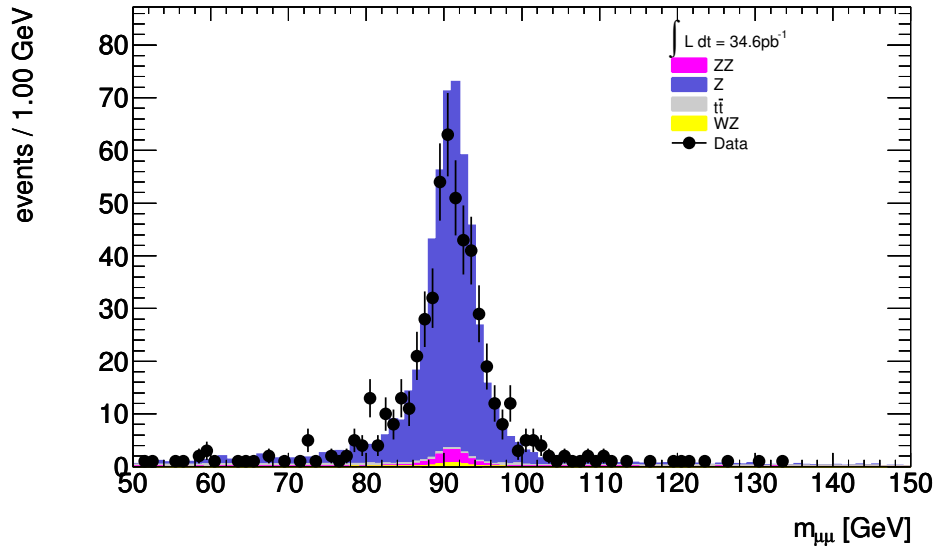


Figure 6.2: Jet multiplicity in di-lepton events.

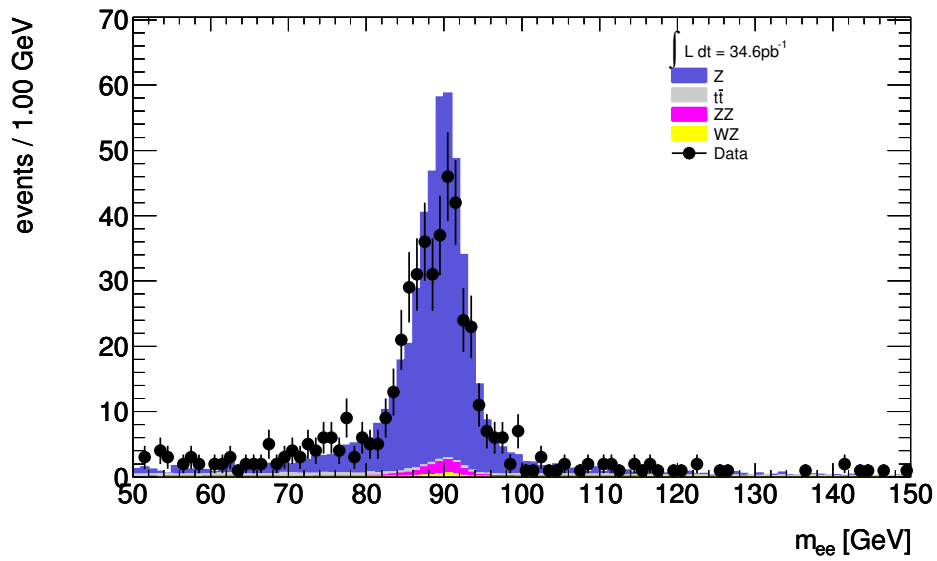
6.4 QCD Background

As stated in section 5.1.5, there are two distinct sources of QCD background affecting this search. First, jets of hadrons can be mistakenly reconstructed as electrons or muons. Pion decay can also provide a source of muons and photon conversions provide a source of electrons. Second, the weak decays of heavy hadrons can produce secondary electrons and muons. The contamination from the latter can be estimated from Monte Carlo. It is impractical to generate sufficient Monte Carlo statistics to study the fake lepton background. Therefore, its contribution must be extracted from the data.

Real leptons from a Z always have opposite charge. A pair of fake muons have no constraint on their charge and are equally likely to be reconstructed with equal or opposite charge. The contribution from jets that fake muons can be estimated by examining the same-sign lepton distribution. Figure

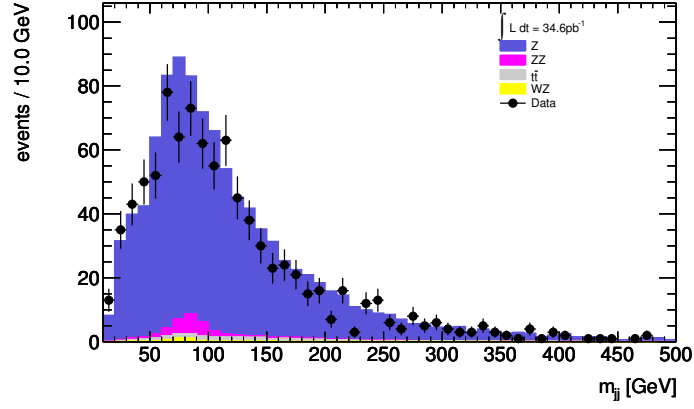


(a) $\mu\mu jj$

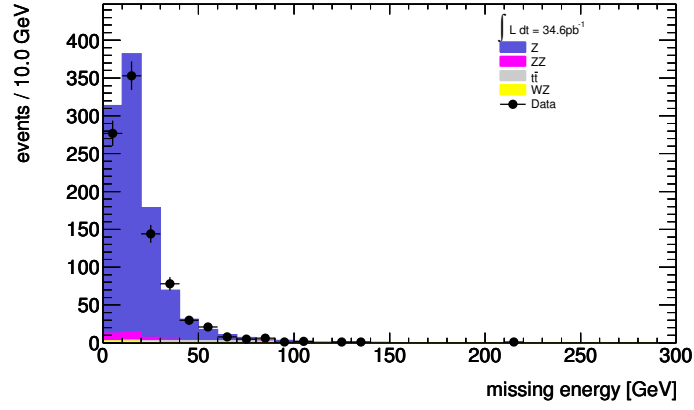


(b) $eejj$

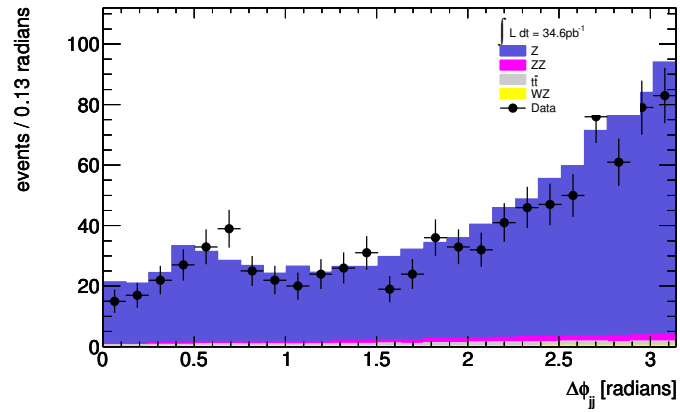
Figure 6.3: Di-lepton invariant mass spectra for events with $2 \leq N_{\text{jets}} \leq 3$. The data are divided between (a) the electron channel and (b) the muon channel.



(a) Di-jet mass in Zjj events



(b) E_T^{miss} in Zjj events



(c) $\Delta\phi_{jj}$ in Zjj events

Figure 6.4: Kinematic distributions for all events with $83 < m_{ll} < 99$ GeV and $2 \leq N_{\text{jets}} \leq 3$.

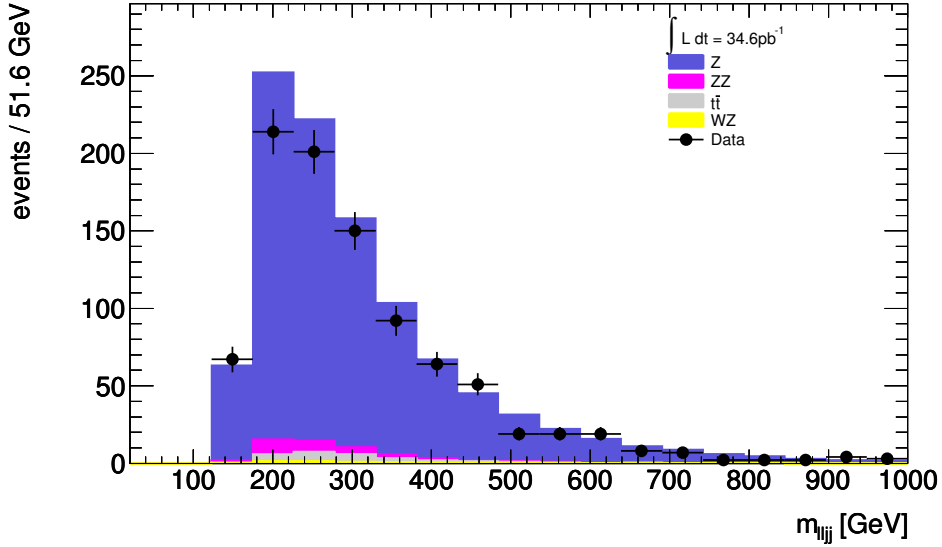


Figure 6.5: $lljj$ invariant mass of all events with $83 < m_{ll} < 99$ GeV and $2 \leq N_{\text{jets}} \leq 3$.

6.6 shows these distributions in the muon channel. Only 3 same-sign muon events were observed in the di-muon mass window. These events did not pass the subsequent analysis cuts.

The muon background from the decay of heavy flavours was estimated from Monte Carlo and no events passed the final selection. Consequently, the QCD background in the muon channel can be assumed to be negligible.

The electron channel has a much higher QCD background. Figure 6.7 shows the di-electron mass distributions for same sign Medium electron pairs. However, due to multiple scattering and bremsstrahlung, it is possible to incorrectly reconstruct the charge of an electron. Approximately 4% of Monte Carlo $Z \rightarrow ee$ events were reconstructed with a pair of same-sign electrons.

The QCD background can more clearly be seen by reversing the electron ID cuts. The di-electron mass distribution for Loose but not Medium electron

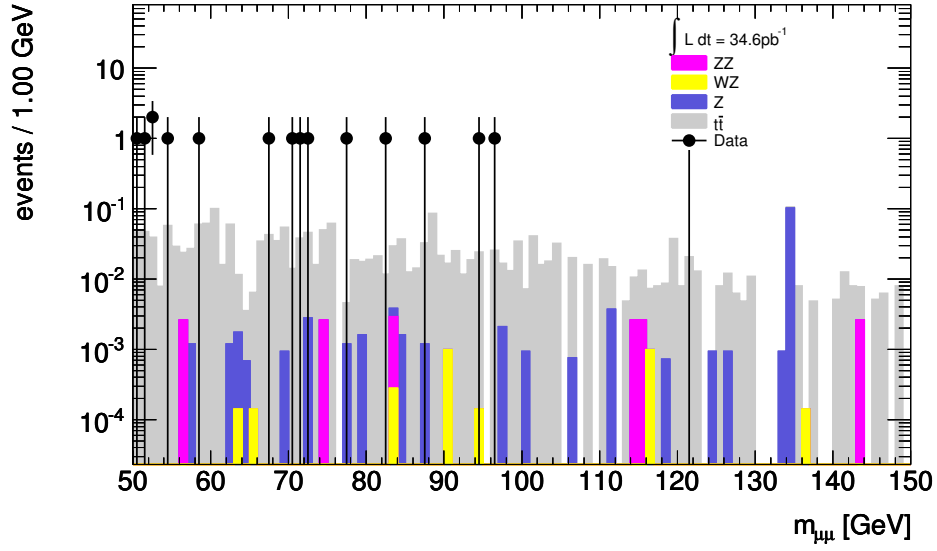


Figure 6.6: Di-muon same-sign lepton distribution.

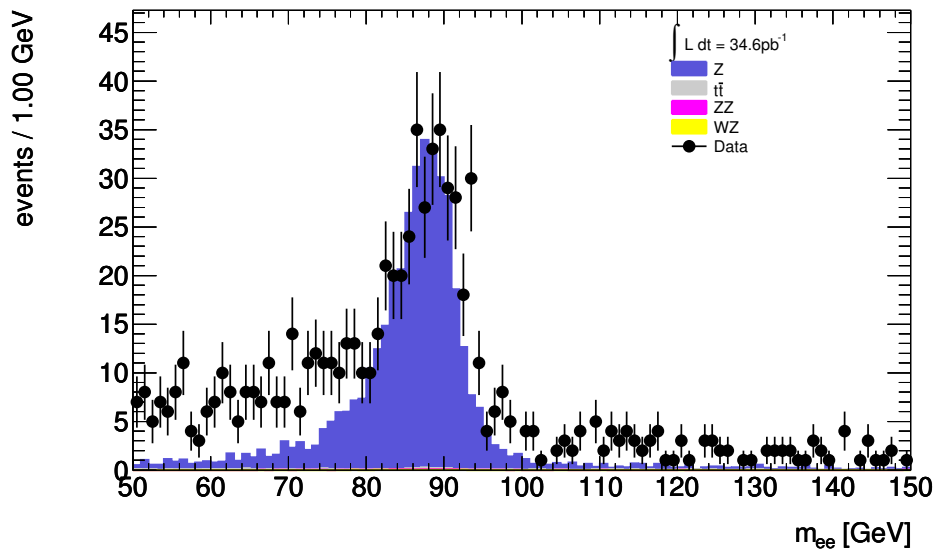


Figure 6.7: Di-electron invariant mass distribution for Medium electron pairs with same sign charge.

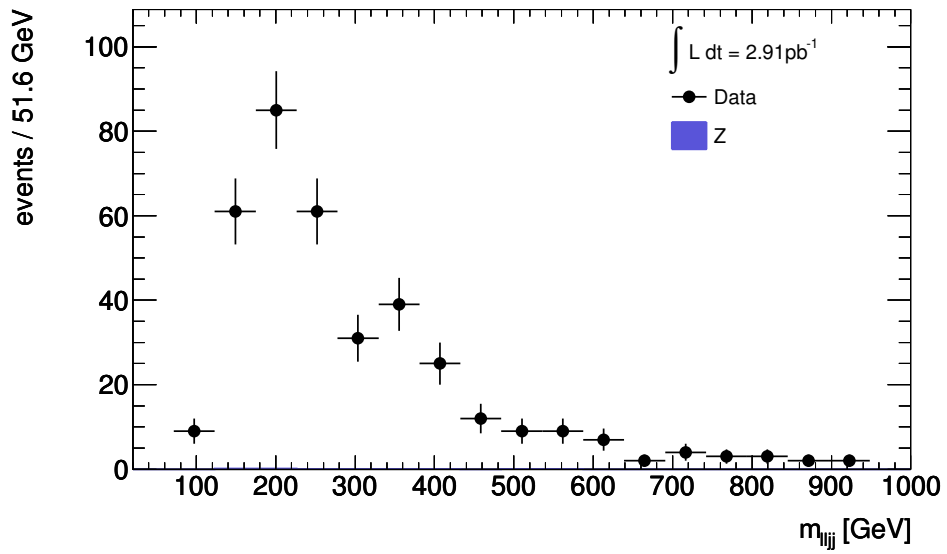
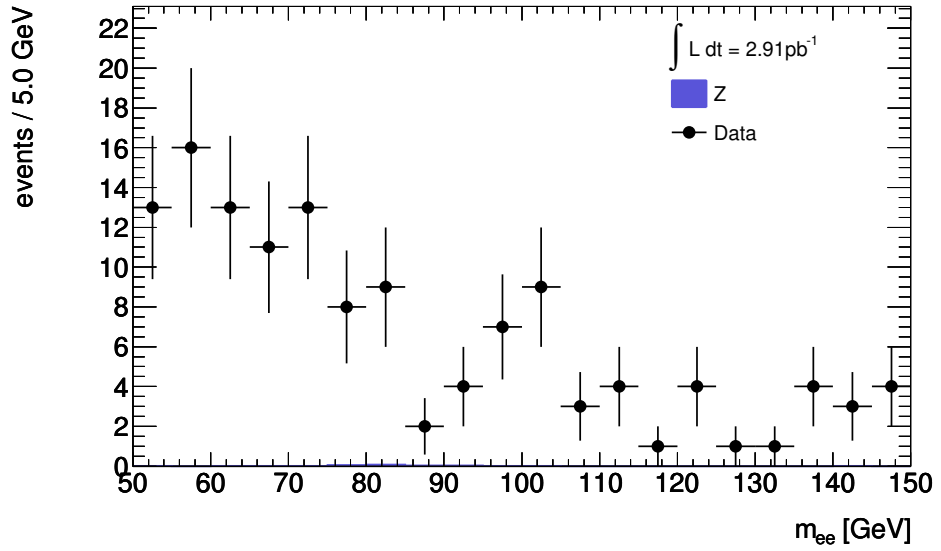


Figure 6.8: m_{ee} QCD enhanced data sample containing a pair of Loose but not Medium electrons.

pairs in events with 2 or 3 jets is shown in figure 6.8. There is very little contamination from Z events. This QCD enhanced dataset can be used to describe the shape of the QCD background.

The normalisation can be estimated by comparing the “Loose-Loose” electron background with the “Medium-Loose” background. If the efficiency for a fake Loose electron to also pass the Medium electron cuts is ϵ_M , then the event yields in each dataset are proportional to,

$$N_{LL} \propto (1 - \epsilon_M)^2, \quad (6.1)$$

$$N_{ML} \propto 1 - (1 - \epsilon_M)^2 - \epsilon_M^2 = 2(\epsilon_M - \epsilon_M^2), \quad (6.2)$$

$$N_{MM} \propto \epsilon_M^2, \quad (6.3)$$

where N_{MM} , N_{ML} and N_{LL} refer to the exclusive “Medium-Medium”, “Medium-Loose” and “Loose-Loose” datasets respectively. Explicitly, equation 6.3 is the efficiency for selecting exactly two medium electrons. Equation 6.1 is the inefficiency for selecting a medium electron squared, which is equivalent to the efficiency for selecting exactly two loose electrons as the pre-selection requires that electrons must be either loose or medium. Equation 6.2 is the remaining possible combinations of electron ID and so is equations 6.3 and 6.1 subtracted from unity. From equations 6.2 and 6.1, ϵ_M can be expressed in terms of the ratio of N_{ML} to N_{LL} ,

$$R = N_{ML}/N_{LL}, \quad (6.4)$$

$$\epsilon_M = \frac{R}{R + 2}. \quad (6.5)$$

Hence, to normalise the “Loose-Loose” background to the “Medium-Medium” scale the appropriate scale factor is,

$$N_{\text{MM}}/N_{\text{LL}} = \frac{\epsilon_M^2}{(1 - \epsilon_M)^2}. \quad (6.6)$$

This procedure assumes that the efficiency for identifying each fake lepton as Medium electrons is fixed and independent of event kinematics.

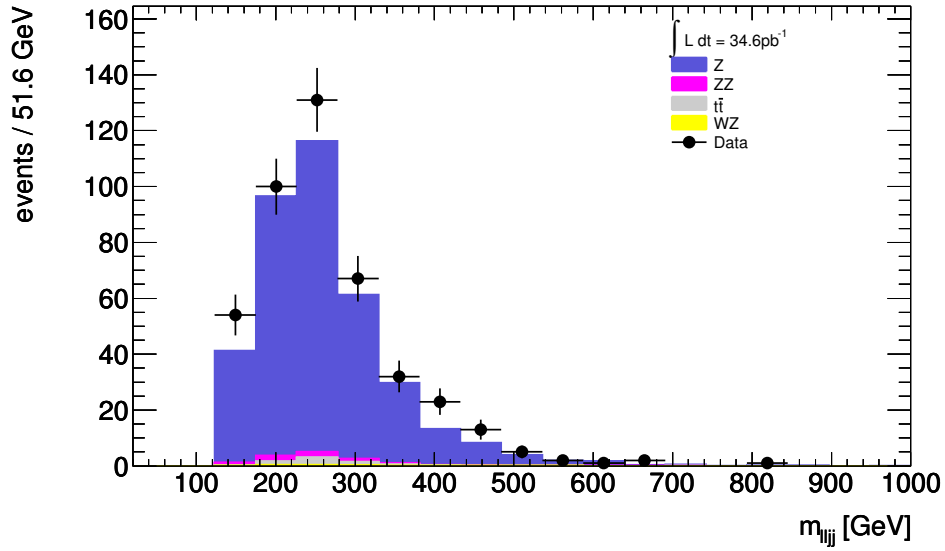
N_{LL} was estimated directly from the observed event yields. The N_{ML} sample has a 10% Z +jet contamination that was subtracted based on the Monte Carlo prediction. To avoid trigger bias a looser trigger selection was applied that was only available unrescaled during early running periods and therefore the available luminosity for this estimate is lower. In 2.91 pb^{-1} 148 events were observed in the exclusive Loose-Loose sample with a negligible non-QCD background. 77 events were observed in the exclusive Medium-Loose sample with a predicted non-QCD background of 7 events, predominantly from Z +jets. From equation 6.4, 6.5 and 6.6, the estimated normalisation factor is $N_{\text{MM}}/N_{\text{LL}} = (5.6 \pm 0.1)\%$. A total of 9 (2) Loose-Loose events passed the other low mass (high mass) analysis cuts excluding b -tagging. This gives a total estimated background in 2.91 pb^{-1} of (0.50 ± 0.18) and (0.11 ± 0.07) events for the low and high mass selection respectively. This gives an estimated QCD background in 34.6 pb^{-1} the untagged data sample of (5.9 ± 2.1) and (1.3 ± 0.8) . No events from the Loose-Loose dataset passed the full event selection, including the b -tagging cut. Hence data is required to estimate the QCD contamination of the b -tagged dataset.

6.5 Z Background

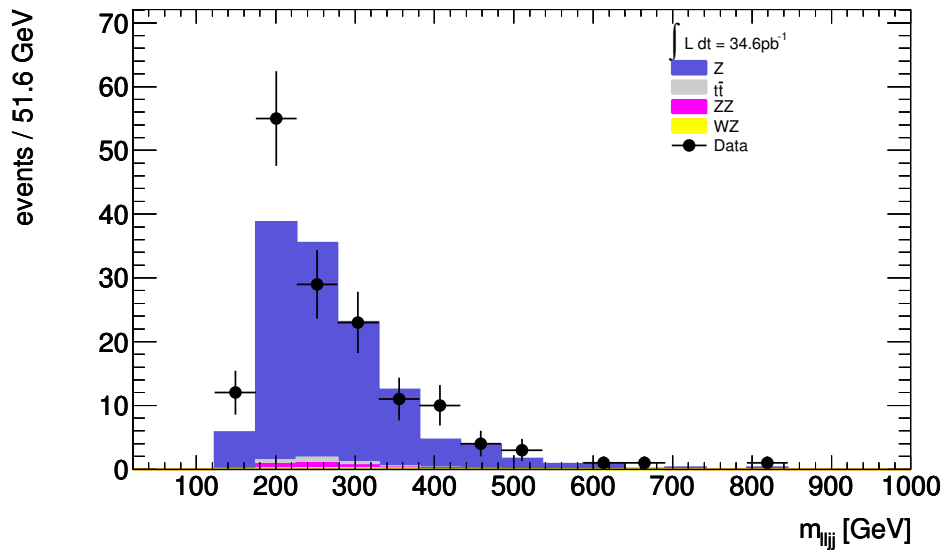
The Z +jets background is by far the dominant background when no b -tagging is applied. A signal free region can be found by looking in side-bands around the jet-jet invariant mass cut. The side bands were defined to be $40 < m_{jj} < 70$ GeV and $110 < m_{jj} < 150$ GeV. Figure 6.9 shows the $lljj$ invariant mass distributions in the signal and side band regions. This Z enriched control sample can be used to normalise the Monte Carlo to the data. A total of 150 (431) events were observed in data, compared to 129 (376) expected from simulation with the high (low) mass selections. This gives a normalisation coefficient of (Data/MC) of 1.17 ± 0.10 (1.15 ± 0.06) for the high (low) mass selections. The statistical uncertainty on this normalisation can provide the systematic uncertainty on the Z background in the limit calculation. Once sufficient luminosity can be recorded a similar procedure may be used to estimate the background from b -tagged Z events.

6.6 Top-quark Background

The top background can be isolated by looking in the side bands around the Z peak in the di-lepton invariant mass distribution. The side bands were defined to be $60 < m_{ll} < 83$ GeV and $99 < m_{ll} < 150$ GeV. This selection alone is not enough to isolate only top events as a significant number of Z events are expected in these side-bands. A significant fraction of the Z background can be cut out by requiring high E_T^{miss} . Figure 6.10 shows the m_{lljj} mass distribution for events passing the m_{ll} side band cuts with

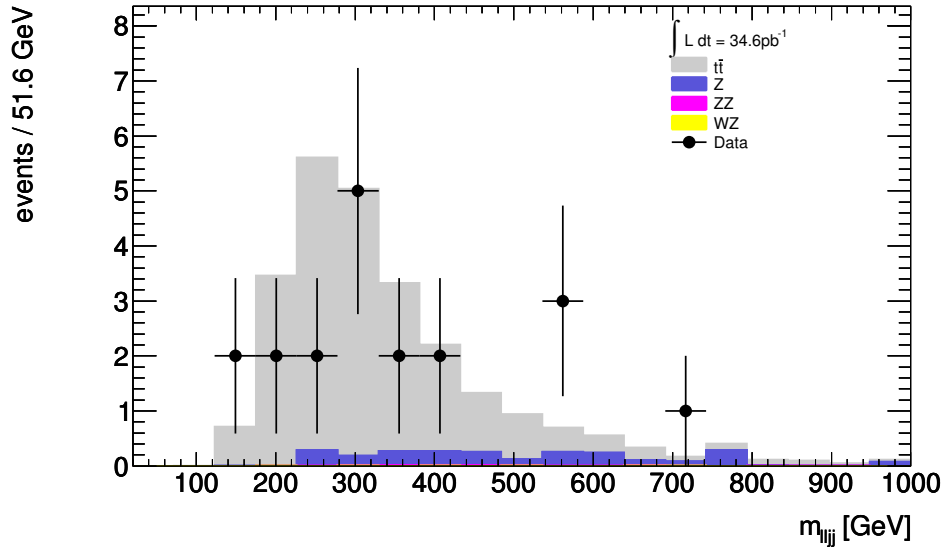


(a) low mass selection

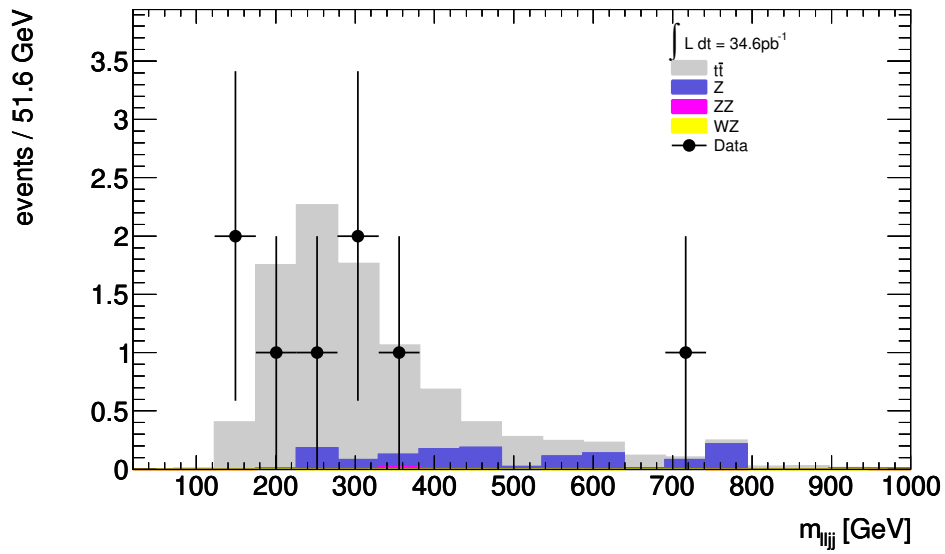


(b) high mass selection

Figure 6.9: m_{ljj} distribution in the jet pair invariant mass side-bands, $40 < m_{jj} < 70$ GeV and $110 < m_{jj} < 150$ GeV.



(a) low mass selection



(b) high mass selection

Figure 6.10: m_{ljj} distribution for events in the di-lepton invariant mass sidebands, $60 < m_{ll} < 83$ GeV and $99 < m_{ll} < 150$ GeV.

$E_T^{\text{miss}} > 50 \text{ GeV}$.

This $t\bar{t}$ enriched control sample can be used to normalise the Monte Carlo to the data. A total of 9 (20) events were observed in data, compared to 9.7 (26) expected from simulation with the high (low) mass selection. This gives a normalisation coefficient of (Data/MC) of 0.9 ± 0.3 (0.78 ± 0.18) with the high (low) mass selection. The statistical uncertainty on this normalisation can provide the systematic uncertainty on the $t\bar{t}$ background in the limit calculation.

When b -tagging is applied the $t\bar{t}$ purity of this control sample will increase. Also, an alternative method to obtain a clean $t\bar{t}$ sample that may be used to provide a cross check, would be to require one electron and one muon. The branching fraction for ee and $\mu\mu$ di-leptonic $t\bar{t}$ events is approximately equal to the branching fraction for $e\mu$ final states. Due to lepton number conservation Z and di-boson events are forbidden from producing $e\mu$ pairs. This would provide a powerful cross check of the previous method.

6.7 Signal Region

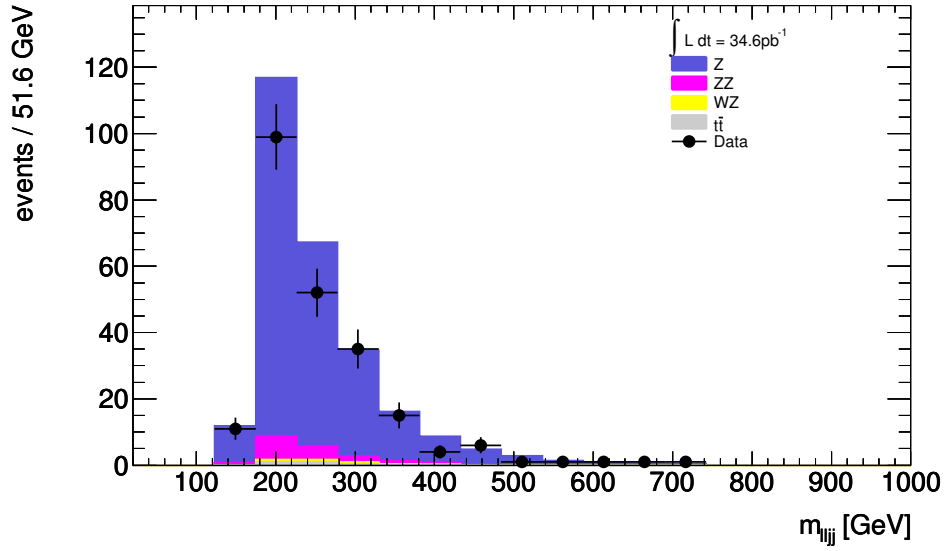
Figure 6.11 (6.12) shows the $lljj$ invariant mass distribution for all events passing the event reconstruction without (with) b -tagging applied. The event yields in data and simulation are summarised in table 6.1. There is good agreement between data and Monte Carlo and no statistically significant excess above background is observed. The predicted signal event yields are shown in table 6.2.

Table 6.1: Comparison of predicted and observed event yields in the signal region.

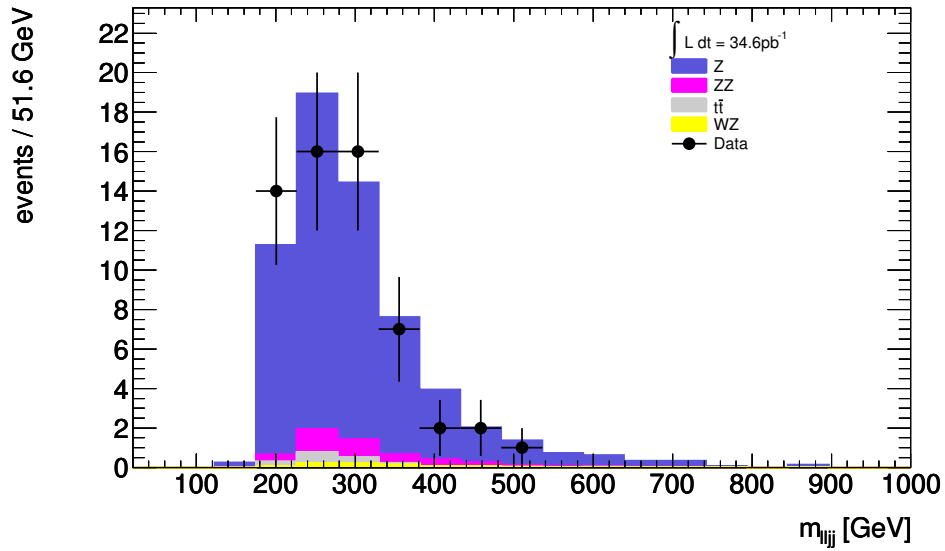
	No b-tag		With b-tag	
	Low mass	High mass	Low mass	High mass
Z	246	56.5	0.3	0.1
$t\bar{t}$	2.4	1.3	0.3	0.2
ZZ	15.7	3.6	0.4	0.1
WZ	2.7	0.8	0.0	0.0
QCD	5.9	1.3	-	-
Total MC	267	62.2	1.01	0.38
Data	227	58	2	1

Table 6.2: Predicted signal event yields in 34.6 pb^{-1} .

m_H [GeV]	No b-tag		With b-tag	
	Low mass	High mass	Low mass	High mass
200	5.0×10^{-1}	4.8×10^{-2}	1.2×10^{-2}	7.1×10^{-4}
300	3.5×10^{-1}	2.6×10^{-1}	1.4×10^{-2}	1.2×10^{-2}
400	2.2×10^{-1}	2.0×10^{-1}	1.1×10^{-2}	1.0×10^{-2}
500	7.2×10^{-2}	6.7×10^{-2}	4.0×10^{-3}	3.9×10^{-3}
600	2.4×10^{-2}	2.2×10^{-2}	1.2×10^{-3}	1.1×10^{-3}

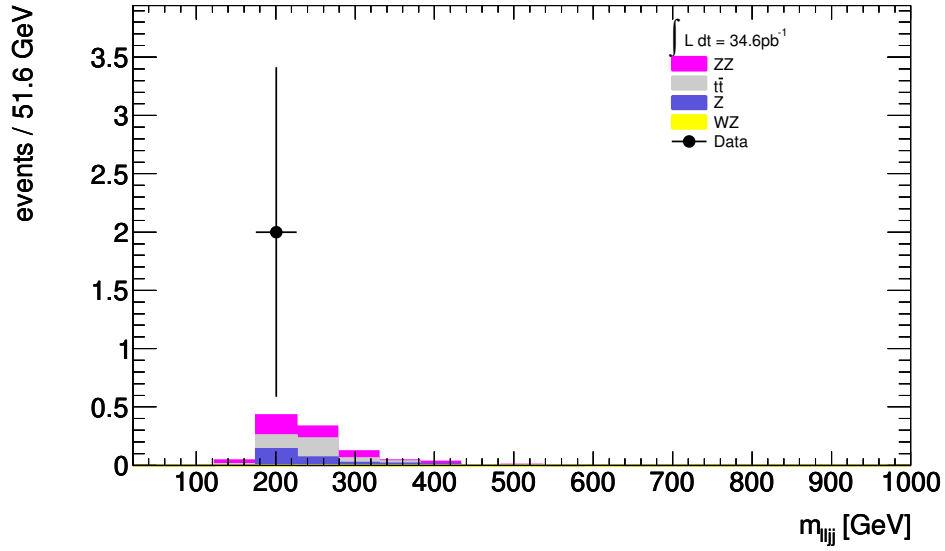


(a) low mass selection

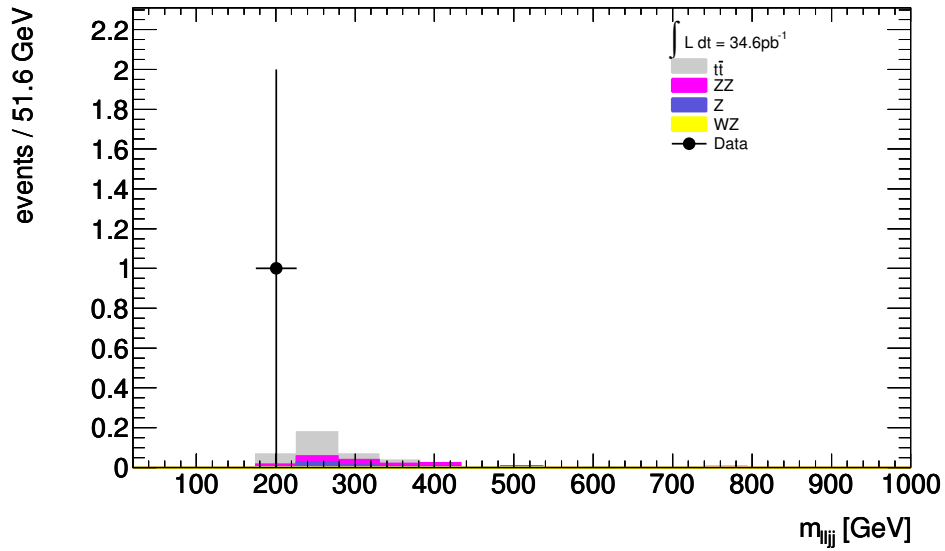


(b) high mass selection

Figure 6.11: m_{ljj} distribution with all analysis cuts excluding b -tagging.



(a) low mass selection



(b) high mass selection

Figure 6.12: m_{lljj} distribution with all analysis cuts including b -tagging.

6.8 Conclusions

Initial investigations of the 2010 LHC run were presented. Control regions were defined to extract Z , $t\bar{t}$ and QCD enhanced samples from the untagged $lljj$ dataset. Similar techniques may be used on the b -tagged dataset when larger statistics are available. In general there is good agreement between data and Monte Carlo simulation. After applying the full b -tagged event selection 1 (2) event(s) pass the high (low) mass selection. This is consistent with the Standard Model expectation. Much more luminosity is required to make useful statements about the existence or exclusion of a $H \rightarrow llbb$ excess in this channel.

Chapter 7

Level-1 Calorimeter Trigger

The Level-1 Calorimeter Trigger (L1Calo) is responsible for identifying high p_T electrons, photons, τ -leptons and jets. It also provides the total E_T and missing E_T triggers [32]. The multiplicities of items passing the set thresholds are passed to the CTP which applies pre-scales and makes the final trigger decision.

There are three main systems that make up L1Calo: the Preprocessor, the Cluster Processor and the Jet Processor. The system architecture is summarised in figure 7.1.

7.1 Preprocessor

The ATLAS calorimeters have in total $\sim 200,000$ channels. This is too many to be processed by the Level-1 Trigger. Instead, analogue signals are summed transversely and in depth within each calorimeter subsystem into around 7200, approximately projective, trigger towers. The towers are mostly of size

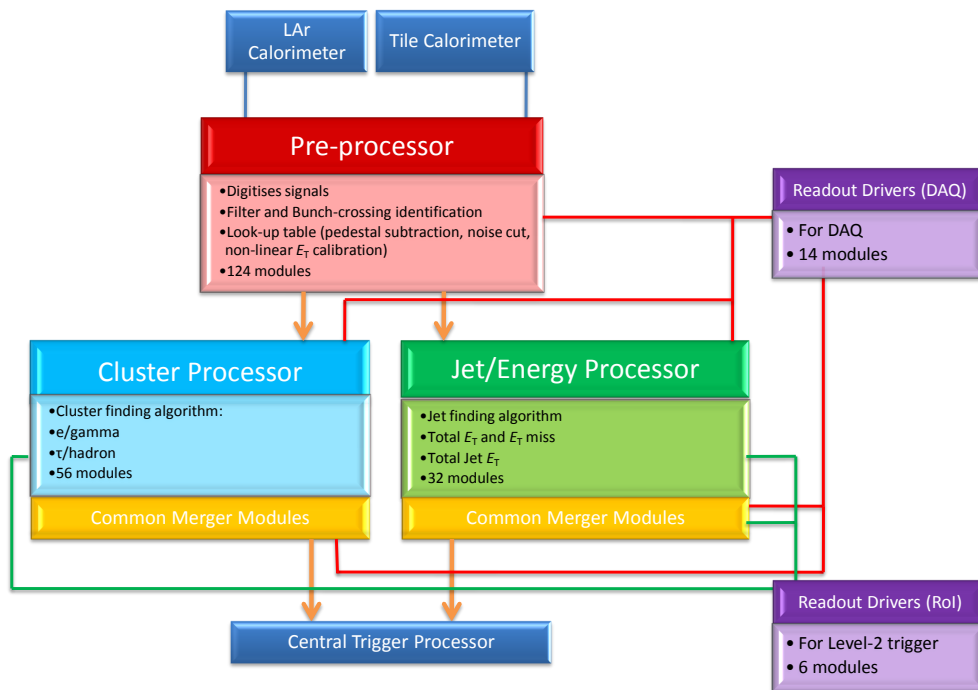


Figure 7.1: A diagram of the L1Calo system architecture. Signals from the calorimeters enter the Preprocessors where they are digitised and calibrated. E_T counts are sent in parallel to the Jet Processor and Cluster Processor systems where the trigger algorithms are run. Results are merged in the CMMs and object multiplicities are transmitted to the CTP. Data and RoIs from each subsystem are read-out, via RODs, for monitoring and for the Level-2 Trigger.

$\eta \times \phi \sim 0.1 \times 0.1$ and are shown in Figure 7.2. Analogue gains are applied to calibrate the signals to a common transverse energy scale before they enter the Preprocessor system.

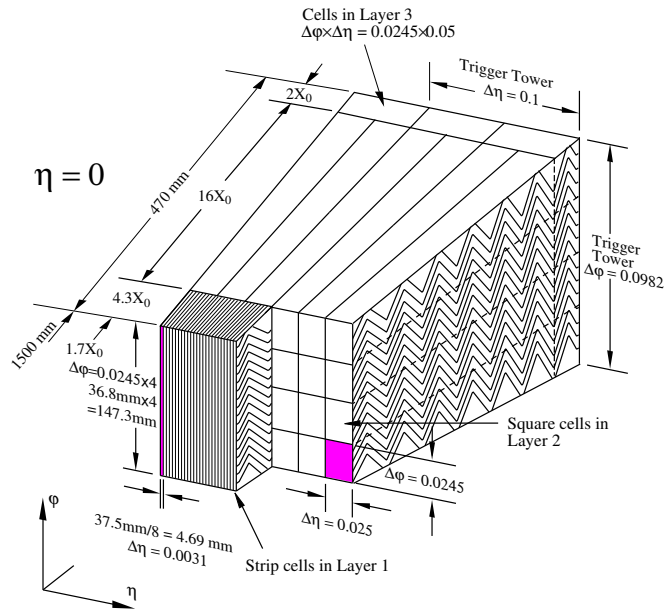
The Preprocessor module performs the fine-timing alignment and digitisation of the signals. Signals are digitised with 10-bit precision at the LHC 40 MHz bunch-crossing rate. Input delays are applied to compensate for different cable lengths and time-of-flight to synchronise the input signals to within one bunch-crossing. Fine timing is set by adjusting the flash-ADC digitisation strobe relative to the input signals in 1 ns steps.

Signals are assigned to a bunch-crossing (described in section 7.2) and the final energy calibration and pedestal subtraction is done with a Look-up Table (LUT). The LUT outputs an 8-bit word representing the E_T in GeV of the signal. The LUT also applies noise thresholds and can act as a mask for bad channels (by setting the entire LUT output to zero).

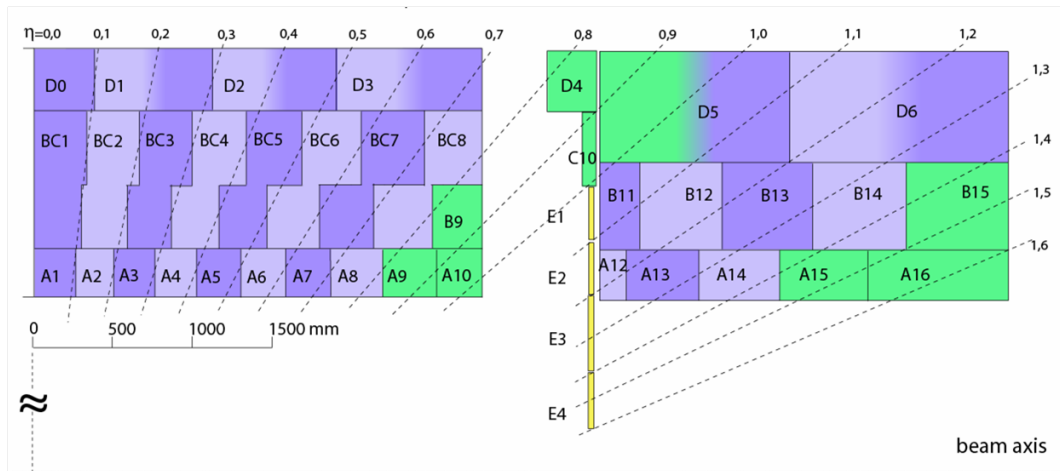
Finally, the signals are prepared for transport to the Cluster Processor and Jet Processor systems. For the Jet Processor, towers are summed into even lower granularity Jet Elements of 2×2 towers in $\eta \times \phi$.

7.2 Bunch-crossing Identification

Trigger tower signals are typically 5 to 6 bunch-crossings wide as the pulses are shaped in the detector front-end electronics. This raises the problem of assigning a pulse to a particular bunch-crossing. The natural choice to make is to choose the peak of the pulse. However, for small signals, noise can distort the shape of the pulse and cause the wrong bunch-crossing to be



(a) Liquid Argon



(b) Tile

Figure 7.2: Signals from calorimeter cells are summed into lower granularity trigger towers. (a) shows a trigger tower in the Liquid Argon calorimeter at $\eta = 0$. The LAr calorimeter granularity varies through the detector and a trigger tower can be formed from up to sixty calorimeter cells. (b) shows the formation of trigger towers in the Tile Barrel (left) and Tile Extended Barrel (right) calorimeters. Most towers are formed from the sum of signals from five photomultipliers. No summation of cells is performed across the boundary between Tile calorimeters.

chosen. Conversely, for large saturated signals there is no clear peak. There are two main Bunch-crossing Identification (BCID) methods, one designed for small signals and one designed for saturated pulses.

For non-saturated pulses (below ~ 250 GeV) the signal is passed through a digital Finite Impulse Response (FIR) filter. The input ADC samples are pipelined. Every bunch-crossing, 5 ADC data samples, adjacent in time, are multiplied by a set of coefficients and the results are summed. The output from the filter is then passed through a peak finder which compares the result with those from the preceding and following bunch-crossings. If the filter output is a local maximum the BCID is passed. If the BCID test is failed the output from the LUT is inhibited.

The filter coefficients can be set individually for all towers. Chapter 8 describes the study to find the best set of filter coefficients which were implemented during the 2010 LHC proton-proton run.

For very high energy pulses, both the analogue electronics and the ADC data can become saturated and the digital filter ceases to effectively identify the correct bunch-crossing. For saturated pulses two samples on the leading edge of the pulse are compared to a high and a low threshold [33]. Since the rise times of the pulses are known, the position of the peak had it not been saturated can be extrapolated. If a saturated pulse is detected, the LUT E_T result is not used. Instead, a fixed value is output (by default the maximum possible 8-bit value, 255).

7.3 Cluster Processor

The Cluster Processor system is responsible for identifying electrons/photons, and τ /hadrons. The algorithm to do this can be represented as a sliding window of 4×4 trigger towers, shown in Figure 7.3 [34]. The Cluster Processor system only operates over the range $|\eta| < 2.5$ as that is the range of the tracking and high granularity calorimetry.

The e.m. cluster energy is defined as the highest of the 2×1 sums in the electromagnetic layer. The hadronic cluster energy is defined as the sum of the e.m. cluster and the 4 towers forming the hadronic inner core. In addition isolation rings in the e.m. and hadronic layer are formed by summing over

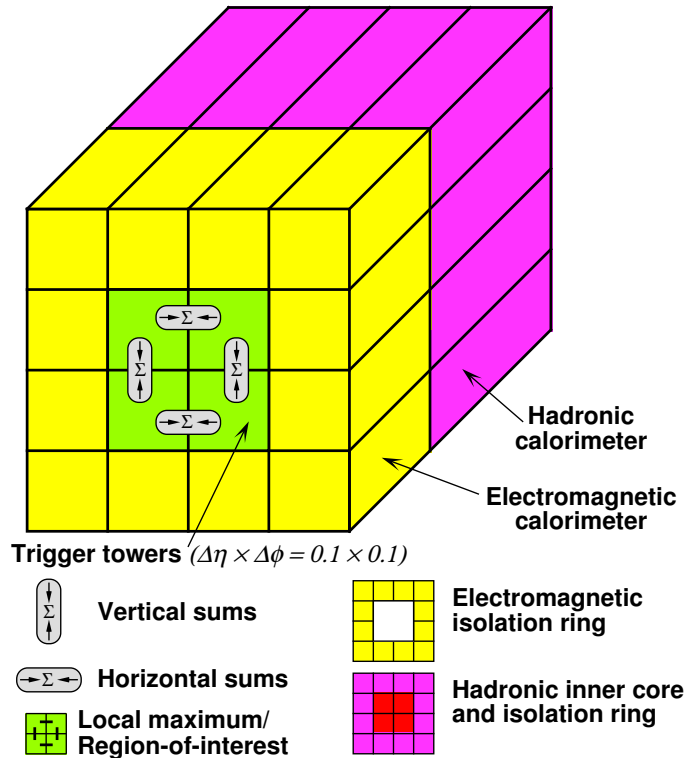


Figure 7.3: The “sliding” window of the Cluster Processor trigger algorithm. The details of the algorithm are described in the text.

the surrounding 12 towers. The RoI cluster energy is defined as the E_T sum over both calorimeter layers of the 2×2 central towers.

A candidate trigger object must pass all of the following criteria:

- The e.m. cluster (for e/γ) or hadronic cluster (for τ /hadron) must have E_T greater than the set threshold.
- The total E_T in each of the isolation rings must be less than their respective thresholds.
- For e/γ only, the E_T in the hadronic core must be less than a threshold.
- The RoI cluster must be a local E_T maximum i.e. its E_T is greater than (or greater than or equal to) ¹ the RoI cluster E_T of adjacent overlapping windows. This prevents double counting of objects.

Sixteen sets of thresholds can be set for the Cluster Processor system. The multiplicities of each trigger object are summed in the CMMs and sent to the CTP where the L1A is generated. Upon L1A, data are read-out through the RODs for data quality and monitoring. In addition RoIs are sent to the Level-2 Trigger to seed algorithms.

The Cluster Processor system consists of 4 crates, each handling a quadrant in ϕ . A crate contains 14 Cluster Processor Modules (CPMs) each processing a slice in η . Because of the overlapping windows of the algorithm, data must be duplicated in different CPMs and different crates. To reduce the number of links between the Preprocessor and the Cluster and Jet Processor

¹As digital values can be equal, the local maximum test uses different conditions for overlapping windows. For the four overlapping windows in the $+\eta$ and $+\phi$ directions a ‘greater than’ condition is used. For the four overlapping windows in the $-\eta$ and $-\phi$ directions a ‘greater than or equal to’ condition is used.

systems, a custom backplane is installed in the Processor crates. Where data must be shared between modules within the same crate they are transmitted via the backplane. Where data must be shared between crates they are duplicated at the Preprocessor and sent to both crates.

7.4 Jet/Energy Processor

The Jet Processor also implements a sliding window algorithm. It is based on Jet Elements which are 2×2 towers summed in depth over both calorimeters. Windows of 2×2 , 3×3 and 4×4 Jet Elements are formed, as shown in Figure 7.4. The total E_T within the window must be greater than the threshold. A total of 8 sets of thresholds can be set with each set containing an E_T threshold and a window size. As with the Cluster Processor system, double-counting is prevented by demanding that the RoI cluster (a 2×2 set of Jet Elements within the window) is a local maximum.

Additionally the Jet Processor system calculates the scalar sum of E_T for the total energy trigger and the vector sum of E_T for the total missing

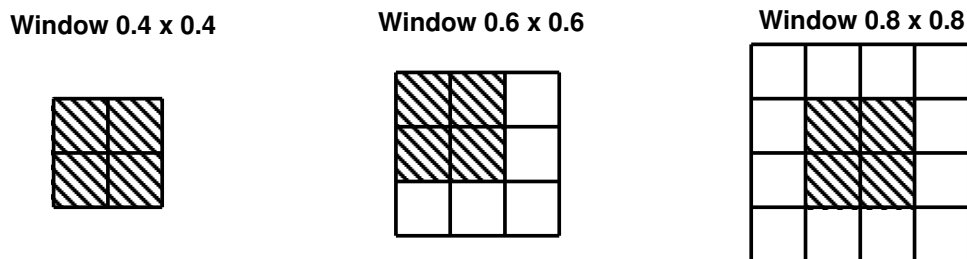


Figure 7.4: The jet windows used by the jet-finding algorithm. Each cell represents a Jet Element. The shaded cells correspond to the RoI cluster required to be a local maximum to prevent double-counting. In the 0.6×0.6 case, the RoI cluster can be placed in any one of the four corners of the window.

energy trigger. Finally a total jet energy trigger is formed by estimating the total energy in jets from the multiplicities of each threshold passed.

The Jet Processor system consists of 2 crates each with 16 Jet Energy Modules (JEMs). Results are merged in the CMMs and jet object multiplicities and sum E_T and missing E_T thresholds passed are transmitted to the CTP where the Level-1 trigger decision is made.

Chapter 8

Digital Filter for the Level-1 Calorimeter Trigger

L1Calo, described in detail in chapter 7, is a hardware-based calorimeter trigger and provides the majority of the inputs to the ATLAS Level-1 trigger decision. It is a pipelined processor system, with a new set of inputs being evaluated every 25 ns. Analogue signals from the calorimeters are first digitized at the 40 MHz LHC bunch-crossing frequency, before being passed to a digital Finite Impulse Response (FIR) filter. Due to latency and chip real-estate constraints, only a simple 5-element filter with limited precision can be used. Nevertheless, this filter achieves a significant reduction in noise, along with improving the bunch-crossing assignment and energy resolution for small signals.

In this chapter, the methods used to determine the best filter coefficients for each detector element are presented. The performance of these filters is investigated with commissioning data and cross-checks of the calibration

with initial beam data from ATLAS are shown.

8.1 Digital Filter Implementation

Due to signal shaping in the analogue electronics chain, as well as the detector response time, trigger tower pulses are typically much longer than a single bunch crossing. Liquid Argon (LAr) trigger towers have bi-polar pulses that are typically five to six bunch-crossings wide, with a typical rise time of 2 bunch-crossings. The bi-polar shaping is designed to ensure that the mean baseline, or pedestal, is insensitive to pile-up. Conversely, Tile calorimeters are not expected to suffer from pile-up as much, so trigger towers have uni-polar pulses with similar widths to the LAr pulses.

The assignment of the energy deposits to the correct bunch-crossing is referred to as Bunch-crossing Identification (BCID). The energy resolution has to be of the order of 3% of the calorimeter energy (at the high energy limit) in order to provide trigger thresholds with good precision, and the Level-1 Trigger must be robust against calorimeter noise to prevent flooding of the higher-level trigger and data acquisition system with many useless events. In L1Calo these functions rely on the digital filter implemented in the Preprocessor.

The implementation in the Preprocessor is shown in Figure 8.1. Due to both time and chip size limitations, only a simplified filter can be used, limited to five elements, each of which has only four bit precision. This simplification reduces the time and number of logic elements needed to perform the filter calculation, but still gives enough freedom to produce a filter which

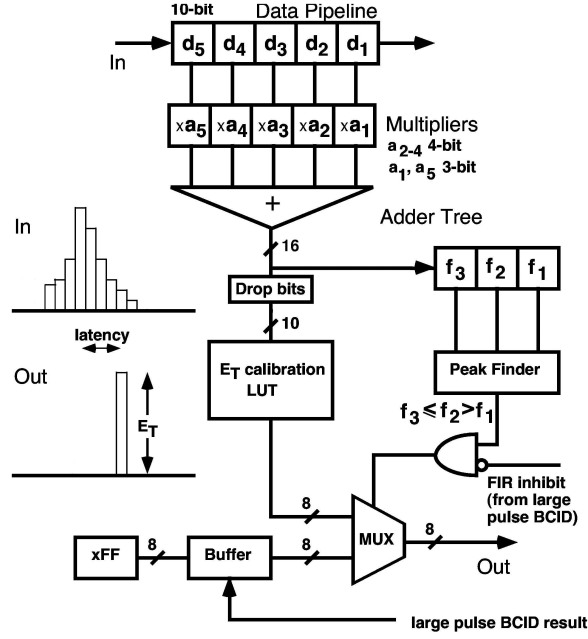


Figure 8.1: A diagram showing the implementation of the digital filter and peak-finder in the Preprocessor.

is tailored for the typical calorimeter signal shape and noise.

The filter calculates the convolution of the input ADC data samples with the filter coefficients. Hence, the filter output, f_{output} is given by,

$$f_{\text{output}} = \sum_{i=1}^5 a_i d_i, \quad (8.1)$$

where a_i are the filter coefficients and d_i are the ADC data samples. Assuming that the pulse shape is independent of energy and that the pedestal is constant, then equation 8.1 can be broken down into its signal, noise and pedestal components,

$$f_{\text{output}} = E \sum_{i=1}^5 a_i x_i + \sum_{i=1}^5 a_i b_i + p \sum_{i=1}^5 a_i, \quad (8.2)$$

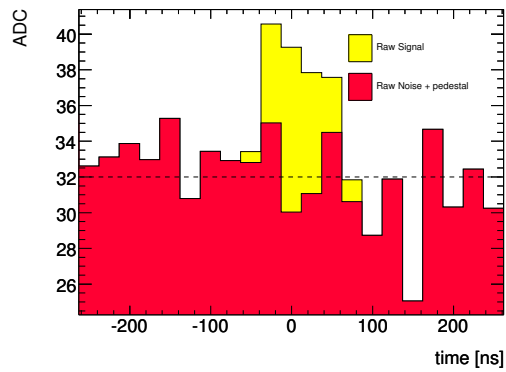
where E is the transverse energy of the pulse, x_i describe the normalised signal pulse shape in the absence of noise, b_i are the background noise components of the pulse and p is the pedestal.

The sixteen bit filter output is passed through a peak finder, which compares the filter output with the outputs from the preceding and following bunch-crossings. The filter output must be greater than the preceding value and greater than or equal to the following value to pass the non-saturated BCID requirement.

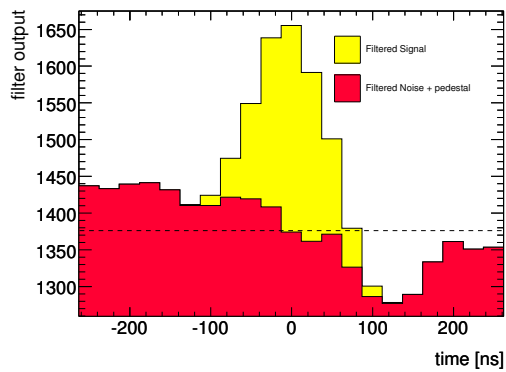
In parallel, the sixteen bit filter output is fed into a ten bit Look-up Table (LUT). This is achieved by dropping a combination of least-significant and most-significant bits. The drop-bits procedure is described in detail in section 8.2. The LUT simultaneously applies pedestal subtraction, noise cuts and the final transverse energy calibration. The LUT also provides the mechanism for disabling channels, which is done by setting the entire LUT range to output 0. The LUT outputs an eight bit number which represents the final calibrated E_T for that tower. Ideally, the system should be calibrated such that one LUT output count corresponds to ~ 1 GeV, and one LUT input count corresponds to ~ 250 MeV.

8.2 Choice of Filter Coefficients

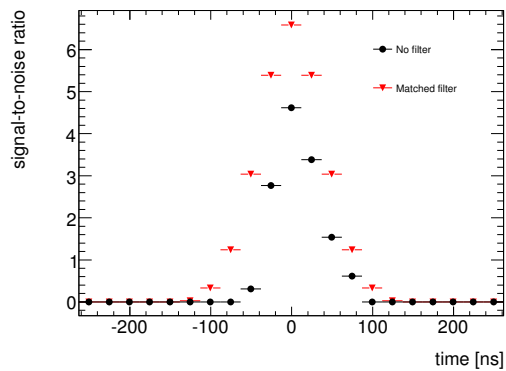
For Gaussian white noise, the optimal choice of filter coefficients is the matched filter [35]. A matched filter has coefficients that are chosen to be proportional to the pulse height at each sample. Figure 8.2 demonstrates the effect of a matched filter on a simulated pulse. In this example, noise



(a) Raw pulse



(b) Filtered pulse



(c) Signal-to-noise ratio

Figure 8.2: A simulated pulse with a 2 GeV signal peaking at 0 ns and $\sigma = 0.5$ GeV Gaussian white noise. (a) and (b) show the pulse before and after applying a matched filter, respectively. The dashed line indicates the corresponding pedestal value. (c) shows the ratio of signal height to noise RMS with and without the filter.

has distorted the shape of the pulse so that the peak of the unfiltered pulse, figure 8.2(a), is one bunch-crossing early. The filtered pulse, 8.2(b), provides a much clearer signal above background and, in this example, the peak is reconstructed in the correct bunch-crossing. Figure 8.2(c) shows the ratio of signal height to noise RMS. The effect of the filter is to improve the signal significance.

In theory, the best performance is achieved by using a filter matched individually to each tower's signal pulse shape. However, there are several practical limitations. Firstly, pulse shapes are not the same for all trigger towers. Relative timing differences between calorimeter cells and different cable lengths as well as different calorimetry and front-end electronics result in different pulse shapes. There are 7,168 towers, each with 5 filter coefficients, which gives 35,840 free parameters. Filter coefficients can be set individually for each tower at the cost of increased overall complexity of the system.

Secondly, the filter coefficients have limited bit precision: four bits unsigned for the central coefficients and four bits signed for the first and final coefficients. To achieve the best match to the pulse shape, the central coefficient should be chosen to be 15. However, there is an additional complication: the filter's sixteen bit output must be mapped to the ten bit input to the look-up table. This is done by dropping a combination of least significant and most significant bits. In practice, some of the most-significant bits can only ever be used by saturated pulses. A constant value is output for all saturated pulses, and so these bits do not add to the precision of the energy measurement. Therefore, bits that are used only for saturated pulses can be dropped with no loss of precision. In the case that the filter output does overflow ten

bits, the maximum value is set. However, usually some least significant bits must also be dropped to reduce the filter output to ten bits, which results in an unavoidable loss of precision. The number of least-significant bits dropped is chosen so that non-saturated pulses produce a filter output that is within the LUT range after the drop-bits operation.

The best LUT precision is achieved by choosing coefficients such that the entire LUT input range is used for non-saturated pulses only. The LUT precision depends on the filter coefficients, pulse shape and the number of least-significant bits dropped, n ,

$$\Delta E_{\text{LUT}} = \frac{2^n}{\sum_{i=1}^5 a_i x_i}, \quad (8.3)$$

where ΔE_{LUT} is the step-size in energy between LUT input counts, or equivalently, the energy corresponding to 1 LUT input count.

When usage of the LUT range is optimised this gives a precision of ~ 250 MeV. With the wrong choice of filter coefficients and drop-bits settings, it is possible to leave up to half of the LUT range unused, which would result in a precision of ~ 500 MeV. The LUT precision is particularly important for the measurement of small pulses as it defines the precision with which the pedestal subtraction and noise cuts can be applied.

In general, in the digital system, it is not possible to simultaneously optimize the LUT range usage and the precision with which the filter may be matched to the pulse shape.

8.3 Measurement of Pulse Shapes

The Preprocessor digitises signals at the LHC bunch-crossing rate. To reconstruct the pulse shape with better than bunch-crossing precision, a timing scan was performed. Calibration pulses were injected into the calorimeter systems while Preprocessor FADC fine-timing was repeatedly shifted by 1 ns. This allowed the pulse shape to be reconstructed with nanosecond precision. The calibration pulses were designed to produce signal shapes approximately equal to those expected from collisions.

Typical trigger tower pulse shapes from each calorimeter region are shown in Figure 8.3. Pulse shapes vary significantly through the detector. Pulses in the hadronic layer, Figures 8.3(d-f), are narrower than in the e.m. layer, Figures 8.3(a-c). In the Forward Calorimeter (FCal), where the LAr gap is much smaller, pulses are extremely short; only ~ 3 bunch-crossings in the example pulse, Figure 8.3(g). Additionally, in the FCal a strong reflection can be seen following the main pulse. This is a feature of the calibration pulses and is not present in physics pulses.

In general, no attempt is made to form trigger towers across the boundaries of calorimeters. There is one exception, the overlap region between the EM Barrel and Electro-magnetic End-cap (EMEC). This corresponds to trigger towers in the region $1.4 < |\eta| < 1.5$. Figure 8.3(c) shows an example pulse shape in this LAr overlap region. The pulse shapes in this region are distorted. The signals from each calorimeter partition are not merged on detector, but in receiver stations immediately upstream from L1Calo. In order to align the signals correctly in time, cables must be cut precisely to length.

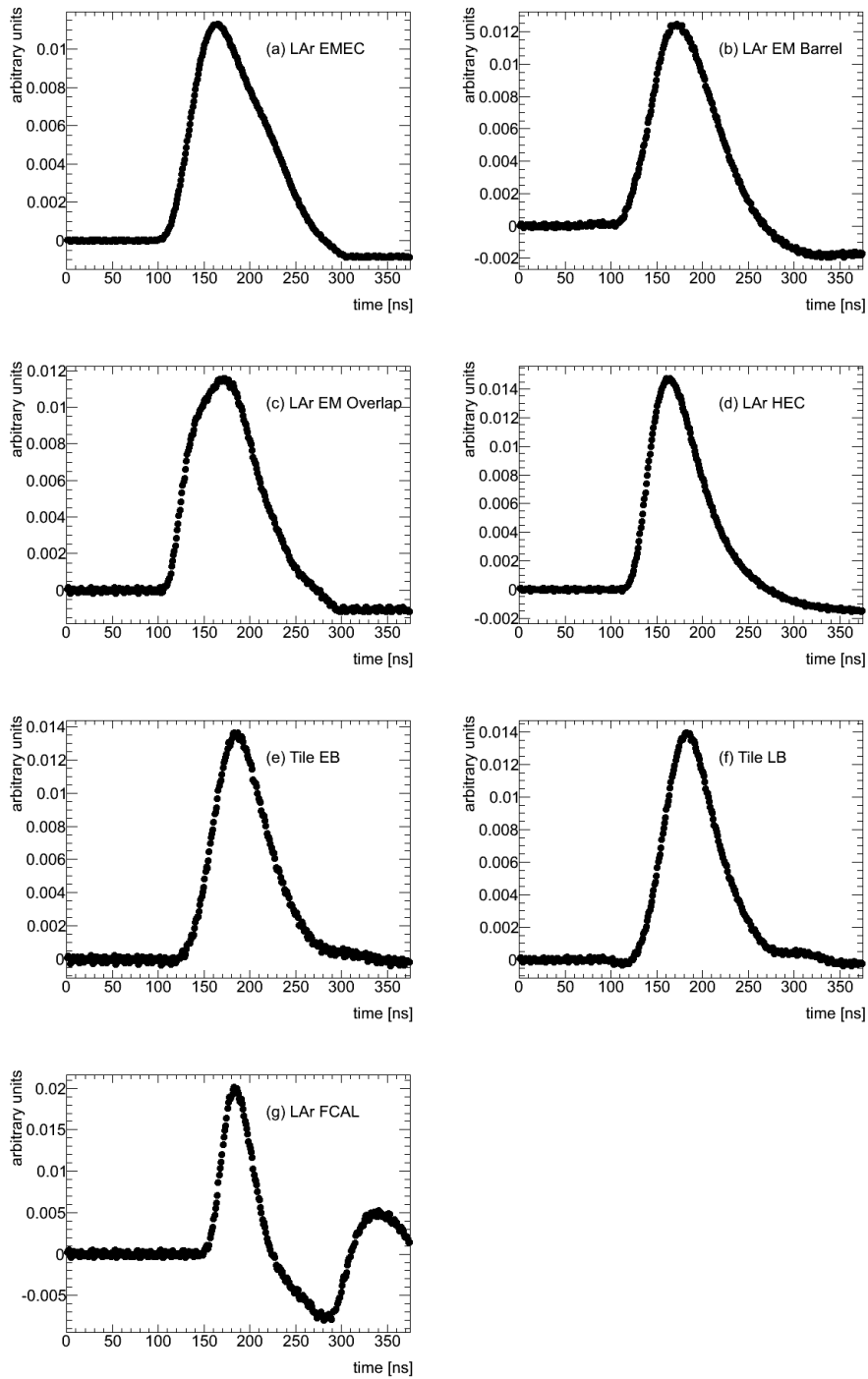


Figure 8.3: Typical trigger tower pulse shapes reconstructed from timing scans as explained in section 8.3. Example pulses are shown for each of the calorimeter partitions.

This was only possible after sufficient data had been taken to precisely determine the timings from real physics pulses. This was not done until after the 2010 LHC run. As the trigger towers in this region were not completely commissioned, they were excluded from the following studies.

Figure 8.4 shows the full-width at half-maximum of pulses reconstructed from a timing scan. Despite the different technologies used in the hadronic layer, a combination of Tile scintillator and LAr ionisation calorimetry, pulses are consistently narrower in the hadronic layer than in the e.m. layer. For this reason, when investigating the performance of filters optimised for certain detector regions, it is more appropriate to make a distinction between the e.m. and hadronic layers, than between Tile and LAr calorimeters. Pulses in the forward calorimeters, $|\eta| > 3.2$, are significantly narrower than elsewhere in the calorimeter, and therefore must also be treated differently to other regions.

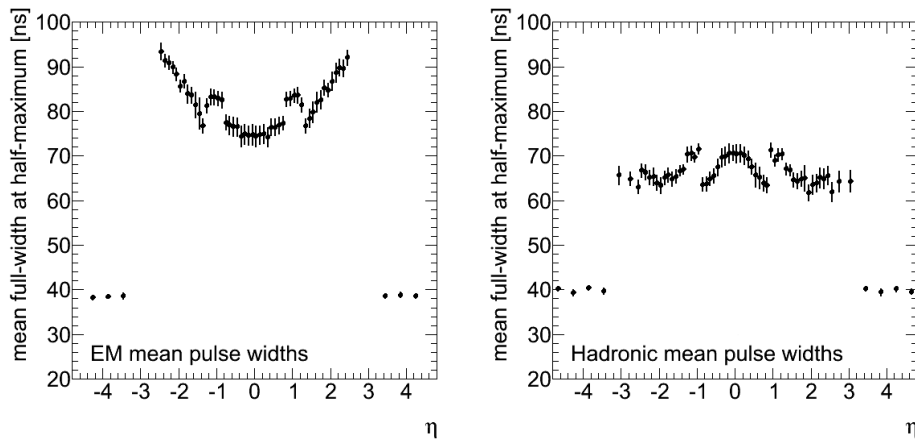


Figure 8.4: The mean full-width-half-maximum of pulses reconstructed from a timing scan versus η shown for the e.m. layer (left) and for the hadronic (right). The bars on the data points show the standard deviation of widths in that η bin.

8.4 Digital Filter Performance

The filter performance can be accurately simulated using a combination of calibration pulses and noise data. The pulse shapes, as measured from timing scans, were sampled every 25 ns, centred around the peak of the pulse. These digitised pulses were scaled to specific energies and superimposed on to real detector noise. Noise events were selected with a random trigger during runs when there was no beam. The resulting pulses were used as the input to a simulation of the Preprocessor filter and BCID mechanism, in order to test the performance of different filter configurations. As the filter implementation is entirely digital, its behaviour can be simulated exactly.

The performances of the following filters have been studied:

1. The **matched** filter, where the filter was matched individually to each tower's reconstructed pulse shape. The central coefficient was fixed to 15. The other coefficients were set in proportion to the pulse height in the corresponding sample. As coefficients must take integer values, the coefficients were rounded to the nearest integer.
2. A **common** filter, applied across an entire calorimeter layer. The coefficients used were matched to the median width pulse in the range $|\eta| < 0.1$. Low η towers were selected as this is where the detector noise is greatest. Detector noise is reduced as η increases due to gains applied to convert signals to E_T . The sets of coefficients used are shown in Table 8.1.
3. The **pass-through** filter, where the coefficients for all towers were set

to (0,0,1,0,0) and no least-significant bits were dropped. The input pulse is equal to the output pulse and hence this setting is equivalent to using no filter.

There are three main measures of performance to compare different sets of filter coefficients: BCID efficiency, noise rejection and energy resolution. Performance results are only shown for towers in the LAr as these towers generally have wider pulses so show greater difference in performance with and without a filter. Absolute performance varies through the calorimeters but the relative performance between the tested filters is consistent.

BCID efficiency is the efficiency for assigning a pulse to the correct bunch-crossing. It is defined as,

$$\epsilon = \frac{\text{N}^\circ \text{ simulated pulses passing the BCID requirement in the correct BC}}{\text{Total N}^\circ \text{ simulated pulses}}. \quad (8.4)$$

The BCID efficiency for a single tower is shown in Figure 8.5. There is a clear improvement in using the matched or common filters over the pass-through. However, there is little difference between the matched and common filters.

Table 8.1: Common filter coefficients.

Calorimeter Region	Filter Coefficients	# bits dropped
e.m. calorimeters	1,8,13,10,7	5
hadronic calorimeters	1,9,15,11,5	5
forward calorimeters	0,2,13,5,0	4

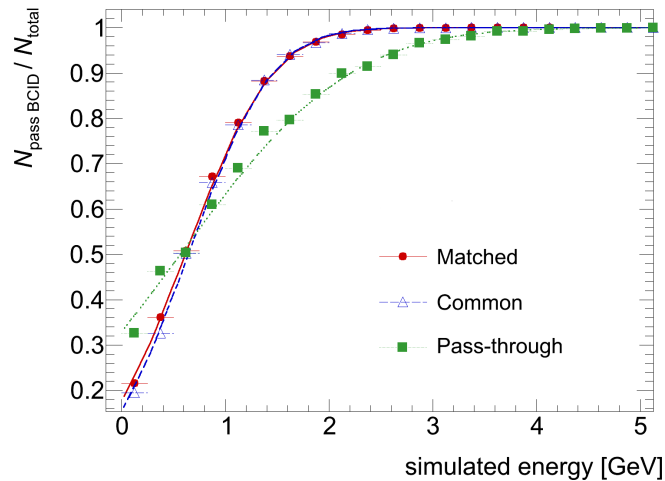


Figure 8.5: BCID efficiency turn-on curve comparing Matched, Common and Pass-through filters for one example trigger tower in the LAr EM barrel. The fit is given by equation 8.5.

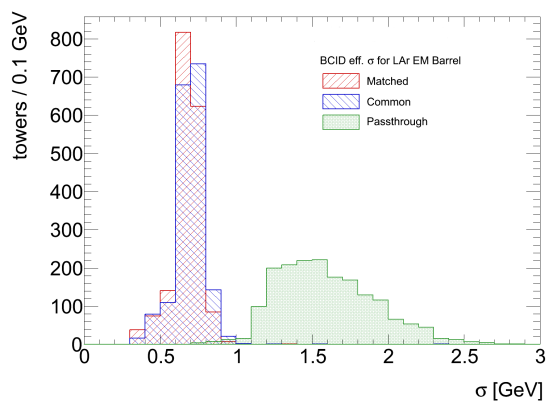


Figure 8.6: BCID efficiency turn-on curve σ , as defined in equation 8.5, for all towers in the LAr EM barrel. Results for Matched, Common and Pass-through filters are shown.

The BCID efficiency turn-on curve can be modelled with the equation,

$$\epsilon(E) = \frac{1}{2} \left(1 + \operatorname{erf} \left(\frac{x - \mu}{\sqrt{2}\sigma} \right) \right), \quad (8.5)$$

where ϵ is the BCID efficiency, μ describes the turn-on transverse energy and σ describes the width of the turn-on curve. Equation 8.5 was fitted to the BCID efficiency curves for all towers. The parameter, σ , provides a useful metric with which to compare the performance of different filters. This is shown for all towers in the e.m. barrel region in Figure 8.6. These results are consistent with those shown in the single-tower Figure 8.5.

If noise fluctuates upwards there is a chance that it will produce a non-zero output from the LUT. By using a filter that includes multiple time slices, there is a tendency for the noise to cancel out, and hence a reduced noise rate. Figure 8.7 shows the probability distribution of noise producing a filter

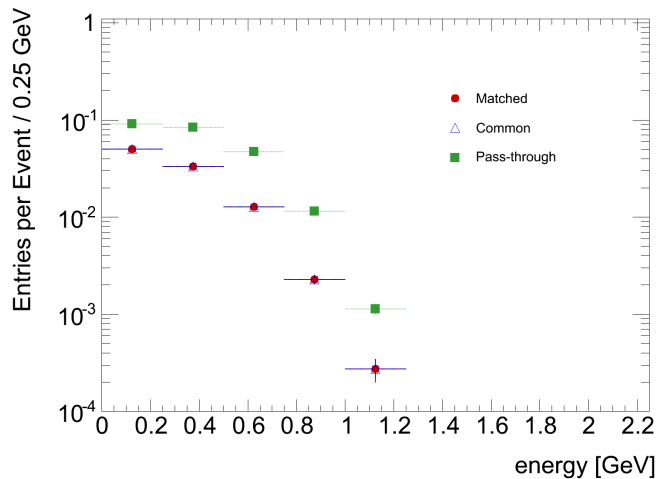


Figure 8.7: Probability distribution for noise producing a filter output that passes BCID requirements versus the corresponding E_T for one example tower. Matched, Common and Pass-through filters are shown.

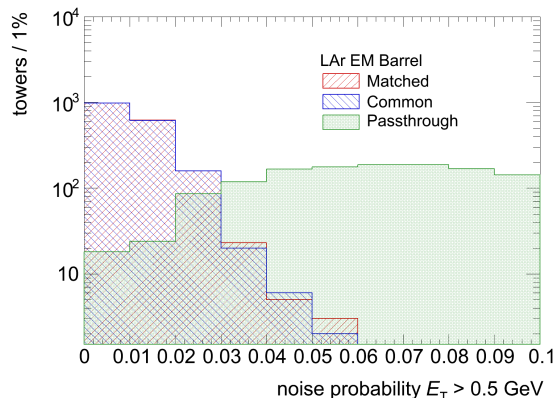


Figure 8.8: The probability of a tower’s noise producing a filter output with an E_T greater than 0.5 GeV was calculated. The histogram is filled with these probabilities, with an entry for each trigger tower in the LAr EM barrel. Note that this does not equal the probability that a tower would produce a non-zero LUT output that is propagated to the processor systems as noise cuts are also applied.

output with a given E_T , for a single tower. Only events passing the BCID criteria are included. There is a clear improvement in using the matched or common filters over the pass-through. However, there is no significant difference between the Matched and Common filters. The distribution shown in Figure 8.7 was integrated from 0.5 GeV to infinity. This gives an estimate of the probability that noise in that tower would produce a filter output greater than 0.5 GeV. This represents the worst-case scenario, as this corresponds to all noise pulses that could be rounded up to 1 GeV in the LUT table and produce a non-zero output. In practice, noise cuts are applied that drastically reduce the probability of noise producing a non-zero LUT output that is propagated into the processor system. Nevertheless, this provides a useful metric with which to compare the performance of filters. Figure 8.8 shows a histogram filled with the calculated probabilities for all towers in

the e.m. barrel region. The results for many towers, shown in Figure 8.8, are consistent with those for a single tower in Figure 8.7.

Finally, the filter affects the contribution of detector noise to the energy measurement. Figure 8.9 shows the difference between the E_T measured by L1Calo and the simulated E_T . The distribution is narrower when using the matched or common filters compared to the pass-through. However, there is no significant difference between the resolutions of the Matched and Common filters. A Gaussian was fitted to the distributions and the fit widths of all towers in the e.m. barrel region are shown in Figure 8.10. These results are consistent with those for a single tower in Figure 8.9.

For all three measures of performance, there is no significant advantage to matching the filter on a tower-by-tower basis. Equivalent performance can be achieved with a common filter applied across an entire calorimeter layer. Therefore, the common filter strategy was adopted for early LHC running.

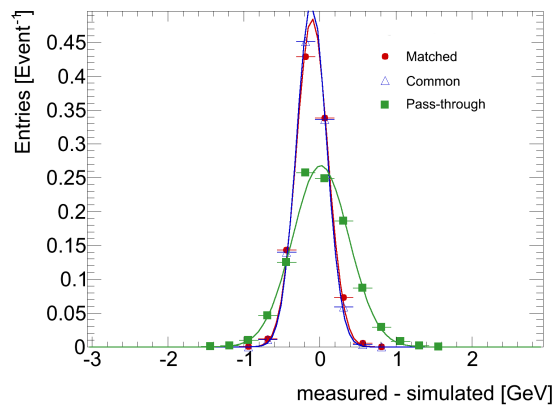


Figure 8.9: Difference between simulated E_T and corresponding E_T of the filter output for an individual trigger tower. The Matched, Common and Pass-through filters are shown. A Gaussian is fitted to each distribution.

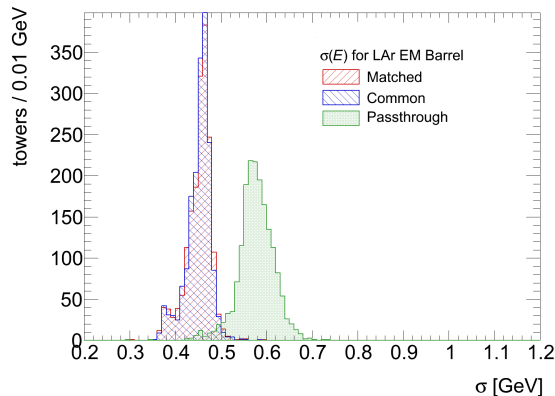


Figure 8.10: The E_T resolution for all channels in the LAr EM barrel as determined from a Gaussian fit to the distributions shown in Figure 8.9.

8.5 Saturation Energies in the Preprocessor

There are two places within the Preprocessor system where saturation can occur. Firstly, the input analogue pulses are digitised with ten bit precision. The ADC saturation energy is simply,

$$E_{\text{sat}}^{(\text{ADC})} = 2^{10} - p, \quad (8.6)$$

where p is the pedestal value. There is a nominal pedestal of 32 counts. Analogue gains are applied to calibrate the input scale to 4 counts per GeV of E_T . Hence the ADC saturates at an E_T of approximately 248 GeV.

Secondly, the input to the LUT is only ten bits wide. In general, the energy scales, before and after applying the filter are different. Consequently, the corresponding saturation energies are different. The LUT saturation energy is given by,

$$E_{\text{sat}}^{(\text{LUT})} = \frac{E_{\text{sat}}^{(\text{ADC})} \sum_i a_i x_i + p \sum_i a_i}{2^n}. \quad (8.7)$$

To achieve the best precision for matching the pulse shapes the filter must have a central coefficient value of 15. However, by rescaling the filter to different peak heights, it is possible to control the LUT saturation energy. The ratio of $E_{\text{sat}}^{(\text{ADC})}$ to $E_{\text{sat}}^{(\text{LUT})}$ indicates the fraction of the LUT range that is used for non-saturated pulses. Ideally this ratio should be equal to 1: the LUT can describe the same range of pulse energies as the ADC, with no loss of precision. Figure 8.11 shows this ratio for 3 different scalings of the Common e.m. filter.

When the e.m. filter is scaled to a peak of 15, the ADC saturation energy is greater than the LUT saturation energy. In this case, the LUT cannot output the full range of pulse energies that can be described by the raw ADC pulse. When the e.m. filter is scaled to a peak of 11, the ADC saturation energy is

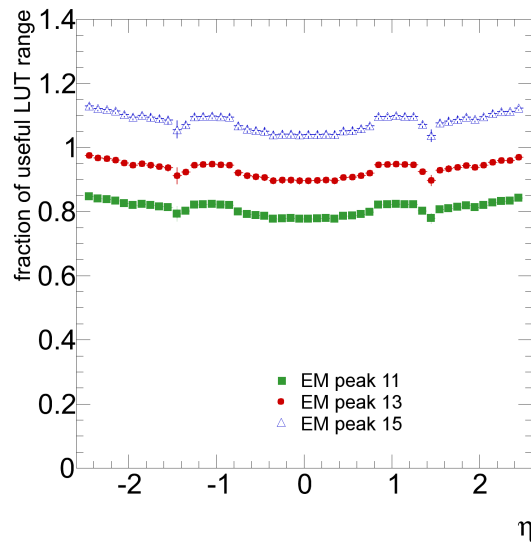


Figure 8.11: The fraction of the LUT range that is used by non-saturated pulses in the e.m. layer. Common-type filters are shown scaled to peak coefficients of 15, 13 and 11. The meaning of these values are explained in the text.

less than the LUT saturation energy. In this case, up to 20% of the LUTs dynamic range is wasted on saturated pulses. This reduces the granularity of LUT counts and so reduces the precision with which pedestal subtraction and noise cuts can be applied. By scaling the e.m. filter to a peak of 13, most of the LUT range is used effectively. Analysis of these scaled filters showed no significant difference in the performance of BCID, noise suppression or energy measurement.

Importantly, Figure 8.11 also shows that a Common filter is capable of providing reasonably uniform saturation energies across the detector; it is not necessary to optimise the LUT range usage on a tower-by-tower basis.

8.6 LUT E_T Calibration

There are two places in the Preprocessor system where the energy calibration is applied. Firstly, gains are applied to the analogue input pulse. During commissioning, these were calibrated to the e.m. E_T scale, such that 1 ADC count corresponds to 250 MeV. Secondly, the E_T scale is changed by the digital filter in a way that depends on the pulse shape. LUT E_T calibration must be corrected for this effect¹.

For early running, the LUT table E_T calibration was based on a simple linear slope set to convert the filter output back to the input E_T scale. These slopes were calculated from the pulse shape measurements, described in section 8.3. However, timing and pulse shapes in real collisions could differ from those measured from calibration pulses, leading to an incorrect energy

¹Ultimately, other effects, such as dead material effects, must also be accounted for. These more advanced corrections were not applied during the 2010 run.

measurement. The LUT E_T calibration was checked by measuring the relationship between the peak ADC sample of a pulse and the LUT output for collision pulses. The ADC input is ten bits wide and the LUT output is only eight bits wide. Hence, if the LUT is perfectly calibrated for collisions then the gradient should be $\frac{1}{4}$. Figure 8.12 shows the correlation between ADC peak sample and LUT output for a single trigger tower. The gradients were extracted from a linear fit to the data and are shown in Figure 8.13 for all towers in the e.m. barrel on the A-side of the detector. Most channels are within a few percent of the optimum value.

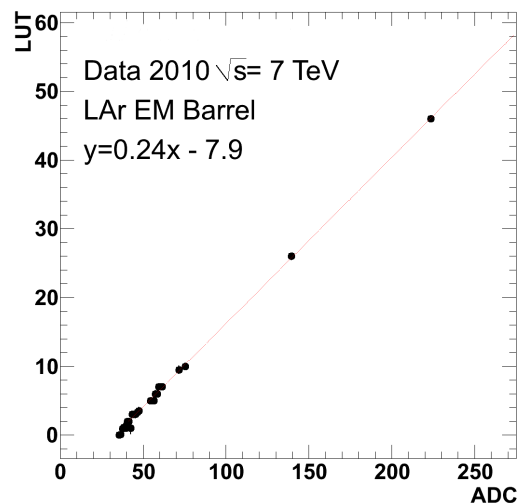


Figure 8.12: Correlation between ADC peak slice and LUT output for a single tower from collision pulses. The offset from the origin is due to the pedestal. A straight line is fit to the data points and the fit gradient is 0.24, close to the expected value of 0.25.

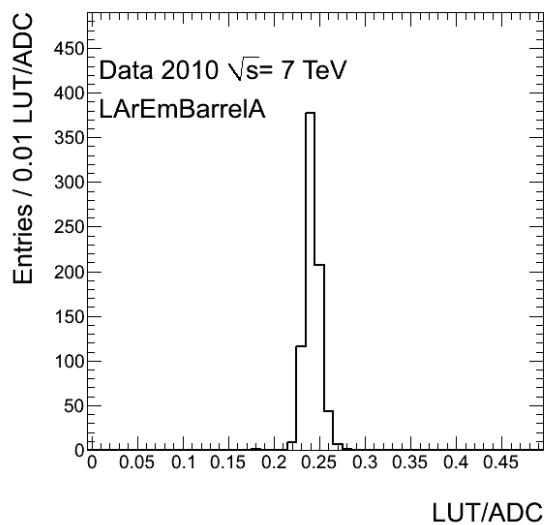


Figure 8.13: Fit gradients of ADC-LUT correlation for all channels in the LAr Barrel A-side.

8.7 Summary and Outlook

The L1Calo Preprocessor’s digital filter provides significant improvements in bunch-crossing identification of small signals, noise rejection and energy resolution. With the limited precision available in the filter coefficients, a common filter provides performance equivalent to that of filters tuned on a channel-by-channel basis, but with vastly reduced complexity in the system. Furthermore, the filter can be optimised to make best use of the look-up table range, at the expense of the precision match to the pulse shape, with no loss in performance.

Based on the studies presented in this chapter, a set of common filters applied across each calorimeter layer, with coefficients scaled to make the best use of the LUT range, were adopted for 2009-10 running. The coefficients used are shown in Table 8.1.

Cross-checks of the initial LUT E_T calibration show that it is already working well for pulses in early LHC beam collision data, though further calibration is required. The deviation from a perfect calibration is most likely due to differences in pulse shapes between calibration and physics pulses. A better understanding of the pulse shapes in physics events will be required for future calibrations.

Once sufficient integrated luminosity has been collected, the pulse shapes and performance can be measured by matching significant energy deposits in the calorimeters with offline reconstructed objects. To study e.m. pulses the obvious candidate process is $Z \rightarrow ee$. To study hadronic interactions good candidates are di-jet (jj) events, or direct photon (γj) events when a precise measurement of the jet E_T is required.

There are several areas where further study is required. The physics pulse shapes must be measured and the LUT E_T calibration corrected. In channels where the physics pulse shape is found to be significantly different to the calibration pulse shape, new filter coefficients may be required.

The studies presented in this chapter have focussed on small energy pulses and assumed that the pulse shape is independent of energy. This is known not to be the case. Specifically, in the Tile electronics, very high energy pulses are known to cause analogue saturation before the ADC saturation. This leads to a distorted pulse shape at high energies. The effects of this on the digital filter performance must be studied.

Finally, this study has neglected the effects of pile-up. As the LHC luminosity increases, so do the number of pile-up interactions in each event. At design luminosity, there will be on average 25 interactions per bunch-crossing.

An upgraded Super-LHC may have $\mathcal{O}(300)$ interactions per bunch-crossing. As well as this “in-time” pile-up, there is also an effect due “out-of-time” pile-up, as pulses from previous events can interfere with pulses from the present bunch-crossing. Pile-up effects on filter performance must be understood. If pile-up is found to significantly degrade performance, an alternative filter strategy, optimised for pile-up noise rather than Gaussian detector noise, may need to be developed.

Chapter 9

Summary

9.1 $H \rightarrow ZZ \rightarrow llbb$

In this thesis, the search prospects for a high mass Higgs boson in the channel $H \rightarrow ZZ \rightarrow llbb$ were studied. A simple cuts based analysis was used to select $H \rightarrow llbb$ events. Kinematic fitting was found to greatly improve the mass resolution of the experiment. Expected confidence limits were calculated using the CL_s method. It is possible to excluded a 400 GeV Higgs boson with a production cross-section around 8 times the Standard Model with 1 fb^{-1} of data. Note that this can be expected to improve significantly once the LHC reaches its design centre of mass energy of 14 TeV. The main power of this channel will come through combination with other channels to improve search sensitivity in the difficult, very high mass, region where all channels suffer from poor statistics.

As the LHC accumulates more integrated luminosity, further work will be needed to reduce the systematic uncertainties. To maximise the potential

of this channel, the use of more advanced analysis techniques and improved b -tagging may be used to improve the efficiency and signal to background ratio.

Initial investigations of the 2010 LHC run were presented. Control regions were defined to extract Z , $t\bar{t}$ and QCD enhanced samples from the untagged $lljj$ dataset. Similar techniques may be used on the b -tagged dataset when larger statistics are available. In general there is good agreement between data and Monte Carlo simulation, however, much more luminosity is required to make useful statements about the existence or exclusion of an $H \rightarrow llbb$ -like excess in this channel.

9.2 L1Calo Preprocessor Digital Filter

A study to determine the optimum coefficients for the L1Calo Preprocessor's digital filter was presented. The filter provides significant improvements in bunch-crossing identification of small signals, noise rejection and energy resolution. Contrary to the naive expectation, optimising the filter coefficients on a channel by channel basis did not yield significant improvements in performance. Instead, the filter coefficients were tuned to make best use of the look-up table range. Based on the studies presented in this thesis a set of common filters applied across each calorimeter layer were adopted for 2009-10 running. Further work is needed to study the physics pulse shapes and optimise the LUT E_T calibration.

Bibliography

- [1] R. Brun and F. Rademakers, *ROOT – An object oriented data analysis framework*, Nuclear Instruments and Methods in Physics Research Section A: Accelerators, Spectrometers, Detectors and Associated Equipment **389** (1997) no. 1-2, 81 – 86.
- [2] W. Verkerke and D. Kirkby, *The RooFit toolkit for data modeling*, ArXiv Physics e-prints (June, 2003) , [arXiv:physics/0306116](https://arxiv.org/abs/physics/0306116).
- [3] T. Junk, *Confidence level computation for combining searches with small statistics*, Nuclear Instruments and Methods in Physics Research Section A: Accelerators, Spectrometers, Detectors and Associated Equipment **434** (1999) no. 2-3, 435 – 443.
- [4] T. Junk, *MCLIMIT*, <http://www-cdf.fnal.gov/~trj/mclimit/production/mclimit.html>. (accessed 19/03/2010).
- [5] F. Englert and R. Brout, *Broken Symmetry and the Mass of Gauge Vector Mesons*, Phys. Rev. Lett. **13** (1964) 321–323.

- [6] P. Higgs, *Broken symmetries, massless particles and gauge fields*, Physics Letters **12** (1964) no. 2, 132 – 133.
- [7] G. S. Guralnik, C. R. Hagen, and T. W. B. Kibble, *Global Conservation Laws and Massless Particles*, Phys. Rev. Lett. **13** (1964) 585–587.
- [8] The LEP Higgs Working Group, *Search for the Standard Model Higgs boson at LEP*, Physics Letters B **565** (2003) 61 – 75, [arXiv:0306033 \[hep-ex\]](https://arxiv.org/abs/hep-ex/0306033).
- [9] B. W. Lee, C. Quigg, and H. B. Thacker, *Strength of Weak Interactions at Very High Energies and the Higgs Boson Mass*, Phys. Rev. Lett. **38** (1977) 883–885.
- [10] I. J. R. Aitchison and A. J. G. Hey, *Gauge Theories in Particle Physics: A Practical Introduction*. IOP Publishing, London UK, third ed., 2003.
- [11] W. J. Murray, ed., *Proceedings of the School for Experimental High Energy Physics Students*. 2008. RAL-TR-2009-010.
- [12] F. Halzen and A. D. Martin, *Quarks and Leptons*. 1984.
- [13] S. Dittmaier et al., *Handbook of LHC Higgs Cross Sections: 1. Inclusive Observables*, [arXiv:1101.0593 \[hep-ph\]](https://arxiv.org/abs/1101.0593).
- [14] The TEVNPH Working Group, *Combined CDF and D0 Upper Limits on Standard Model Higgs-Boson Production with up to 6.7 fb⁻¹ of*

- Data*, arXiv:1007.4587v1. Preliminary Results prepared for the ICHEP 2010 Conference.
- [15] T. Hambye and K. Riesselmann, *Matching conditions and Higgs mass upper bounds revisited*, Phys. Rev. **D55** (1997) 7255–7262, arXiv:hep-ph/9610272.
- [16] The LEP Higgs Working Group, *Precision Electroweak Measurements and Constraints on the Standard Model*, arXiv:0911.2604v2 [hep-ex]. Updated results and images for 2010 taken from <http://lepewwg.web.cern.ch/LEPEWWG/>.
- [17] The GFitter Group, *The electroweak fit and constraints on new physics*, arXiv:1006.0003 [hep-ph].
- [18] The GFitter Group, *The Global Electroweak Fit and Constraints on New Physics*, <http://gfitter.desy.de>. Talk presented at the International Conference for High Energy Physics 2010.
- [19] L. Evans and P. Bryant, *LHC Machine*, JINST **3** (2008) S08001.
- [20] C. Amsler et al, *The Review of Particle Physics*, Physics Letters **B667** (2008) .
- [21] The ATLAS Collaboration, *ATLAS Technical Design Report*, ATLAS TDR 15, CERN/LHCC 99-15 (1999) .
- [22] The ATLAS Collaboration Collaboration, *The ATLAS Experiment at the CERN Large Hadron Collider*, JINST **3** (2008) S08003.

- [23] R. K. Bock and A. Vasilesci, *The Particle Detector BriefBook*, <http://physics.web.cern.ch/Physics/ParticleDetector/BriefBook>, 1999. (accessed 05/08/2010).
- [24] The ATLAS Collaboration, *Expected Performance of the ATLAS Experiment Detector, Trigger and Physics*, arXiv:0901.0512v4 [hep-ex], CERN-OPEN-2008-020.
- [25] M. Cacciari, G. P. Salam, and G. Soyez, *The anti- k_t jet clustering algorithm*, JHEP **04** (2008) 063, arXiv:0802.1189 [hep-ph].
- [26] F. James and M. Walker, *MINUIT Users Guide*, 2004. <http://www.cern.ch/minuit>.
- [27] C. Gwilliam, D. Hadley, A. Mehta, J. Price, P. Thompson, J. Vossebeld, and C. Wiglesworth, *Discovery prospects for a very high mass Higgs boson in the channels $H \rightarrow ZZ \rightarrow ll\nu\nu$, $H \rightarrow ZZ \rightarrow llbb$ and $H \rightarrow ZZ \rightarrow lll$.*, Tech. Rep. ATL-PHYS-INT-2010-117, CERN, Geneva, Sep, 2010.
- [28] A. Read, *Presentation of search results: the CLs technique*, Journal of Physics G: Nucl. Part. Phys. 28 2693-2704 (2002). .
- [29] G. Piacquadio and C. Weiser, *A new inclusive secondary vertex algorithm for b-jet tagging in ATLAS*, Journal of Physics: Conference Series **119** (2008) no. 3, 032032.
- [30] T. Sjostrand, S. Mrenna, and P. Z. Skands, *PYTHIA 6.4 Physics and Manual*, JHEP **0605** (2006) 026, arXiv:hep-ph/0603175.

- [31] M. L. Mangano, M. Moretti, F. Piccinini, R. Pittau, and A. D. Polosa, *ALPGEN, a generator for hard multiparton processes in hadronic collisions*, JHEP **07** (2003) 001, arXiv:hep-ph/0206293.
- [32] R. Achenbach et al, *The ATLAS Level-1 Calorimeter Trigger*, JINST **3** (2008) P03001.
- [33] W. H. Ullrich Pfeiffer, *Bunch-Crossing Identification for saturated calorimeter signals*, ATL-DAQ-99-009.
- [34] ATLAS L1Calo Collaboration, *ATLAS Level-1 Calorimeter Trigger Algorithms*, ATL-DAQ-2004-011.
- [35] J. Garvey and D. Rees, *Bunch Crossing Identification for the ATLAS Level - 1 Calorimeter Trigger*, Tech. Rep. ATL-DAQ-96-051. ATL-D-PN-51, CERN, Geneva, May, 1996.
- [36] S. Frixione and B. R. Webber, *Matching NLO QCD computations and parton shower simulations*, JHEP **06** (2002) 029, arXiv:hep-ph/0204244.
- [37] GEANT4 Collaboration, S. Agostinelli et al., *GEANT4: A simulation toolkit*, Nucl. Instrum. Meth. **A506** (2003) 250–303.
- [38] S. Angelidakis, *Search for a Standard Model Higgs in the mass range 200-600 GeV in the channels $H \rightarrow ZZ \rightarrow ll\nu\nu$ and $H \rightarrow ZZ \rightarrow llqq$* , Tech. Rep. ATL-COM-PHYS-2011-041, CERN, Geneva, Jan, 2011.

Glossary

ATLAS	A Toroidal LHC ApparatuS . A good example of a particle physics backronym.
BCID	Bunch-crossing Identification.
BSM	beyond-the-standard-model.
Cluster Processor	The L1Calo Processor system that runs the e/γ and τ /had algorithms..
CMM	Common Merger Module. Calculates object multiplicities found by the Processor Systems and sends the results to the CTP.
CPM	Cluster Processor Module.
CSC	Cathode Strip Chamber. Part of the Muon spectrometer.
CTP	Central Trigger Processor.
EM Barrel	Barrel section of the e. m. calorimeter.

EMEC	Electro-magnetic End-cap. The end-cap section of the e. m. calorimeter.
FCal	Forward Calorimeter.
FIR	Finite Impulse Response.
GPD	General Purpose Detector.
HEC	Hadronic End-cap. End-cap section of hadronic calorimeter.
HLT	High Level Trigger.
ID	Inner Detector.
JEM	Jet Energy Module.
Jet Processor	The L1Calo Processor system that runs the jet finding, E_T^{miss} and total- E_T algorithms.
L1A	Level-1 Accept. The signal sent by the CTP to trigger readout from the detector.
L1Calo	Short-hand to describe the Level-1 Calorimeter Trigger collaboration or the system itself.
LAr	Liquid Argon.
LEP	Large Electron Positron collider.

LHC	Large Hadron Collider.
LUT	Look-up Table.
MDT	Monitored Drift Tube. Part of the Muon spectrometer.
pixels	Pixel Sensors. Part of the ID.
Preprocessor	The L1Calo Preprocessor system.
Presampler	Presampler. Part of the calorimetry placed in front of the solenoidal magnet.
ROD	Readout Driver.
RoI	Region of Interest. Level 1 information used to seed Level 2 trigger algorithms.
RPC	Resistive Plate Chamber. Part of the Muon spectrometer.
SCT	Silicon-microstrip Tracker. Part of the ID.
TGC	Thin Gap Chamber. Part of the Muon spectrometer.
Tile EB	Tile Extended Barrel. The end sections of the Tile calorimeter.

Tile LB	Tile Long Barrel. The central section of the Tile calorimeter.
TRT	Transition Radiation Tracker. Part of the ID.

Appendix A

Cross-sections

A complete list of the signal and background cross-sections used in the physics analysis presented in chapters 5 and 6 to normalise Monte Carlo samples follow. The samples used were centrally produced by ATLAS. The Monte Carlo event generators used were: Pythia [30], ALPGEN [31] and MC@NLO [36]. The detector simulation was implemented with GEANT4 [37].

Table A.1 shows the $\sigma \times BR$ and event generators used for the signal samples. The cross-sections were taken from reference [27].

Table A.2 shows the cross-sections and event generators used for background samples. The cross-sections were taken from reference [38]. The Z +jet samples were generated using ALPGEN. The numbers include a k -factor of 1.22 to make the inclusive Z cross-section agree with NLO calculations. A filter is applied to the $t\bar{t}$ sample at the generator level. The filter requires at least one of the W bosons to decay leptonically.

Table A.1: A complete list of all Higgs signal Monte Carlo samples and cross-sections.

Process	σ [fb]	Generator
$H(200) \rightarrow ZZ \rightarrow llqq$	211	Pythia
$H(220) \rightarrow ZZ \rightarrow llqq$	192	Pythia
$H(240) \rightarrow ZZ \rightarrow llqq$	166	Pythia
$H(260) \rightarrow ZZ \rightarrow llqq$	146	Pythia
$H(280) \rightarrow ZZ \rightarrow llqq$	129	Pythia
$H(300) \rightarrow ZZ \rightarrow llqq$	117	Pythia
$H(320) \rightarrow ZZ \rightarrow llqq$	109	Pythia
$H(340) \rightarrow ZZ \rightarrow llqq$	106	Pythia
$H(360) \rightarrow ZZ \rightarrow llqq$	107	Pythia
$H(380) \rightarrow ZZ \rightarrow llqq$	95.8	Pythia
$H(400) \rightarrow ZZ \rightarrow llqq$	82.6	Pythia
$H(420) \rightarrow ZZ \rightarrow llqq$	70.1	Pythia
$H(440) \rightarrow ZZ \rightarrow llqq$	59.1	Pythia
$H(460) \rightarrow ZZ \rightarrow llqq$	49.7	Pythia
$H(480) \rightarrow ZZ \rightarrow llqq$	41.8	Pythia
$H(500) \rightarrow ZZ \rightarrow llqq$	35.1	Pythia
$H(520) \rightarrow ZZ \rightarrow llqq$	29.5	Pythia
$H(540) \rightarrow ZZ \rightarrow llqq$	24.9	Pythia
$H(560) \rightarrow ZZ \rightarrow llqq$	20.9	Pythia
$H(580) \rightarrow ZZ \rightarrow llqq$	17.7	Pythia
$H(600) \rightarrow ZZ \rightarrow llqq$	15.0	Pythia

Table A.2: A complete list of all background Monte Carlo samples and cross-sections.

Process	σ [fb]	Generator
$Z + 0p, Z \rightarrow ll$	805000	ALPGEN
$Z + 1p, Z \rightarrow ll$	162000	ALPGEN
$Z + 2p, Z \rightarrow ll$	48700	ALPGEN
$Z + 3p, Z \rightarrow ll$	13600	ALPGEN
$Z + 4p, Z \rightarrow ll$	3340	ALPGEN
$Z + 5p, Z \rightarrow ll$	976	ALPGEN
$Zb\bar{b} + 0p, Z \rightarrow ll$	7954	ALPGEN
$Zb\bar{b} + 1p, Z \rightarrow ll$	3013	ALPGEN
$Zb\bar{b} + 2p, Z \rightarrow ll$	986	ALPGEN
$Zb\bar{b} + 3p, Z \rightarrow ll$	472	ALPGEN
$ZZ \rightarrow llqq$	561	Pythia
$W^+Z \rightarrow l^+l^-q\bar{q}$	522	MC@NLO
$W^-Z \rightarrow l^+l^-q\bar{q}$	295	MC@NLO
$t\bar{t}$ (excluding fully hadronic)	91550 (including $\epsilon_{\text{filter}} = 0.56$)	MC@NLO